Distortion correction for free-space quantum communication

by

Chemist M. MABENA

Submitted in fulfillment of the requirements
for the degree of Doctor of Philosophy
in the

Structured Light group, School of Physics, Faculty of Science

September 2019

Distortion correction for free-space quantum communication

by

Chemist M. MABENA

Supervisor: **Dr. Filippus S. ROUX**

Co-supervisor: **Dr. Kahesh DHUNESS**

Co-supervisor: **Prof. Andrew FORBES**

UNIVERSITY OF THE WITWATERSRAND

Faculty of Science

School of Physics

Structured Light group

Doctor of Philosophy

Abstract

The work in this thesis can be put into two categories: First, the effect of atmospheric turbulence on single-photon optical fields and on quantum entangled orbital angular momentum (OAM) systems is assessed. Secondly, the mitigation against the effects of atmospheric turbulence on OAM based quantum systems is considered.

In the first part, the evolution of single-photon optical fields propagating through atmospheric turbulence is studied under arbitrary turbulence conditions. The single phase screen (SPS) model and the infinitesimal propagation equation (IPE) are used to compute the optical power fractions in an input Laguerre-Gaussian (LG) mode. The power fractions transferred to high-order LG modes are also computed. The study shows that while under weak scintillation conditions the IPE and the SPS models show the same trend, they deviate when the strength of scintillation reaches a certain threshold. The above computations are subsequently compared with numerical simulations of optical fields propagating through atmospheric turbulence. The numerical simulations are performed in accordance with the multi-phase screen (MPS) model based

on the Kolmogorov theory of turbulence. The simulations are performed for different turbulence strengths to allow for comparison in both weak and strong scintillation. The numerical results are in agreement with the IPE results for all conditions, but they deviate from the SPS results for weak scintillation.

Further, as part of the first category, the effect of the atmospheric turbulence on second-order quantum interference in the Hong-Ou-Mandel (HOM) effect is investigated. The investigation involves a theoretical and experimental analysis. In the experiment, quantum states that are entangled in the orbital angular momentum (OAM) degree of freedom are prepared with spontaneous parametric downconversion (SPDC). The atmospheric turbulence, which is modeled in accordance with the SPS approach, is simulated with spatial light modulators according to the Kolmogorov theory of turbulence. Both the theoretical and experimental analyses show that the HOM dip is unaffected when only one of the photons passes through atmospheric turbulence. However, it is observed that when both photons are sent through the atmospheric turbulence, the HOM is only slightly affected.

The second part of the thesis starts with the proposal of a method for characterizing a high-dimensional quantum channel with the aid of classical light. The method uses a single non-separable input optical field that contains correlations between the spatial modes (OAM) and the wavelength degrees of freedom. The channel estimation process incorporates the spontaneous parametric upconversion or sum frequency generation to perform the pertinent measurements.

Finally, singular value thresholding (SVT) based compressive sensing is used to perform high dimensional quantum channel estimation. The estimated channel is subsequently used to correct for the turbulence induced distortion on the input quantum state. As a measure of the success of the procedure, the fidelity and trace distance of the corrected density matrix against the ideal maximally entangled qutrit state is computed. The results are compared with those of the uncorrected density matrix. Furthermore, the amount of entanglement is quantified using both the corrected and the uncorrected density matrices.

Declaration of Authorship

I, Chemist M. MABENA, declare that this thesis titled, "Distortion correction for free-space quantum communication" and the work presented in it are my own. I confirm that:

- This thesis has not been submitted for any degree or examination at any other university.
- Where I have consulted the published work of others, this is always clearly attributed.
- This thesis does not contain other people's data, pictures, graphs or other information unless specifically acknowledged as being sourced from other researchers. Where other written sources have been quoted, then:
  - Their words have been rewritten but the general information attributed to them has been referenced.
  - Where the exact words have been used, then their writing has been place in italics and/or inverted quotation marks, and referenced.
- This thesis does not contain text, graphics or tables copied from the internet, unless specifically acknowledged, and the source being detailed in the thesis and the Bibliography.

Signed: Mabena

Date:13/09/2019

"All the 50 *years of conscious pondering did not bring me nearer to the answer to the question "What is light quanta?" Nowadays every rascals believes he knows the answer, however, he is mistaken. "*

Albert Einstein

Acknowledgements

I wish to thank Stef for being an excellent supervisor, my family and friends for the unwavering support, and all the colleagues that have contributed in all sorts of ways. Last but not least, the financial assistance of the Council for Scientific and Industrial Research (CSIR) towards this research is hereby acknowledged.

Contents

List of Figures

List of Abbreviations

HOM	**H**ong **O**u **M**andel
IPE	**I**nfinitesimal **P**ropagation **E**quation
OAM	**O**rbital **A**ngular **M**omentum
SAM	**S**pin **A**ngular **M**omentum
SPDC	**S**pontaneouos **P**arametric **D**ownconversion
SPS	**S**ingle **P**hase **S**creen
SVT	**S**ingular **V**alue **T**hresholding

I dedicate this thesis to my late grandmother, Linah Pimpi Thabethe.

Chapter 1

Mapping matters into perspective

1.1 Background and Motivation

Communication is a very broad subject, however, it suffices to say that it constitutes an exchange of information. The exchange occurs in a variety of ways: this could be through writing, speaking or some other method. The human species has developed to the point that communication can be extended to the level of machines. In machine language, information processing pertains to manipulating 0s and 1s: the so-called bits. This type of processing has enabled a vast array of services including but not limited to telephones, Whatsapp, Facebook, online credit card transactions, and so forth.

It would not be untrue to say that communication engulfs a very large portion of our existence. While this is a "pro", it is also important to take into consideration the "cons" associated with such a powerful tool. Like fire, communication is a useful tool however its disadvantages can be detrimental. There are instances when communication should be private and only be kept between the involved parties. Situations like this require the use of cryptographic methods [1] to ensure the security of the communication. The most popular and widely used method is the RSA public key encryption method. It is named in this way after its creators Rivest, Shamir, Adleman [2]. While the RSA is believed to be extremely safe, there exist at least two methods that could be used to break its security. These are order finding and factoring [3]. As things currently stand, large number factorization is considered a very difficult problem to solve with a classical computer. Therefore, by virtue of this, the RSA method is considered to be really secure.

The safety of the RSA method cracks in the midst of quantum information processing. Quantum information deals with the concepts and applications of information theory within the context of quantum mechanics. Quantum information processing promises the development of quantum computers. The most popular selling point of a quantum computer is that it can perform tasks more efficiently than a classical computer. One of key tasks that were identified is the factorization of very large numbers [4]. The cornerstone of the RSA method.

Quantum optics is the part of quantum theory that deals with the interaction of light with matter. In particular, it refers to the phenomena that can only be understood through the quantization of both the light and matter. This branch of optics came into existence in the second half of the 20$^{\text{th}}$ century with the key contributions coming from the invention of the maser and laser [5, 6, 7]. While the quantum theory of light (quantization of light) was introduced a few decades earlier by Dirac [8] and Fermi [9], it can be argued that the theoretical formulation of modern quantum optics was established by Roy Glauber around the same time as the invention of the laser. Glauber, stimulated by experimental progress at the time was able to formulate the quantum theory of optical coherence [10]. In the book titled: *Introduction to QUANTUM OPTICS: from the Semi-classical Approach to Quantized light*, the authors wrote, "Actually, Glauber developed a clear quantum formalism to describe optics phenomena, and introduced the important notion of quasi-classical states of light, a theoretical tool that allowed physicists to understand why all available sources of light, including lasers, delivered light whose properties could be totally understood in the framework of the semi-classical approach." [11].

During its development, a lot of interest in quantum optics was associated with its implications on the fundamentals and foundations of quantum mechanics. A merger of both quantum optics and quantum information seems like a step in the progressive direction as this opens up a new avenue for quantum optics, one that addresses a technological breakthrough. The most popular applications that benefit from the merger of these two fields are quantum computation, quantum sensing, and quantum communication. The latter is the driver behind the work of this thesis. While there are various aspects to quantum communication, to highlight the relevance of the work in this thesis we will zoom into one particular form that is related to the security of communication systems.

It was mentioned above that the security of the RSA method is threatened by quantum computing. The solution to this problem is also quantum mechanics. This brings a fresh meaning to the adage: fight fire with fire! Quantum key distribution (QKD), as it is currently called, is a cryptographic scheme that is based on the fundamental principles of nature. It is a completely different way of performing encryption. This is in contrast to the standard methods of "classical" cryptography whose security is based on the complexity of solving some mathematical problem. Since its inception, there are a number of protocols that have been developed [12, 13, 14, 15, 16, 17]. However, the most popular QKD protocols include the BB84 protocol [18] and the E91 protocol [19]. The BB84 is based on the notion that it is not possible to copy quantum information without disturbing the quantum system, and the E91 is based on quantum entanglement.

Quantum communication, in general, benefits from increasing the dimension of the Hilbert space of the quantum systems. One popular contender as a degree of freedom for high-dimensional quantum systems is the orbital angular momentum (OAM) of light. In the case that free-space is used as a communication channel, the OAM states of light, however, seize to be ideal. This is because they are susceptible to atmospheric turbulence. In this thesis we consider the OAM states of light propagated through atmospheric turbulence and further look at how to mitigate the adverse effect of the atmospheric turbulence in such a way that we can preserve the quantum entanglement in the propagated quantum systems.

1.1.1 Quantum entanglement

Quantum mechanics is a theoretical framework which is used to predict and understand the behavior of nature at the most fundamental level [20]. It continues to provide a level of accuracy in predictions that supersedes any classical framework. Nonetheless, during its development, there were some uncomfortable implications that the theory posed [21]. For instance, quantum mechanics predicts that at the most fundamental level nature is not a deterministic process, rather it is intrinsically probabilistic. This was really uncomfortable for many people at the time. So much so that a group of scientists: Einstein, Podolsky, and Rosen (EPR) wrote a paper that was meant to show that quantum mechanics is an incomplete theory [22]. In the paper, the trio proposed a thought experiment that involves the so-called EPR state. The EPR state is a pure state consisting of two subsystems, A and B, that have been emitted by some source (or that would have interacted somehow in the past). The two subsystems are described such that they remain correlated even after they have been spatially separated by an arbitrary distance. Such a pure state is said to be non-separable since it cannot be written as a product of the states of the two subsystems A and B. In this form, the EPR state implies that one can be able to predict with absolute certainty the outcome of a measurement on one subsystem based on the results obtained by measurement on the other subsystem.

In the original paper the authors consider the logical connection between two assertions: 1) the description of reality as given by quantum mechanics is incomplete, or 2) any two non-commuting observables cannot have simultaneous reality. By using the EPR state, they argue the disjunction in the two assertions.Particularly, they use the EPR state to show that it possible for two non-commuting to have simultaneous real values which could be predicted with absolute certainty. Their conclusion, therefore, was that quantum mechanics is incomplete as it is incapable of giving all possible information about a quantum system.

In light of this conclusion, a few scientists at the time including David Bohm started contemplating alternative theories to quantum mechanics, particularly, a hidden variable theory that was meant to provide the information which the quantum theory was always missing. This could, therefore, account for the non-deterministic results obtained via quantum mechanics. As a response to the EPR paper, Schrödinger wrote a paper [23] in the same year 1935 in which he coined the word entanglement.

Approximately three decades later, in 1964, John Bell put the ideas in the EPR paper into perspective. He formalized the EPR local hidden variable model ideas in accordance with three assumptions that are collectively known as *local realism and free will*. The first assumption that the EPR hidden variable model considers is called realism. It states that physical properties have definite values that exist independent of any observation. The second assumption is locality. It states that a local measurement result is independent of any other event that is performed with a space-like separation from the local measurement. The last is free-will. It states that the settings of the measurement equipment of a local result do not depend in any way on the properties of the system that determines the local result. Bell, working from this formal structure of the EPR model was able to derive an inequality for the statistical correlations of the results of measurements of a two-qubit system. He was able to show that any such local hidden variable model gives results which are significantly different from those of quantum mechanics in certain situations. In his analysis, Bell essentially set up an inequality that gives an upper bound for the strength of the correlations that would exist for a theory obeying local realism. He showed that there are certain correlated quantum states that are able to surpass this upper bound, and thus violate the Bell inequality. Clauser, Horne, Shimony and Holt [24] derived an inequality that could be tested in an experiment as an extension of the work done by Bell. There exist other inequalities which have been derived, and they are all collectively called the Bell inequalities. Despite the theoretical progress, the "Bell" inequality was only confirmed experimentally in 1972 by Freedman *et al.* [25].

Outside of its domain as an interesting and fundamental phenomenon, quantum entanglement can also be used for technological advances that are based on quantum information processes. It is a crucial resource for the implementation of quantum computing [26, 3], quantum teleportation [27, 28], superdense coding [29, 30], and quantum cryptography as already alluded to above [19].

Furthermore, it has been suggested and shown that high-dimensional quantum systems are better than the ordinary two-dimensional quantum systems. This has been shown in the context of communication regarding information capacity and security in quantum cryptography [31, 32]. High dimensional quantum systems, or quNits as they are usually referred to, lead to high-dimensional quantum entanglement. Such systems, which possess high-dimensional entanglement, can be generated by using the orbital angular momentum (OAM) of light.

1.1.2 Orbital angular momentum of light

Angular momentum as a property of optical fields has a history dating back to the early 1900s. Using a mechanical analogy Poynting [33] was able to show theoretically that light should possess angular momentum that is associated with circular polarization. For a single photon, this angular momentum is $\pm\hbar$ depending on whether it is right or left circularly polarized. This is the so-called spin-angular momentum (SAM) [34]. In his analysis, Poynting also proposed a method or experiment of how his predictions could be tested. However, the confirmation of his work was not carried out as he had intended. A variation of the proposed experiment was performed by Beth approximately three decades later [35].

The idea of OAM of light was not really popular. Nevertheless, it was known for a very long time that light had to have a contribution to the angular momentum that was not the SAM [36]. This is because it had been observed that higher-order transitions, e.g. quadrupole, required the emitted light to carry angular momentum that was above the maximum magnitude possible by SAM [37, 38]. That is, these transitions required light that carried angular momentum that was multiples of $\hbar$. In 1992 Allen *et al.* [39] showed that optical fields with an azimuthal phase dependence given as $\exp(i\ell\phi)$ carry angular momentum that is proportional to $|\ell|$, and most importantly it does not depend on the polarization state of the optical field. The key point about this realization was that the OAM is a natural property of such optical fields, and therefore they can be readily generated in the laboratory. At this point, it is important to note that even prior to this realization, helically phased optical fields had already been subject to intensive study. Albeit, the focus was not on their ability to carry OAM.

The optical field that was considered in the study by Allen *et al.* is the Laguerre-Gaussian mode (LG) [40, 41, 42]. The LG modes form a complete and orthogonal basis set. In the latter study, the LG modes were generated by using Hermite-Gaussian modes and transforming them by cylindrical mode converters [39, 43, 44]. There exist other methods of generating LG modes: these include the use of spiral phase-plates [45, 46, 47, 48], q-plates [49, 50] and holograms [51, 52, 53]. The hologram method is the most widely used and preferred method because of its simplicity and ease of application. Other optical fields that carry OAM include high-order Bessel beams [54, 55], Ince-Gaussian beams [56] and Mathieu beams [57].

The OAM of optical fields is associated with the spatial distribution of the optical fields, through the azimuthal index ℓ. In principle, there is no fundamental limitation on the values of ℓ that can be associated with any single photon. Therefore, the OAM degree of freedom spans an infinite dimensional Hilbert space. This further implies that by using the OAM of light it is possible to produce quantum states of arbitrary dimension. In practice, there are various methods for producing single photons but not a lot that produce entangled photons.

1.1.3 Spontaneous parametric down conversion

Spontaneous parametric down conversion (SPDC) is perhaps the most powerful and widely used source of single and entangled photons [58]. Parametric down-conversion is a non-linear process where a photon from a high intensity laser produces two photons under the conservation of energy and momentum [59]. The state of the two photons that are produced in this way is nonseparable; which means that the two photons are entangled [60]. The photon pair can be entangled in a number of different ways: this can be through temporal frequencies [61], energy and time variables [62], etc. As already alluded to above, the high dimensionality of the OAM of light promises to be an important resource for realizing high-dimensional entanglement. In the early 2000s an experiment was presented by Mair *et al.* [63] in which the spatial modes of optical fields that carry OAM were used to create high-dimensional entanglement. Particularly, in the down conversion experiment of Mair *et al.* the correlation between the LG modes of the signal and the idler were observed; the authors further confirmed that the correlations they had observed cannot be explained in terms of classical correlations.

Around the same period, theoretical works were proposed to account for the experimental observations [64, 65]. In the work by Arnaut and Babosa [64], the authors found the general form of the eigenstate vector describing single photons carrying intrinsic angular momentum and OAM. In the work by Franke-Arnold *et al.* [65], the authors investigated the OAM correlation of the entangled photon pair in the SPDC process. They show how the OAM is a consequence of the phase matching in the nonlinear crystal.

The use of SPDC to generate OAM entangled photons has opened up an arena for a number of studies in quantum communication [66, 67, 68, 69, 70]. These studies are directed towards showing the advantage of OAM as a degree of freedom in free-space optical and quantum communication.

Free-space quantum and optical communication use the atmosphere as a channel for transmission. Unlike the polarization degree of freedom, OAM is susceptible to the atmospheric turbulence [71, 72, 73, 74, 75, 76, 77, 78, 79, 80, 81, 82]. This implies that successful implementation of the OAM degree of freedom in communication systems can only be achieved after a thorough understanding of how the atmospheric turbulence affects the OAM modes of light has been established.

1.1.4 Atmospheric turbulence effects on OAM states

The first treatment of the effect of atmospheric turbulence on a communication system that is based on the OAM of light was given by Paterson in 2005 [71]. In this work, Paterson quantified the effects of atmospheric turbulence on the coherence of single-photon communication systems that are based on OAM states. By considering LG modes, he employed a semi-classical model to derive a rotational coherence function, which he then used to obtain the scattering equations for different OAM modes. The expressions for the scattering probabilities are integrals and are, in general, intractable. In an effort to alleviate the intractability, Paterson considered a special case. He restricted his analysis to the weak scintillation regime. Within this regime, the effect of the atmospheric turbulence is considered as a mere phase perturbation. That is, it is assumed that the overall effect of the atmospheric turbulence is a modulation of the optical field with a random phase function. This consideration will, for the rest of this thesis, be referred to as the single phase screen model (SPS). The results obtained by Paterson using the SPS were sufficient to show that even weak scintillation can cause significant problems for OAM based communication systems.

Tyler and Boyd [74], using the SPS model, considered the effect of atmospheric turbulence on optical vortex beams, where optical vortices can be described as optical fields with an azimuthal phase dependence with a Gaussian envelop. More generally, optical vortices are singularities in the phase of an optical field, this leads to optical fields that have helical wavefronts. In their work, they analytically determined the probability of a detected photon to retain its original (initial) OAM after going through the atmospheric turbulence. Apart from some nuances, the results of this work show that the behavior of optical vortex beams in atmospheric turbulence is comparable to that of LG modes.

Experimental studies on the effects of atmospheric turbulence, particularly based on the SPS model, on OAM carrying optical fields include the work done by Rodenberg *et al.* [83] and the work by Malik *et al.* [77]. In the former study, the authors experimentally assessed the degradation of mode purity for optical fields that carry OAM. They used a phase-only spatial light modulator to introduce the atmospheric turbulence for 11 different OAM modes. They showed that atmospheric turbulence degrades all the modes irrespective of the OAM mode number. In the latter work, Malik *et al.* experimentally implemented a free-space 11-dimensional communication system based on OAM modes. They quantified the channel capacity of their communication system and found that it had a maximum OAM channel capacity of 2.12 bits/photon. They also showed that the atmospheric turbulence degrades the performance of the communication system.

So far, we have reviewed the work done within the SPS model and we have further limited our attention to single-photon and classical systems. However, there also exists studies on how the atmospheric turbulence affects quantum states that are entangled in the OAM degree of freedom.

Considering weak scintillation conditions, Smith and Raymer performed a theoretical study of the effect of atmospheric turbulence on the OAM entanglement of a two-qubit system [84]. They found that higher order OAM modes are more robust. While these high modes are more robust, they tend to have a high rate of crosstalk to other modes than the lower order modes. In their analytical calculations, Smith and Raymer simplified the intractable integrals that involve the structure function by approximating it with a quadratic function [85]. The work of Smith and Raymer has been corroborated by Hamadou *et al.* [78]. Hamadou *et al.* studied atmospheric turbulence induced decay of OAM entanglement in a two-photon system, both numerically and experimentally. The experiments were performed by using a spatial light modulator to simulate the weak scintillation. They considered two separate cases: in one case, only one photon goes through the atmospheric turbulence and in the other both photons go through the atmospheric turbulence. In both cases, their results correspond to those of Smith and Raymer. The quantum entanglement is more robust in higher OAM modes. The authors further derived an empirical formula for the distance scale at which the entanglement decays.

Gopal and Andrews numerically analyzed the effect of Kolmogorov turbulence on states that are produced using the SPDC process [76]. By calculating joint and signal photon detection probabilities as a function of the mode width to the Fried parameter, they found that entangled photons that are produced using SPDC are less robust than generic single photons in Kolmogorov turbulence. However, the authors also found that a single photon produced through the SPDC, say the signal photon, is more robust than a generic single photon in the lowest order modes.

In another study, Leonhard *et al.* [81] also studied the case of an OAM entangled qubit system through atmospheric turbulence. They found that by introducing a phase correlation length they could show that entanglement of OAM photons displays a universal exponential deterioration.

Around the same time as the authors of the latter work, Goyal *et al.* [80] studied the effect of atmospheric turbulence on the secret key rate for quantum key distribution in OAM based quantum communication. The authors found that the secret key rate goes to zero at approximately the same scale where the entanglement of formation goes to zero.

Yingwen *et al.* [79] investigated the effects of atmospheric turbulence, both theoretically and experimentally, on high-dimensional entangled photonic states generated through the SPDC process. The authors considered the case where only one of the photons goes through the atmospheric turbulence. A full state tomography of the output states was performed, and the obtained density matrices were used to quantify the amount of entanglement as a function of scintillation strength. Their results show that the entanglement decays as a function of scintillation strength, although the theory predicts that it never goes to zero in the case of one-sided atmospheric turbulence.

The results obtained thus far have limited validity. They are only valid within the weak scintillation regime. In 2014, Hamadou *et al.* showed using numerical simulations that the SPS model cannot be used to accurately describe the evolution of OAM entanglement beyond the weak scintillation regime [86]. The study showed that within the SPS model the evolution of quantum entanglement is well described by a single dimensionless parameter, whereas for strong scintillation two dimensionless parameters are necessary for the accurate description of the OAM entanglement evolution. The authors also found that in strong scintillation the higher order OAM modes are no longer robust in atmospheric turbulence.

The authors of the latter study used the multi-phase screen (MPS) model, which is based on the split-step method [87, 88]; it is valid in both weak and strong scintillation regimes. The MPS model is an extension of the SPS model; instead of representing the atmospheric turbulence as a single-phase screen, it is rather represented by a series of phase screens. Each of these phase screens has to obey the SPS model conditions.

Anguita *et al.* also used the MPS model to numerically analyze the effect of atmospheric turbulence on a multi-channel free-space optical communication system based on OAM carrying optical fields [89]. They found that atmospheric turbulence induces attenuation and cross-talk among the different OAM modes. Furthermore, the authors also found that atmospheric turbulence causes the aggregate channel capacity to decrease. By considering a binary symmetric channel, with crosstalk that is modeled as a Gaussian noise source, they were able to find an optimal set of OAM states for each turbulence condition and quantify the channel capacity for the obtained set of states.

There also have been some effort in studying the effects of the atmospheric turbulence on OAM modes outside of the SPS region of validity in experiments. Pors *et al.* performed an experimental investigation of the effect of atmospheric turbulence on the coincidences of two photons that are entangled in the OAM degree of freedom and are produced through the SPDC process [72]. The atmospheric turbulence was experimentally simulated using a turbulent cell in which cold and warm air were mixed to generate the random temperature variations which cause the fluctuations in the index of refraction. In their investigation, they found that the number of entangled modes decreases with increasing scintillation. Their results further showed that the shape of the coincidence curve is robust under the atmospheric turbulence.

On the analytical side, a model for the evolution of entangled quantum states in atmospheric turbulence that is supposed to be valid under all scintillation conditions has been derived [90, 91, 82]. The derivation is based on the MPS model of the atmospheric turbulence. The distortion of the atmospheric turbulence is treated as an infinitesimal transformation. In its original form [90, 91], the infinitesimal propagation equation (IPE) was formulated in the Laguerre-Gaussian (LG) basis, which is a discrete basis. This led to an infinite set of coupled differential equations, therefore to obtain a solution it was necessary to truncate the IPE. The truncation had the unfavorable effect of not correctly representing the crosstalk among the different OAM modes. This resulted in predictions by the IPE that deviated from the numerical simulations and experiments [78]. The truncation problem was resolved by formulating the IPE using a continuous basis, the plane wave basis [82]. In this new formulation, an analytical solution to the IPE is obtained by using the quadratic structure function approximation to the Kolmogorov model of turbulence. Upon converting into the discrete OAM basis, the new solution correctly represents the effects of coupling among the different OAM modes for arbitrary turbulence conditions.

All the studies that have been discussed paint a good picture of where we are with regards to realizing functional free-space optical and quantum communication systems that are based on the OAM of light. It is clear that to take advantage of the dimensionality afforded by the OAM of light we would have to develop systems and protocols that mitigate against the adverse effects of the atmospheric turbulence. This is part of the contribution of this thesis.

1.1.5 Mitigation against atmospheric turbulence effects

In the same work where Paterson characterized the effect of atmospheric turbulence on single-photon communication systems, he also suggested that adaptive optics could be used to mitigate the adverse effects caused by the atmospheric turbulence. This approach has played a significant role in classical studies of OAM based free-space optical communication [92, 93, 94, 95, 96, 97, 98, 99]. As a brief review, next, we mention just a few.

Zhao *et al.* [92] performed a study to compare the Shack-Hartmann wavefront sensing method based on Zernike polynomials and another phase correction method which is based on the OAM modes. In their numerical results, they found that the OAM based phase correction method outperforms the Zernike polynomials based wavefront sensing method; their numerical results showed that both methods improve the mode purity of single OAM states and the channel capacities of the free-space optical communication link. The authors further performed an experiment which showed that the OAM based correction method mitigates the adverse effects of the atmospheric turbulence.

Ren *et al.* proposed an adaptive compensation scheme to simultaneously correct multiple OAM optical fields propagating through atmospheric turbulence [93]. In this work, a Gaussian beam in one of the polarization states was used as a beacon to probe the atmospheric turbulence. The beacon was used to obtain the phase correction pattern for the compensation of OAM modes which were in the orthogonal polarization. In an effort to preserve both polarization states in the multiplexing scheme for information transfer, Ren *et al.* [97] did a follow-up study using a Gaussian beam on a different wavelength as a beacon. They also derived the phase correction pattern for the compensation of the OAM modes passing through the same turbulence. Both these approaches led to noticeable mitigation of the adverse atmospheric turbulence effects on the OAM modes.

The traditional method of wavefront sensing using a Shack-Hartmann wavefront sensor relies on local slopes between parts of the beam, however, when the incident beam carries OAM there exists a singularity at the center. In the specific case of strongly scintillated beams this may lead to challenges in using the traditional method for wavefront sensing [100] and such an approach may thus be unsuccessful. To overcome this hurdle, Xie *et al.* [98] used a method that uses the intensity of the incoming optical field together with a stochastic-parallel-gradient-descent algorithm based on Zernike polynomials to generate a phase pattern for the correction of distorted OAM modes. This work was done experimentally and they found that a phase pattern obtained from an arbitrary OAM mode could be used to correct the distortion of other OAM modes that have gone through the same atmospheric turbulence.

While the above discussion has focused mainly on classical studies, there also exists studies on the mitigation of the effects of atmospheric turbulence on OAM photons in the quantum communication domain. Alonso and Brunn [101] numerically simulated the propagation of OAM photons through the atmosphere and studied the resulting errors. Using the numerical simulation, they extracted the Kraus operator representation for the OAM photons error process due to the atmospheric turbulence. Furthermore, the authors applied approximate quantum error correction in an effort to protect the OAM photon from the atmospheric perturbation. As a concluding remark, the authors indicated that the range over which their quantum error correction is useful is limited and thus suggest a pairing with adaptive optics or decoherence-free subspaces.

More recently, adaptive optics was applied in quantum optics. Leonhard *et al.* [102], through a multi-phase screen simulation, showed that an adaptive optics system could be used to correct for the effects of the atmospheric turbulence on an entangled quantum system. The focus of this work was on the efficiency of an adaptive optics system in preventing the loss of quantum entanglement, and the trace of the qubit density matrix. The authors were able to show that even by a simple correction of the tilt introduced by the atmospheric turbulence there is a significant improvement in the retained entanglement and the trace of the qubit density matrix.

Ndagano *et al.* [103] established that the evolution of vector vortex modes, which are considered to represent the so-called classically entangled system, in atmospheric turbulence is the same as the evolution of OAM entanglement that exists between a pair of photons that are produced through the SPDC process. They also claim that the equivalence is, in fact, more general and that OAM entanglement and atmospheric turbulence as a channel are merely an example case. The authors further use this equivalence as a resource for the characterization of a quantum channel, for qubit states. Within the quantum domain, a tomography requires that multiple measurements be made on an ensemble of quantum systems, therefore, for propagation through atmospheric turbulence the result is also a mixed state in spite of the unitary nature of the turbulence channel. This implies that it is not possible to observe directly the unitary evolution of single photons. However, such a restriction does not exist with classical systems (classical light). This assessment led the authors to propose a characterization of a quantum channel using classical light. Such a system has immediate application in real-time error correction that is key for the implementation of quantum communication links. The work done by the authors is limited to a two-dimensional space since they are using vector vortex modes. This is because the "entanglement" of vector vortex modes is between the polarization degree of freedom and the OAM degree of freedom.

It can be seen that within the quantum domain there still isn't a well-established system for the mitigation against the atmospheric turbulence effects. For instance: while adaptive optics has been shown to work in the study by Leonhard *et al.*, in strong scintillation it would still run into the same issues as the classical systems. Further, the work by Ndagano *et al.* has the obvious limitation of dimension.

1.2 Thesis structure

This thesis can be categorized into two sections: the background information and the contribution(s) of the work done.

The first section consists of Chapters 1 & 2. In Chapter 1 we introduce the thesis through a literature review and also draw out the motivation for this work. In Chapter 2 we discuss the basics that are required to understand the rest of this thesis. The focus on this chapter is on five major concepts: optical fields, angular momentum, quantum optical fields, atmospheric turbulence, and compressive sensing.

The second section of the thesis can be further split into two different sub-parts. In one sub-part we studied the behavior of single photons and entangled quantum systems in atmospheric turbulence. In the other sub-part, we looked at the mitigation of the effects of atmospheric turbulence on high-dimensional quantum systems.

In the first sub-part, we studied the infinitesimal propagation equation (IPE) as it would apply to single photon fields. The IPE was originally formulated for the description of the evolution of entangled photonic quantum systems. However, we show through numerical simulations that the IPE can also be used to describe the crosstalk and thus the evolution of single photon OAM modes, particularly LG modes through atmospheric turbulence. This work is presented in Chapter 3 and is based on articles **P1** and **P2** of the publication list given below. Furthermore, we studied the effect of the atmospheric turbulence on the Hong-Ou-Mandel (HOM) interference effect. We found that under weak scintillation the HOM interference effect is not affected by the atmospheric turbulence. Due to the scattering of the OAM modes, however, there is a reduction in the number of counts that are observed in the experiment. These results are in agreement with the theoretical calculations. This work is presented in Chapter 4 and is based on article **P3** of the publication list given below.

The second contribution of this thesis involves the mitigation of the adverse effects of the atmospheric turbulence on OAM states of light. As a starting point, given the work done by Ndagano *et al.* and noting its limitation to a two-dimensional Hilbert space, we set up to develop a method for the characterization of high-dimensional quantum channels using classical light. We performed calculations that confirm the validity of our approach. This work is presented in Chapter 5 and is based on article **P4** in the publication list. Subsequently, upon noting that the OAM state space is infinite which implies that under severe turbulence conditions it becomes impractical to characterize the full channel matrix for the mitigation. We further investigated the use of compressive sensing as an aid in the determination and characterization of the channel. We show that compressive sensing could be a very useful technique as part of a protocol for the efficient characterization and correction of high-dimensional quantum states under the effect of the atmospheric turbulence. This work is presented in Chapter 6 and is based on article **P5** of the publication list given below.

Finally, we have the conclusions in Chapter 7. Here we summarize the results of the two sub-parts detailed-out above. In the conclusions, we also mention the future work that we intend to undertake.

1.3 Publications

Below is the list of publications that this thesis is based on:

P1 Chemist M. Mabena and Filippus S. Roux. *Optical orbital angular momentum under strong scintillation*. Physical Review A **99**, 013828 (2019).

P2 Chemist M. Mabena, Teboho Bell, and Filippus S. Roux. *Corroboration of a multi-phase screen model*. Free-Space Laser Communications XXXI, International Society for Optics and Photonics, **10910**, 109101T (2019).

P3 Shashi Prabhakar, Chemist M. Mabena, Thomas Konrad, and Filippus S. Roux. *Turbulence and the Hong-Ou-Mandel effect*. Physical Review A **97**, 013835 (2018).

P4 Chemist M. Mabena and Filippus S. Roux. *High-dimensional quantum channel estimation using classical light*. Physical Review A **96**, 053860 (2017).

P5 Chemist M. Mabena and Filippus S. Roux. *Compressive sensing based quantum entanglement preservation of twisted photons*. In Preparation.

Chapter 2

Background theory

2.1 Introduction

In this chapter we discuss all the basic concepts that are necessary to understand the work in this thesis. We start off in Sec. 2.2 with an explicit statement of Maxwell's equations, we continue to set up the Helmholtz equation and further give a brief introduction of the Poynting vector. Section 2.3 is a discussion of angular momentum for optical fields. In Sec. 2.4 we introduce the paraxial approximation and show its consequence with regards to the angular momentum of optical fields. In the same section, we also mention and briefly discuss the most common method for the generation of paraxial optical fields that carry orbital angular momentum. In Sec. 2.5 we introduce quantum states, quantum state tomography, and subsequently discuss the spontaneous parametric downconversion process. Atmospheric turbulence is introduced in Sec. 2.6. We start by discussing some basic statistical concepts, then we introduce the single-phase-screen approximation and derive some results. Lastly, we give a detailed derivation of the infinitesimal propagation equation. Compressive sensing is discussed briefly in Sec. 2.7. Finally, we finish-off by a brief summary.

2.2 Maxwell's equations and optical fields

For completeness, we commence this discussion with an explicit statement of Maxwell's equations in vacuum [104]

$$\nabla \cdot \mathbf{E}(\mathbf{r}, t) = 0, \tag{2.1}$$

$$\nabla \cdot \mathbf{H}(\mathbf{r}, t) = 0, \tag{2.2}$$

$$\nabla \times \mathbf{E}(\mathbf{r}, t) = -\mu_0 \frac{\partial \mathbf{H}(\mathbf{r}, t)}{\partial t}, \tag{2.3}$$

$$\nabla \times \mathbf{H}(\mathbf{r}, t) = \epsilon_0 \frac{\partial \mathbf{E}(\mathbf{r}, t)}{\partial t}, \tag{2.4}$$

where $\mathbf{E}(\mathbf{r},t)$ is the electric field, $\mathbf{H}(\mathbf{r},t)$ is the magnetic field, μ_0 is the magnetic permeability of the vacuum, and ϵ_0 is the electric permitivity of vacuum.[1] The electric and magnetic fields in the above set of equations are real valued functions of space $\mathbf{r} = (x, y, z)$ and time t. Since optical fields are electromagnetic fields, it follows that they are governed by the above set of linear first order coupled-differential equations.

In the most general case, there are in total six scalar functions that are required to describe an electromagnetic field. Using Maxwell's equations we can derive the time dependent wave equation that is satisfied by each of the scalar functions independently

$$\nabla^2 U(\mathbf{r},t) = \frac{1}{c^2}\frac{\partial^2 U(\mathbf{r},t)}{\partial t^2}, \tag{2.5}$$

where $c = \frac{1}{\sqrt{\mu_0\epsilon_0}}$ is the speed of light in vacuum, and $U(\mathbf{r},t)$ is a real valued scalar function of position and time that represents any of the components of the electromagnetic field.

2.2.1 Monochromatic optical fields

In practice, especially in laboratories, it is usually the case that the optical fields of interest have a specific time dependence given as follows

$$U(\mathbf{r},t) = \frac{1}{2}\left(\tilde{u}(\mathbf{r})\exp\left[-\mathrm{i}\omega t\right] + C.C\right) \tag{2.6}$$

where $\tilde{u}(\mathbf{r})$ is a complex valued function of space, ω is the angular frequency of the optical field, and $C.C$ is the complex conjugate of the first term on the right-hand side (RHS) of the above equation. The tilde is used to distinguish complex functions from real functions, however, in cases were no confusion is imminent we will drop it for convenience. Optical fields with the type of time dependence in Eq. (2.6) are referred to as monochromatic fields due to the presence of a single angular frequency term.

A substitution of Eq. (2.6) into the wave equation Eq. (2.5) leads to the Helmholtz equation

$$\nabla^2\tilde{u}(\mathbf{r}) + k_0^2\tilde{u}(\mathbf{r}) = 0, \tag{2.7}$$

where $k_0 = \omega/c$ is the wave number, and we have dropped the complex conjugate contribution for conciseness[2].

[1] Bold face letters represent vectors.

[2] The operation expressed in the Helmholtz equation is linear, therefore it would apply to each of the terms in Eq. (2.6) independently. This implies that to obtain the physical optical field we would need to apply the same operation to the complex conjugate and add the two results.

2.2.2 Poynting vector

One of the most important properties of an electromagnetic field is that it transports energy. The direction of flow of electromagnetic energy is described by the Poynting vector, which can be written as

$$\mathbf{S}(\mathbf{r},t) = \mathbf{E}(\mathbf{r},t) \times \mathbf{H}(\mathbf{r},t). \tag{2.8}$$

Upon invoking the monochromatic condition on the electric and magnetic fields the Poynting vector becomes

$$\begin{aligned} \mathbf{S}(\mathbf{r},t) &= \frac{1}{4}\left[\tilde{\mathbf{E}}(\mathbf{r}) \times \tilde{\mathbf{H}}^*(\mathbf{r}) + \tilde{\mathbf{E}}^*(\mathbf{r}) \times \tilde{\mathbf{H}}(\mathbf{r}) + \tilde{\mathbf{E}}(\mathbf{r}) \times \tilde{\mathbf{H}}(\mathbf{r}) \exp\left(-2\mathrm{i}\omega t\right) \right. \\ &\quad \left. + \tilde{\mathbf{E}}^*(\mathbf{r}) \times \tilde{\mathbf{H}}^*(\mathbf{r}) \exp\left(2\mathrm{i}\omega t\right)\right], \end{aligned} \tag{2.9}$$

where the asterisk $*$ denotes complex conjugation.

The optical section of the electromagnetic spectrum is characterized by rapidly oscillating fields therefore in practice we do not use the instantaneous values of the Poynting vector to describe the flow of energy rather we use the time averaged Poynting vector which is given by

$$\langle \mathbf{S}(\mathbf{r},t) \rangle = \frac{1}{4}\left[\tilde{\mathbf{E}}(\mathbf{r}) \times \tilde{\mathbf{H}}^*(\mathbf{r}) + \tilde{\mathbf{E}}^*(\mathbf{r}) \times \tilde{\mathbf{H}}(\mathbf{r})\right], \tag{2.10}$$

where $\langle \cdot \rangle$ is usually used to denote an ensemble average. However, we use it here to represent a time average since we are working with ergodic processes, and therefore the ensemble and time average give the same result. We have dropped the time dependent terms since they are removed by the averaging process. The average is taken for times greater than the optical field period. The above time average of the Poynting vector further simplifies as follows,

$$\langle \mathbf{S}(\mathbf{r},t) \rangle = \frac{1}{2}\left[\tilde{\mathbf{S}}(\mathbf{r}) + \tilde{\mathbf{S}}^*(\mathbf{r})\right] = \mathrm{Re}\left\{\tilde{\mathbf{S}}(\mathbf{r})\right\}, \tag{2.11}$$

where

$$\tilde{\mathbf{S}}(\mathbf{r}) = \frac{1}{2}\tilde{\mathbf{E}}(\mathbf{r}) \times \tilde{\mathbf{H}}^*(\mathbf{r}), \tag{2.12}$$

will be called the complex Poynting vector and "Re" denotes the real part of the vector. Given Eq. (2.11) for the time averaged Poynting vector, the intensity of an optical field is defined in terms of its magnitude.

2.3 Angular momentum

The linear momentum density of an optical field is given in terms of the Poynting vector (Eq. (2.8)) as follows

$$\mathbf{p} \;=\; \frac{1}{c^2}\mathbf{S}, \tag{2.13}$$

which can also be expressed in terms of the electric and magnetic complex amplitudes through Eq. (2.10). Moving forth we will further drop the tilde that indicates the complex nature of the expressions and also suppress the dependence on position and time for succinctness. In the case that a function is complex or real it will be stated explicitly or it will be clear from context.

While linear momentum is related to the translational properties of the optical field, it has been observed that the optical field can also lead to rotational effects when it interacts with matter [105, 106]. This behavior implies that the optical field itself should possess angular momentum. The simplest form of the angular momentum contained in an optical field can be easily traced to its polarization properties.

The records show that it was Poynting [33] who proposed that the conversion of linearly polarized light into circularly polarized light should lead to an exchange of angular momentum with the optical element. The first ever experiment performed to confirm this proposal was done by Beth [35], who used as the optical element a birefringent wave plate.

Polarization is the most popular source of angular momentum in an optical field, however, it is not the only source. For certain types of optical fields, it has been shown that there is a contribution to the total angular momentum that does not come from the polarization of the optical field [44]. This contribution is referred to as orbital angular momentum (OAM) and is a consequence of the spatial distribution of the optical field. Therefore, the total angular momentum of an optical is due to the orbital (spatial) and spin (polarization) contributions.

Using the monochromatic condition (Eq. (2.6)) and the electric field curl equation (Eq. (2.3)) from Maxwell's equations, the total linear momentum density can be written as follows

$$\mathbf{P} \;=\; \frac{\epsilon_0}{4\mathrm{i}\omega}\int \left[\mathbf{E}^* \times \nabla \times \mathbf{E} - \mathbf{E} \times \nabla \times \mathbf{E}^*\right] \mathrm{d}^3 r, \tag{2.14}$$

where the integral is taken over all space, and the contribution that contains the time dependence goes to zero. Further simplification of the above total linear momentum gives

$$\mathbf{P} \;=\; \frac{\epsilon_0}{2\omega}\mathrm{Im}\int \left[\mathbf{E}^* \cdot (\nabla)\,\mathbf{E} - (\mathbf{E}^* \cdot \nabla)\,\mathbf{E}\right] \mathrm{d}^3 r, \tag{2.15}$$

where "Im" denotes that we are taking the imaginary part, and we have used the identity

$$\mathbf{A} \times \nabla \times \mathbf{B} = \mathbf{A} \cdot (\nabla)\mathbf{B} - (\mathbf{A} \cdot \nabla)\,\mathbf{B}, \tag{2.16}$$

with,

$$\mathbf{A} \cdot (\nabla)\mathbf{B} = \sum_j A_j \nabla B_j, \tag{2.17}$$

where A_j and B_j are the components of the vectors $\mathbf{A}$ and $\mathbf{B}$, respectively. Upon integration by parts and further using the fact that the electric field goes to zero as $|\mathbf{r}| \to \infty$, we find that [107]

$$\mathbf{P} = \frac{\epsilon_0}{2\omega} \mathrm{Im} \int \mathbf{E}^* \cdot (\nabla)\,\mathbf{E}\,\mathrm{d}^3 r. \tag{2.18}$$

Given the momentum density of an optical field, we write the angular momentum density as follows

$$\mathbf{j} = \mathbf{r} \times \mathbf{p}. \tag{2.19}$$

The total angular momentum can be obtained from latter equation by integrating over all space. Furthermore, by also using integration by parts, the divergence criterion (Eq. (2.1)) for the electric field as required by Maxwell's equations, and the fact that the electric field goes to zero as $|\mathbf{r}| \to 0$, the total angular momentum of the optical field becomes [44]

$$\mathbf{J} = \frac{\epsilon_0}{2\omega} \mathrm{Im} \left[\int \mathbf{E}^* \times \mathbf{E}\,\mathrm{d}^3 r \right] + \frac{\epsilon_0}{2\omega} \sum_j \mathrm{Im} \left[\int E_j^* \,(\mathbf{r} \times \nabla)\, E_j\,\mathrm{d}^3 r \right]. \tag{2.20}$$

The first term on the RHS in the above equation is associated with the vectorial nature of the optical field as such is taken to represent the angular momentum with respect to the polarization of the optical field, the so-called spin angular momentum (SAM). The second term is commonly referred to as the orbital term because it has an explicit dependence on the position vector $\mathbf{r}$. However, this may sometimes be misleading since the z-component of the second term may, in the most general case, contain some contribution from the angular momentum associated with the polarization of the optical field [108, 44]. Therefore, the two terms in the above equation cannot be said, in general, to represent the two types of contributions for the total angular momentum separately [109]. In the special case of paraxial optical fields, the total angular momentum of the optical field can be explicitly separated into the polarization and orbital contributions without any ambiguity.

2.4 Paraxial optical fields

Optical fields that propagate predominantly in a given direction are said to be paraxial. They are governed by the paraxial equation which is obtained by way of approximation to the Helmholtz equation (Eq. (2.7)). To derive the paraxial equation we consider, without any loss of generality, a solution of the form

$$u(\mathbf{r}) = A(\mathbf{r}) \exp[\mathrm{i}kz], \tag{2.21}$$

where z is specified as the direction of propagation of the optical field, $A(\mathbf{r})$ is a complex function and thus can be expressed in terms of a real function $a(\mathbf{r})$ denoting an amplitude and another real function $\psi(\mathbf{r})$ denoting a phase such that

$$A(\mathbf{r}) = a(\mathbf{r}) \exp[\mathrm{i}\psi(\mathbf{r})]. \tag{2.22}$$

The solution presented in Eq. (2.21) can be constructed by starting with a plane wave

$$A \exp[\mathrm{i}kz], \tag{2.23}$$

where A is a constant complex amplitude, and modulating the constant amplitude so that it varies with position $\mathbf{r}$, albeit very slowly.

The slow variation of the complex amplitude $A(\mathbf{r})$ with propagation distance can be expressed mathematically as follows

$$\left|\frac{\partial^2 A(\mathbf{r})}{\partial z^2}\right| \ll \left|\frac{\partial^2 A(\mathbf{r})}{\partial x^2}\right|, \left|\frac{\partial^2 A(\mathbf{r})}{\partial y^2}\right|, \left|k\frac{\partial A(\mathbf{r})}{\partial z}\right|. \tag{2.24}$$

Substitution of Eq. (2.21) into Eq. (2.7) and dropping the second derivative of the complex amplitude with respect to z leads to the paraxial equation

$$\nabla_\perp^2 A(\mathbf{r}) + 2\mathrm{i}k\frac{\partial A(\mathbf{r})}{\partial z} = 0, \tag{2.25}$$

where the symbol $\perp$ denotes the transverse part and

$$\nabla_\perp^2 = \frac{\partial^2}{\partial x^2} + \frac{\partial^2}{\partial y^2}, \tag{2.26}$$

is the transverse Laplacian in Cartesian coordinates.

Maxwell's Equations as given in Eq. (2.1) - Eq. (2.4) are based on real electric and magnetic fields, however, the fields can be expressed in complex notation as in Eq. (2.6). In what follows we consider the complex amplitude keeping in mind that the physical field is obtained by also considering the complex conjugate and adding the two together as is done in Eq. (2.6). With this said, we proceed to write (where we have chosen to omit the "tilde" which denotes the complex nature of the functions for succinctness.)

$$\nabla \times \mathbf{E} = \mathrm{i}\omega\mu_0\mathbf{H}, \tag{2.27}$$

and

$$\nabla \times \mathbf{H} = -\mathrm{i}\omega\epsilon_0\mathbf{E}. \tag{2.28}$$

Expanding the former and making **H** subject of the formula we obtain

$$\mathbf{H} = \frac{\mathrm{i}}{\omega\mu_0}\left[\left(\frac{\partial E_z}{\partial y} - \frac{\partial E_y}{\partial z}\right)\hat{x} - \left(\frac{\partial E_z}{\partial x} - \frac{\partial E_x}{\partial z}\right)\hat{y} + \left(\frac{\partial E_y}{\partial x} - \frac{\partial E_x}{\partial y}\right)\hat{z}\right]. \tag{2.29}$$

Let us choose the $x-$component of **H** and substitute the corresponding electric field components as obtained from the expansion of Eq. (2.28)

$$H_x = \frac{1}{\omega\mu_0}\frac{1}{\omega\epsilon_0}\left[\frac{\partial}{\partial y}\left(\frac{\partial H_y}{\partial x} - \frac{\partial H_x}{\partial y}\right) + \frac{\partial}{\partial z}\left(\frac{\partial H_z}{\partial x} - \frac{\partial H_x}{\partial z}\right)\right], \tag{2.30}$$

by making the substitution $c^2 = \frac{1}{\epsilon_0\mu_0}$, $\omega = ck$ and noting that $H_j = h_j \exp[ikz]$ (Eq. (2.21)) we obtain

$$H_x = \frac{\mathrm{i}}{k}\frac{\partial H_z}{\partial x} - \frac{\mathrm{i}}{k}\frac{\partial H_x}{\partial z} + \mathcal{O}(1/k^2) \tag{2.31}$$

where we have used the paraxial equation

$$\frac{\partial h_j}{\partial z} = \frac{\mathrm{i}}{2k}\left[\frac{\partial}{\partial x}\frac{\partial h_j}{\partial x} + \frac{\partial}{\partial y}\frac{\partial h_j}{\partial y}\right], \tag{2.32}$$

and dropping all the terms which are second order and higher in the coefficient $\frac{1}{k}$ we end up with

$$\begin{aligned} H_x &\approx \frac{\mathrm{i}}{k}\left[\frac{\partial H_z}{\partial x} - \frac{\partial H_x}{\partial z}\right] \\ &= -\sqrt{\frac{\epsilon_0}{\mu_0}}E_y. \end{aligned} \tag{2.33}$$

A similar derivation process can be followed to obtain the y component

$$H_y = \sqrt{\frac{\epsilon_0}{\mu_0}}E_x. \tag{2.34}$$

The full expression for the magnetic field can be written in terms of the transverse **H**-field components or the transverse **E**-field components as follows

$$\begin{aligned} \mathbf{H} &= H_x\hat{x} + H_y\hat{y} + Z_0\,\nabla_\perp\cdot\mathbf{H}_\perp\hat{z} \\ &\cong \frac{1}{Z_0}\left[\hat{z}\times\mathbf{E}_\perp + \frac{\mathrm{i}}{k}\,\nabla_\perp\times\mathbf{E}_\perp\right], \end{aligned} \tag{2.35}$$

where $Z_0 = \sqrt{\frac{\mu_0}{\epsilon_0}}$ is the impedance of free-space.

Perhaps, the most surprising and interesting feature of the above equation is that the z component of the **H**-field is not zero. This feature has implications for the flow of the energy as it leads to the transverse flow of energy for the optical field. This feature of non-zero z component is not special to the **H**-field, as it happens it can easily be shown that the **E**-field also possesses a non-zero z component, and can be expressed as follows

$$\mathbf{E} \cong \mathbf{E}_\perp + \frac{\mathrm{i}}{k}\,\nabla_\perp\cdot\mathbf{E}_\perp\hat{z}. \tag{2.36}$$

Next, we delve into the details of the paraxial angular momentum and show the implications of the non-zero z components of the electric and magnetic fields.

2.4.1 Paraxial angular momentum

Given the expression for the paraxial electric and magnetic fields we proceed to establish the paraxial angular momentum. We begin by first obtaining the expression for the time averaged momentum density in terms of $u(\mathbf{r})$ by using Eq. (2.13). To achieve this we substitute Eq. (2.35) and Eq. (2.36) and evaluate the cross product to find

$$\begin{aligned} \mathbf{p} &= \frac{\epsilon_0}{4\omega}\left[\mathrm{i}\left\{u\left(\mathbf{r}\right)\nabla_\perp u^*\left(\mathbf{r}\right) - u^*\left(\mathbf{r}\right)\nabla_\perp u\left(\mathbf{r}\right)\right\}\right. \\ &\quad \left. +\mathrm{i}\left(\alpha\beta^* - \alpha^*\beta\right)\nabla_\perp|u\left(\mathbf{r}\right)|^2\times\hat{z} + 2k|u\left(\mathbf{r}\right)|^2\hat{z}\right], \end{aligned} \tag{2.37}$$

where we have considered[3]

$$\mathbf{E}_\perp = \alpha u\left(\mathbf{r}\right)\hat{x} + \beta u\left(\mathbf{r}\right)\hat{y}, \tag{2.38}$$

α and β are complex numbers associated with the x and y components of the electric field and are subject to the condition

$$|\alpha|^2 + |\beta|^2 = 1. \tag{2.39}$$

These complex numbers are also related to the polarization of the optical field.

[3]In our consideration here, we use fields that are uniformly polarized. However, it is quite straight forward to generalize to non-uniformly polarized optical fields.

The transverse terms which contain derivatives come from the terms of the cross product that contain the z components of the electric and magnetic fields. They represent the transverse flow of electromagnetic energy. In their absence, the only term that is present in the linear momentum density expression is the z component which is related to the intensity of the optical field.

The transverse terms in Eq. (2.37) can be separated into two to represent the two types of linear momentum: One that is associated with the vectorial nature (spin) of the fields and one that is associated with the spatial distribution (orbital) of the fields.

Spin angular momentum

In converting to cylindrical coordinates (r, ϕ, z) we can rewrite the second term in Eq. (2.37) as follows

$$\frac{\epsilon_0}{4\omega}\sigma\nabla_{\perp}|u\left(\mathbf{r}\right)|^2 \times \hat{z} = -\frac{\epsilon_0}{4\omega}\sigma\frac{\partial|u\left(r,\phi,z\right)|^2}{\partial r}\,\hat{\phi}, \tag{2.40}$$

where $\sigma = \mathrm{i}\left(\alpha\beta^* - \alpha^*\beta\right)$. The factor σ comes from the x and the y components of the electric field. Since the complex numbers (α, β) are related to the polarization of the optical field it follows that the σ factor represents the linear momentum density associated with polarization.

Therefore, we proceed to obtain the SAM density by taking the cross product of the transverse radius vector $r\hat{r}$ and RHS of Eq (2.40)

$$j_{sz} = -\frac{\epsilon_0}{4\omega}r\sigma\frac{\partial|u\left(r,\phi,z\right)|^2}{\partial r}\,\hat{z}. \tag{2.41}$$

The above angular momentum density depends on the local gradient and the spin term σ. The value of σ is in the range $-1 \leq \sigma \leq 1$, with equality for left circularly polarized light (-1) and right circularly polarized light (1). It goes to zero for linearly polarized and unpolarized light, as expected since the SAM should be zero for such light.

Orbital angular momentum

Here, while still considering cylindrical coordinates we take a complex function which obeys the paraxial approximation and has the form

$$u(r,\phi,z) = a(r,z)\exp\left[\mathrm{i}\ell\phi\right]. \tag{2.42}$$

Given the above function we find the OAM by substituting into the first term of Eq. (2.37) and taking the cross product with the radius vector $r\hat{r}$

$$j_{oz} = \frac{\epsilon_0}{2\omega}\ell|u\,(r,\phi,z)\,|^2\,\hat{z}. \tag{2.43}$$

This result shows that the OAM density contribution to the total angular momentum density depends on different parameters than the SAM. In this instance, for optical fields with an azimuthal phase dependence, the orbital angular momentum depends on ℓ.

In an effort to elaborate on what the ℓ in the above equations represents we rewrite Eq. (2.42) as follows

$$u(r,\phi,z) = a_0(r,z)\exp\left[\mathrm{i}\,(kz+\ell\phi)\right], \tag{2.44}$$

where we have included the contribution to the phase term that comes from the propagation of the optical field. The form of the complex function allows us to write the condition for the wavefronts of the optical field as follows

$$\ell\phi + kz = const + 2\pi n, \tag{2.45}$$

where $const$ is a constant and n is an integer. This equation can be contrasted with that of the plane wave wavefronts. In the case of a plane wave, the wavefronts can be described as a sequence of planes separated by the wavelength λ of the optical field. In Eq. (2.45) there is an additional contribution in the form of $\ell\phi$. Since ϕ is different across the transverse plane for a given value of r it follows that the surface of constant phase is not as simple as in the plane wave case. Rather, the surface of constant phase as described by Eq. (2.45) is a helical structure. Figure 2.1 shows a schematic of a typical helical wavefront.

A way to think about the emergence of the helicity of the wavefronts is by imagining that the azimuthal dependence modulates the phase distribution of the plane wave at each point on the plane in such a way that each point at a given radius has a different phase value along the $\hat{\phi}$ direction. Such a modulation leads to a modification of the wavefronts of the optical field. Instead of having all the points that give the same phase lay on a plane, the presence of the azimuthal term causes the points of the same phase to lie on a helix along the direction of propagation. This distribution of the phase values is responsible for the helical structure of the wavefronts, and ultimately for the OAM carried by the optical field.

Total angular momentum

In the discussions above we have so far dealt with angular momentum densities, here we put everything together and give the total angular momentum. Doing so requires

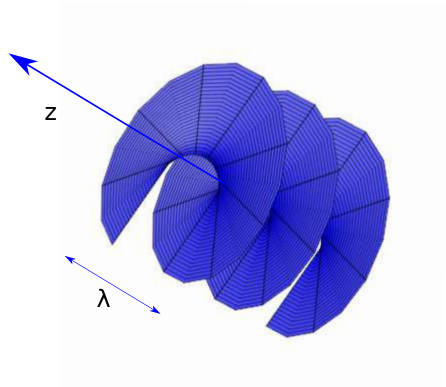

FIGURE 2.1: Typical surface of constant phase, wavefront, for an optical field with non-zero OAM.

integration over all space, however, it is common when working with paraxial optical fields to only consider integration over the transverse plane rather than over all space. This means that the quantity of interest is no longer the total angular momentum rather it is the angular momentum per unit length. Nonetheless, we shall still refer to it as the total angular momentum.

The total angular momentum of the optical field along the direction of propagation is obtained by adding Eq. (2.41) and Eq. (2.43) together and integrating over the transverse plane as follows

$$J_z = \frac{\epsilon_0}{2\omega}\ell \int r|a\,(r,z)\,|^2 \mathrm{d}r\mathrm{d}\phi - \frac{\epsilon_0}{4\omega}\sigma \int r^2 \frac{\partial |a\,(r,z)\,|^2}{\partial r} \mathrm{d}r\mathrm{d}\phi. \tag{2.46}$$

In order to accentuate the two different contributions to the total angular momentum, it is also common to consider the ratio of the total angular momentum to the total energy in the field. The energy in the optical field is calculated as the z component of the linear momentum density multiplied by the speed of light in a vacuum integrated over the transverse plane as follows

$$W = \frac{\epsilon_0}{2} \int r|a\,(r,z)\,|^2 \mathrm{d}r\mathrm{d}\phi. \tag{2.47}$$

Finally, we have after performing integration by parts with respect to r on the second term of Eq. (2.46) and setting $a\,(r,z) = 0$ as $|r| \to \infty$

$$\frac{J_z}{W} = \frac{\ell}{\omega} + \frac{\sigma}{\omega}. \tag{2.48}$$

This result shows that the total angular momentum is given by the sum of the OAM which is a consequence of the azimuthal phase $\exp[\mathrm{i}\ell\phi]$ and the SAM which is due to the polarization dependent term σ.

2.4.2 Optical fields with OAM

The paraxial equation, being a first-order partial differential equation with respect to the propagation direction z, can be solved using any of the available methods for partial differential equations [110]. While all of these methods should give the same result, albeit, with varying degrees of difficulty, it follows that the form of the solution to the paraxial equation is dependent on the symmetry of the coordinate system. For instance, the rectangular symmetry of most cavities results in modes that are super-positions of the Hermite-Gaussian(HG) modes. Solving the same equation under cylindrically symmetric conditions (r, ϕ, z) gives rise to the so-called Laguerre-Gaussian(LG) modes. Both these modes, HG and LG, form a basis[4] set and therefore any optical field can be expanded in their superposition.

In this work, however, we will only focus on the LG modes which can be expressed mathematically as follows

$$\begin{aligned} u_{\ell,p}(r,\phi,z) &= \frac{C_{\ell,p}}{w(z)}\left(\frac{r\sqrt{2}}{w(z)}\right)^{\ell} L_p^{|\ell|}\left(\frac{2r^2}{w^2(z)}\right)\exp\left[-\frac{r^2}{w^2(z)}\right] \\ &\times \exp\left[\mathrm{i}\left(2p+|\ell|+1\right)\arctan\left(\frac{z}{z_R}\right)\right]\exp\left[\mathrm{i}\ell\phi\right] \\ &\times \exp\left[-\frac{\mathrm{i}kr^2z}{2\left(z^2+z_R^2\right)}\right], \end{aligned} \tag{2.49}$$

where p is the radial index, ℓ is the azimuthal index

$$C_{\ell,p} = \sqrt{\frac{2p!}{\pi\left(p+|\ell|\right)!}}, \tag{2.50}$$

is a normalisation constant, $L_p^{\ell}(\cdot)$ is the generalised Laguerre polynomial, $w(\cdot)$ is the width of the LG mode which is given in terms of the beam waist w_0 as

$$w(z) = w_0\sqrt{1+\left(\frac{z}{z_R}\right)^2}, \tag{2.51}$$

with

$$z_R = \frac{\pi\omega_0^2}{\lambda}, \tag{2.52}$$

as the Rayleigh range, and λ is the wavelength of the optical field.

[4] There are two important requirements for a basis: Firstly, the set must consist of linearly independent elements, that is, none of the elements should be expressible in terms of a linear combination of the other elements. Secondly, the basis elements must be complete, that is, each element of the space must be expressible in terms of a linear combination of the basis elements exactly.

The expression of the LG modes can be broken down into two terms, the amplitude term and the phase term

$$u_{\ell,p}(r,\phi,z) = A_{\ell,p}\left(r,z\right)\exp\left[\mathrm{i}\psi_{\ell,p}\left(r,\phi,z\right)\right]. \tag{2.53}$$

The amplitude term determines the intensity of the optical field, whereas the phase term is responsible for the structure of the wavefronts. We will, from this point on, focus mainly on the phase term as it expresses the condition necessary for the optical field to carry OAM. The phase of the LG mode given above can be written out as

$$\psi_{\ell,p}\left(r,\phi,z\right) = -\frac{kr^2 z}{2\left(z^2+z_R^2\right)} + \left(2p+\ell+1\right)\arctan\left(\frac{z}{z_R}\right) + \ell\phi. \tag{2.54}$$

The first term is responsible for the curvature of the wavefronts and thus contributes to the deviation of the optical field from the plane wave structure [42]. The second term is the so-called Gouy phase and represents an offset from the ideal plane or spherical wave [111, 112, 113]. The last term represents the azimuthal dependent phase, this term is responsible for the OAM contained in the LG mode [44]. The OAM carried by the LG mode is proportional to the magnitude of the azimuthal index ℓ. Since OAM is a vector quantity, the magnitude of ℓ determines the amount of OAM carried by the optical field and the sign of ℓ determines the direction of the OAM carried by the optical field.

Since the azimuthal angle ϕ is defined with respect to the cross-section of the optical field, it is easy to see that it has a singularity at the origin, as such the intensity of the LG modes with non-zero ℓ has an annular character. Figure 2.2 shows the intensity profiles and the phases of the LG modes with $p = 0$. LG modes with a non-zero radial index p have rings dependent on the value of p, however, for this work LG modes with the radial index $p = 0$ will be used.

Generation of optical fields with OAM

The LG modes as discussed in the previous section are only useful when they are generated physically. In physical form, they can be used either in applications or to perform experiments. In either case, one has to be able to generate them. As it happens, there are a number of different methods that can be followed in generating such optical fields. However, by far, the computer generated hologram method [52, 114], is the most widely used and preferred way of generating OAM carrying optical fields. This method is generally preferred because of its simplicity and ease of use. A computer generated hologram is formed in a computer as an interference pattern between a reference optical field and some desired optical field pattern. This interference pattern can be displayed on a spatial light modulator (SLM). The SLM is then illuminated

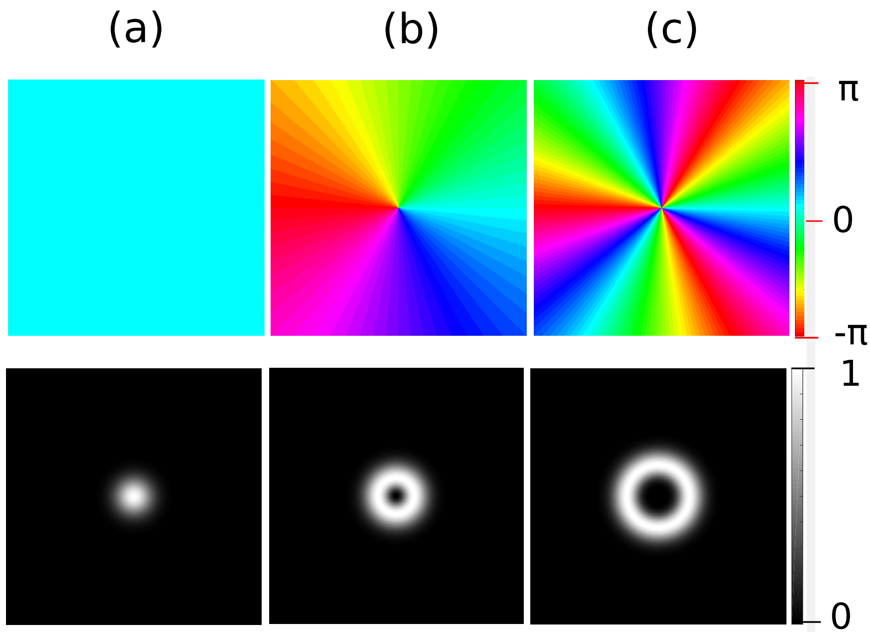

FIGURE 2.2: The intensity and phase patterns for different LG modes with radial index $p = 0$. a) The LG mode with azimuthal index $\ell = 0$; b) LG mode with azimuthal index $\ell = 1$; c) LG mode with $\ell = 3$

.

with the reference optical field to produce the desired optical field pattern. An SLM is a pixelated liquid crystal device that is reconfigurable and gives control over the generation of computer holograms.

While the above described when combined with a diffraction hologram can be used to generate many different transverse distributions of optical fields, it has been shown that to have absolute control over the generation of specific transverse distributions phase masking becomes paramount [115, 116].

The paraxial approximation allows for the separation of OAM and SAM to be physically meaningful, and thus each of these physical quantities to be prepared, and determined independently. This implies that, in principle, we can control the polarization properties and spatial properties of optical fields independently. The discussions, so far, have been based on classical fields. Nonetheless, the properties of light that were discussed extend in a natural way to the case of single photons, which is the domain of quantum mechanics.

2.5 Quantum optical fields

The notion that single photons can be prepared in the SAM and OAM degrees of freedom independently implies a practical realization of photonic quantum digits. However, as is well-known the SAM degree of freedom spans a two-dimensional Hibert space and thus can only be used to describe a qubit. Qubits are defined as quantum binary digits and can be used to represent the simplest unit of quantum information, as will be shown below. The OAM degree of freedom, on the other hand, allows for a much larger Hilbert space and thus can be used to describe the so-called quNits. QuNits are described as high-dimensional quantum digits. The high-dimensionality of the OAM Hilbert space has led to proposals for the use of OAM as a basis for encoding information into single photon fields [117, 63].

The OAM degree of freedom has applications in quantum communication and quantum information processing. It can be used for instance, for secure free-space quantum communication in which information is encoded into a single-photon field. Such a photon could be a member of a composite quantum system where the states of the system are related via quantum entanglement.

2.5.1 Quantum states

Quantum mechanics is a theoretical framework which allows for the description of a vast number of physical phenomena. While much of its formal properties are deeply abstract and counter-intuitive, it has stood the test of experiment. A quantum mechanical description of a physical system is given through a state vector and is usually written in Dirac notation as $|\psi\rangle$. The state vector can be expanded in terms of a suitable basis within a Hilbert space. For a two-dimensional system, one can consider the orthonormal standard basis $\{|0\rangle, |1\rangle\}$. In terms of this basis, the state vector of an arbitrary physical system can be expressed as

$$|\psi\rangle = \alpha|0\rangle + \beta|1\rangle, \tag{2.55}$$

where α and β are complex numbers and are referred to as probability amplitudes. It is expected that such a state vector be normalized for it to characterize a physical system. This condition implies that in the case of an orthonormal basis set

$$|\alpha|^2 + |\beta|^2 = 1. \tag{2.56}$$

In quantum information science, the state vector in Eq. (2.55) is commonly referred to as a qubit. While the qubit expression is sufficient for the description of a single system, it is a common occurrence that one has to describe more than one system. The simplest way to define the state of a composite system made up of two independent subsystem A and subsystem B is in terms of a tensor product as follows

$$|\psi\rangle_{AB} = |A\rangle \otimes |B\rangle, \tag{2.57}$$

where $|A\rangle$ and $|B\rangle$ are single qubit states. The composite system state expressed in Eq. (2.57) is also known as a product state.

Density matrix

The discussion has, upto this point, been based on pure states. The state vector description that has been maintained thus far is only possible for such states. However, there exists other states that cannot be expressed in this way, and these are called mixed states. There is no simple way to describe such states mathematically apart from the introduction of the concept of a density matrix, usually denoted as ρ. The density matrix of a pure state $|\psi\rangle$ is simply

$$\rho = |\psi\rangle\langle\psi|, \tag{2.58}$$

where $|\psi\rangle$ could be a single qubit or a composite system state. The mathematical representation of a mixed state in terms of a density matrix is given as

$$\rho = \sum_j p_j |\psi_j\rangle\langle\psi_j|, \tag{2.59}$$

where p_j is the probability for the quantum system to be in the state $|\psi_j\rangle$. Since the p_j's are probabilities it follows that

$$\sum_j p_j = 1, \tag{2.60}$$

and

$$0 \leq p_j \leq 1 \tag{2.61}$$

also important to note is that $|\psi_j\rangle$ is a pure state. From Eq. (2.59) it can be seen that a mixed state is a weighted-average of an ensemble of pure states. It can further be seen that the description in terms of a density matrix is more general than the state vector representation.

A density matrix is a tool for working with quantum systems and has certain properties that it has to satisfy in order to represent a physical system. The first and most obvious is the requirement that it be Hermitian,

$$\rho = \rho^{\dagger}. \tag{2.62}$$

This is important since it represents real physical systems, and from quantum mechanics we know that observables are represented by Hermitian operators. In order to express the other conditions that the density matrix has to satisfy, we first have to introduce a basis set $|\phi_n\rangle$ that is complete and for convenience, orthonormal. The completeness of the basis implies that

$$\sum_n |\phi_n\rangle\langle\phi_n| = 1, \tag{2.63}$$

and the orthonormality,

$$\langle \phi_n | \phi_m \rangle = \begin{cases} 1, & m = n \\ 0, & \text{otherwise.} \end{cases}$$

In terms of the basis set, we have that any arbitrary pure state, or the i^{th} state of the ensemble representing a mixed state, can be expanded as follows

$$|\psi_i\rangle = \sum_n a_n^{(i)} |\phi_n\rangle, \tag{2.64}$$

where $a_n^{(i)} = \langle \phi_n | \psi_i \rangle$ is the complex amplitude associated with the basis element $|\phi_n\rangle$ in the state $|\psi_i\rangle$. The corresponding mixed state density matrix elements are given as

$$\begin{aligned} \rho_{mn} &= \sum_j \langle \phi_m | \psi_j \rangle \langle \psi_j | \phi_n \rangle p_j \\ &= \sum_j a_n^{(j)} a_m^{(j)*} p_j. \end{aligned} \tag{2.65}$$

It can be shown using Eq. (2.65) that the trace of the density matrix that represents a real physical system is given as

$$\text{trace}\,\{\rho\} = 1. \tag{2.66}$$

This condition is enforced by the requirement of the total probability of the system to be unity.

Given a density matrix ρ that represents some quantum system, it is possible to check its purity by taking the trace of ρ^2. The purity of a quantum system represented in the density matrix formalism is given as

$$\text{trace}\left\{\rho^2\right\} \leq 1. \tag{2.67}$$

In the case of a pure state we that, trace $\left\{\rho^2\right\} = 1$, therefore it follows that the purity of a mixed state is less than unity.

Quantum entanglement

While classical systems are also known to possess correlations between subsystems of a composite system, in quantum mechanics, we can define a different type of correlation between subsystems of a composite system. This feature of quantum systems is called entanglement. The "model" states, for a two-dimensional Hilbert space that represent this deeply eccentric and unintuitive characteristic are the so-called Bell states

$$|\Psi^+\rangle = \frac{1}{\sqrt{2}} \left(|0\rangle_A \otimes |1\rangle_B + |1\rangle_A \otimes |0\rangle_B \right), \tag{2.68}$$

$$|\Psi^-\rangle = \frac{1}{\sqrt{2}} \left(|0\rangle_A \otimes |1\rangle_B - |1\rangle_A \otimes |0\rangle_B \right), \tag{2.69}$$

$$|\Phi^-\rangle = \frac{1}{\sqrt{2}} \left(|0\rangle_A \otimes |0\rangle_B - |1\rangle_A \otimes |1\rangle_B \right), \tag{2.70}$$

$$|\Phi^+\rangle = \frac{1}{\sqrt{2}} \left(|0\rangle_A \otimes |0\rangle_B + |1\rangle_A \otimes |1\rangle_B \right). \tag{2.71}$$

The Bell states, as expressed above are maximally entangled. Mathematically, a quantum system in a pure state is said to be entangled if its state vector cannot be expressed as a product state

$$|\psi\rangle_{AB} \neq |A\rangle \otimes |B\rangle. \tag{2.72}$$

In the density matrix formalism (or for a mixed state) a composite system consisting of subsystem A and subsystem B is said to be entangled if it cannot be written as

$$\rho_{AB} = \sum_j p_j \rho_A^j \otimes \rho_B^j, \tag{2.73}$$

where p_j are the probabilities satisfying the conditions given in Eq. (2.60) and Eq. (2.61), ρ_A^j and ρ_B^j are density matrices for the two subsystems.

For a two dimensional system a common method of quantifying the entanglement in the system is through the computation of the concurrence [118]. The concurrence is defined as follows

$$\mathcal{C}(\rho_{AB}) = \max\{0, \sqrt{\lambda_1} - \sqrt{\lambda_2} - \sqrt{\lambda_3} - \sqrt{\lambda_4}\}, \tag{2.74}$$

where λ_i are the eigenvalues of the matrix

$$R = \rho_{AB}(\sigma_2 \otimes \sigma_2)\rho^*_{AB}(\sigma_2 \otimes \sigma_2), \tag{2.75}$$

in decreasing order, with σ_2 as the Pauli matrix given below and the asterisk denotes complex conjugation.

For a three-dimensional system, qutrits, one of the methods that is used to quantify entanglement is the negativity [79]. The negativity is defined as follows

$$\mathcal{E} = \frac{1}{2} \sum_n \left(\lambda_n - |\lambda_n| \right), \tag{2.76}$$

where λ_n is n^{th} eigenvalue of the partial transpose of the density matrix.

Quantum state tomography

Quantum state tomography is concerned with determining or characterizing the state of a quantum system. For a single qubit system, the density matrix is a 2×2 matrix, and thus can be expressed in terms of the Pauli matrices and the identity matrix as follows

$$\rho = \frac{\sigma_0}{2} + \frac{1}{2}\sum_{n=1}^{3} \alpha_n \sigma_n, \tag{2.77}$$

where α_n represents the coefficient or weight of the n^{th} Pauli matrix,

$$\sigma_1 = \begin{bmatrix} 0 & 1 \\ 1 & 0 \end{bmatrix}$$

$$\sigma_2 = \begin{bmatrix} 0 & -\mathrm{i} \\ \mathrm{i} & 0 \end{bmatrix}$$

$$\sigma_3 = \begin{bmatrix} 1 & 0 \\ 0 & -1 \end{bmatrix},$$

and the 2×2 identity matrix is given by

$$\sigma_0 = \begin{bmatrix} 1 & 0 \\ 0 & 1 \end{bmatrix}.$$

The Pauli matrices as given above are orthogonal

$$\text{trace}\left\{\sigma_m \sigma_n\right\} = \begin{cases} 2, & m = n \\ 0, & m \neq n \end{cases}.$$

The quantum state ρ can be determined by performing measurements on the system that will reveal the coefficients α_n. The most common measurement method in practice and that used in this work is the projective measurement method. However, there are other methods such as the positive operator valued measurement (POVM) method, which is more general than the projective method [3].

A projective measurement is described as an observable M [3], which due to its Hermiticity, has a spectral decomposition

$$M = \sum_m m P_m, \tag{2.78}$$

where P_m is a projective operator onto the eigenspace of M with eigenvalue m. In this formalism, the eigenvalues m correspond to the possible results of the measurement of the observable M. Therefore, given a density matrix ρ the average value or expectation value of the observable M can be determined as follows

$$\begin{aligned} E(M) &= \text{trace}\{\rho M\} \\ &= \sum_m m \,\text{trace}\{\rho P_m\}, \end{aligned} \tag{2.79}$$

where trace $\{\rho P_m\}$ is the probability of obtaining the measurement result m.

Recasting all of the above into the problem of determining the density matrix of an unknown quantum state, we realize that the Pauli matrices are Hermitian, and thus can be subject to a spectral decomposition. The eigenstates of the Pauli matrices are given as

$$\sigma_1 \to \frac{1}{\sqrt{2}}\{|0\rangle + \mathrm{i}|1\rangle, |1\rangle + \mathrm{i}|0\rangle\}, \tag{2.80}$$

$$\sigma_2 \to \frac{1}{\sqrt{2}}\{|0\rangle + |1\rangle, |0\rangle - |1\rangle\}, \tag{2.81}$$

$$\sigma_3 \to \{|0\rangle, |1\rangle\}. \tag{2.82}$$

If we represent the Pauli matrices in terms of their eigenstate decomposition, we find that

$$\sigma_n = |a_n\rangle\langle a_n| - |b_n\rangle\langle b_n|, \tag{2.83}$$

where a_n and b_n are the eigenstates of the corresponding Pauli matrices, as it happens all the Pauli matrices have eigenvalues ± 1 for the respective eigenstates, a_n and b_n. For each of the Pauli matrices, the coefficient is determined as an average value according to

$$\alpha_n = \text{trace}\{\rho\sigma_n\} = \langle a_n|\rho|a_n\rangle - \langle b_n|\rho|b_n\rangle, \tag{2.84}$$

where $\langle\cdot|\rho|\cdot\rangle$ is the probability of obtaining either measurement result.

The density matrix in terms of the coefficients in matrix form is given as

$$\rho = \frac{1}{2}\begin{bmatrix} 1+\alpha_3 & \alpha_2 - \mathrm{i}\alpha_1 \\ \alpha_2 + \mathrm{i}\alpha_1 & 1-\alpha_3 \end{bmatrix}.$$

Earlier we introduced the concept of entanglement, one of the most bizarre predictions of quantum mechanics. Entanglement, as a property of non-classical systems requires more than one system to be meaningful. The density matrix of a two-qubit system can be expressed in terms of the Pauli matrices as follows

$$\rho_{AB} = \frac{1}{4}\left[\sigma_0 \otimes \sigma_0 + \sum_{mn} \alpha_{mn}\sigma_m \otimes \sigma_n + \sum_m \alpha_{m0}\sigma_m \otimes \sigma_0 + \sum_n \alpha_{0n}\sigma_0 \otimes \sigma_n\right], \tag{2.85}$$

where α_{mn} is the coefficient of the corresponding Pauli matrix tensor product, with $m, n = 1, 2, 3$, σ_0 is the 2×2 identity matrix, α_{m0} and α_{0n} are the coefficients for the matrices that are a tensor product of the Pauli matrix and the identity. The basis matrices, which represent the observables with respect to which the measurements are to be made, can be separated into three sets; the first of which is given as follows

$$\begin{aligned}\sigma_m \otimes \sigma_n &= (|a_m\rangle\langle a_m| - |b_m\rangle\langle b_m|) \otimes (|a_n\rangle\langle a_n| - |b_n\rangle\langle b_n|) \\ &= |a_m, a_n\rangle\langle a_n, a_m| - |a_m, b_n\rangle\langle b_n, a_m| - |b_m, a_n\rangle\langle a_n, b_m| \\ &\quad + |b_m, b_n\rangle\langle b_n, b_m|. \end{aligned} \tag{2.86}$$

The average value, and thus coefficient of the above observable becomes

$$\begin{aligned}\alpha_{mn} &= \text{trace}\,\{\rho\sigma_m \otimes \sigma_n\} \\ &= \langle a_m, a_n|\rho|a_m, a_n\rangle - \langle a_m, b_n|\rho|a_m, b_n\rangle - \langle b_m, a_n|\rho|b_m, a_n\rangle \\ &\quad + \langle b_m, b_n|\rho|b_m, b_n\rangle. \end{aligned} \tag{2.87}$$

The second set of measurements is determined as

$$\begin{aligned}\alpha_{0n} &= \text{trace}\,\{\rho\sigma_0 \otimes \sigma_n\} \\ &= \langle a_m, a_n|\rho|a_m, a_n\rangle - \langle a_m, b_n|\rho|a_m, b_n\rangle + \langle b_m, a_n|\rho|b_m, a_n\rangle \\ &\quad - \langle b_m, b_n|\rho|b_m, b_n\rangle, \end{aligned} \tag{2.88}$$

and the last set

$$\begin{aligned}\alpha_{m0} &= \text{trace}\,\{\rho\sigma_m \otimes \sigma_0\} \\ &= \langle a_m, a_n|\rho|a_n, a_m\rangle + \langle a_m, b_n|\rho|b_n, a_m\rangle - \langle b_m, a_n|\rho|a_n, b_m\rangle \\ &\quad - \langle b_m, b_n|\rho|b_n, b_m\rangle. \end{aligned} \tag{2.89}$$

In matrix form, the coefficients are combined according to the Pauli matrices as follows

$$\rho_{AB} = \tfrac{1}{4}\begin{bmatrix} 1+\alpha_{33}+\alpha_{03}+\alpha_{30} & -i\alpha_{31}+\alpha_{32}-i\alpha_{01}+\alpha_{02} & -i\alpha_{13}+\alpha_{23}-i\alpha_{10}+\alpha_{20} & -\alpha_{11}-i\alpha_{12}-i\alpha_{21}+\alpha_{22} \\ i\alpha_{31}+\alpha_{32}+i\alpha_{01}+\alpha_{02} & 1-\alpha_{33}-\alpha_{03}+\alpha_{30} & \alpha_{11}-i\alpha_{12}+i\alpha_{21}+\alpha_{22} & i\alpha_{13}-\alpha_{23}-i\alpha_{10}+\alpha_{20} \\ i\alpha_{13}+\alpha_{23}+i\alpha_{10}+\alpha_{20} & \alpha_{11}+i\alpha_{12}-i\alpha_{21}+\alpha_{22} & 1-\alpha_{33}+\alpha_{03}-\alpha_{30} & i\alpha_{31}-\alpha_{32}-i\alpha_{01}+\alpha_{02} \\ -\alpha_{11}+i\alpha_{12}+i\alpha_{21}+\alpha_{22} & -i\alpha_{13}-\alpha_{23}+i\alpha_{10}+\alpha_{20} & -i\alpha_{31}-\alpha_{32}+i\alpha_{01}+\alpha_{02} & 1+\alpha_{33}-\alpha_{03}-\alpha_{30} \end{bmatrix}.$$

Given the full system density matrix ρ_{AB} it is also possible to extract the density matrix of the subsystems through a partial trace

$$\begin{aligned}\rho_B &= \text{trace}_A\,\{\rho_{AB}\} \\ &= \frac{1}{4}\Bigg[\text{trace}\,(\sigma_0)\,\sigma_0 + \sum_{mn}\alpha_{mn}\text{trace}\,(\sigma_m)\,\sigma_n + \sum_m \alpha_{m0}\text{trace}\,(\sigma_m)\,\sigma_0 \\ &\quad + \sum_n \alpha_{0n}\text{trace}\,(\sigma_0)\,\sigma_n\Bigg]. \end{aligned} \tag{2.90}$$

It follows that the Pauli matrices and the identity matrix satisfy the property

$$\text{trace}\{\sigma_m\} = \begin{cases} 2, & m = 0 \\ 0, & m \neq 0 \end{cases}$$

therefore,

$$\rho_B = \frac{1}{2}\left[\sigma_0 + \sum_n \alpha_{0n}\sigma_n\right]. \tag{2.91}$$

This result shows that we can simply generate the qubit density matrix by just considering the coefficients that correspond to the measurement of the observable $\sigma_0 \otimes \sigma_n$. However, it does not tell us how to use the elements of the full density matrix to obtain the subsystem density matrix given that we do not have access to the individual coefficients. That is, how do we relate the elements of the bigger matrix to the subsystem density matrix? Suppose that we already have the full system density matrix in terms of its elements after performing an actual experiment, how do we use this information to generate a subsystem density matrix? The derivation of this result is left-out, here we only show the final result. Given that the full density matrix is

$$\rho_{AB} = \begin{bmatrix} \rho_{00} & \rho_{01} & \rho_{02} & \rho_{03} \\ \rho_{10} & \rho_{11} & \rho_{12} & \rho_{13} \\ \rho_{20} & \rho_{21} & \rho_{22} & \rho_{23} \\ \rho_{30} & \rho_{31} & \rho_{32} & \rho_{33} \end{bmatrix},$$

it follows that the operation of the partial trace is, in the case that we trace over A (a similar analysis exists for subsystem A by tracing over B)

$$\rho_B = \begin{bmatrix} \rho_{00} + \rho_{22} & \rho_{01} + \rho_{23} \\ \rho_{10} + \rho_{32} & \rho_{11} + \rho_{33} \end{bmatrix}.$$

To confirm that this is correct, we do a simple substitution using the elements in the 4×4 density matrix shown above in terms of the Pauli matrix coefficients

$$\rho_B = \frac{1}{4}\begin{bmatrix} 2 + 2\alpha_{03} & 2\alpha_{02} - 2i\alpha_{01} \\ 2\alpha_{02} + 2i\alpha_{01} & 2 - 2\alpha_{03} \end{bmatrix},$$

This is exactly the result that we obtained in Eq. (2.91). This implies that we can always generate the density matrix of any of the subsystems if we have the full density matrix, even if we do not have direct access to the measured coefficients, individually.

Using this method of generating subsystems from the full density matrix, we can show an interesting feature about entangled systems. Given, for instance the density matrix

$$\rho_{AB} = \frac{1}{2}\begin{bmatrix} 0 & 0 & 0 & 0 \\ 0 & 1 & 1 & 0 \\ 0 & 1 & 1 & 0 \\ 0 & 0 & 0 & 0 \end{bmatrix},$$

corresponding to the Bell state

$$|\Psi^+\rangle = \frac{1}{\sqrt{2}}\left(|0\rangle_A \otimes |1\rangle_B + |1\rangle_A \otimes |0\rangle_B\right), \tag{2.92}$$

it follows that,

$$\rho_A = \rho_B = \frac{1}{2}\begin{bmatrix} 1 & 0 \\ 0 & 1 \end{bmatrix},$$

that is, even though the full system is in a pure state, the subsystems are mixed states. While you know all there is to know about the full system (within the bounds of quantum mechanics), it seems you do not learn anything about the full system from its components when studied individually! This implies that the information in an entangled system is contained in the correlations of the subsystem rather than in the individual systems. This is in stark contrast to how classical systems behave.

This method for the characterization of the density matrix can be generalised to M qubits through

$$\alpha_{n_1 n_2 n_3 \ldots n_M} = \frac{1}{2^M}\text{trace}\left\{\rho\sigma_{n_1} \otimes \sigma_{n_2} \otimes \sigma_{n_3} \cdots \sigma_{n_M}\right\}, \tag{2.93}$$

where each n_i is an element of $\{0, 1, 2, 3\}$. The full M qubit density matrix is therefore given by

$$\rho = \sum_{n_1 n_2 n_3 \ldots n_M} \alpha_{n_1 n_2 n_3 \ldots n_M}\left(\sigma_{n_1} \otimes \sigma_{n_2} \otimes \sigma_{n_3} \cdots \sigma_{n_M}\right). \tag{2.94}$$

So far we have considered quantum systems that are made up of qubits, whether single or composite. However, as was noted in the introduction for this section when motivating for the OAM as a possible degree of freedom to explore, we can also have systems that exist in higher dimensional Hilbert spaces. A quantum system that exists in an N-dimensional Hilbert space is called a quNit and can be expressed mathematically in the density matrix notation as follows

$$\rho = \sum_n \alpha_n \tau_n \tag{2.95}$$

where the α_n are the weight coefficients, τ_n are the generalized Gell-Mann matrices, $n = \{0, 1, 2, ..., N^2 - 1\}$.

The general structure of the generalized Gell-Mann matrices is as follows

Symmetric: $\frac{N(N-1)}{2}$ elements

$$\tau_{sym} = |j\rangle\langle k| + |k\rangle\langle j|, \qquad 0 \leq j \leq k \leq N-1 \tag{2.96}$$

Anti-symmetric: $\frac{N(N-1)}{2}$ elements

$$\tau_{ant} = -\mathrm{i}|j\rangle\langle k| + \mathrm{i}|k\rangle\langle j|, \qquad 0 \leq j \leq k \leq N-1 \tag{2.97}$$

Diagonal: $N-1$ elements

$$\tau_{dia} = \sqrt{\frac{2}{N(N+1)}}\left(\sum_{j}^{l} |j\rangle\langle j| - l|l+1\rangle\langle l+1|\right), \qquad 0 \leq l \leq N-2. \tag{2.98}$$

Other than the fact that we now work in a high-dimensional Hilbert space, the procedure for characterizing a quNit density matrix is the same as that for a qubit. The coefficients of the generalized Gell-Mann matrices can be obtained in the same way

$$\alpha_n = \frac{1}{N}\mathrm{trace}\left(\rho\tau_n\right). \tag{2.99}$$

The generalization to M quNits is also the same

$$\alpha_{n_1 n_2 n_3 \ldots n_M} = \frac{1}{N^M}\mathrm{trace}\left(\rho\tau_{n_1} \otimes \tau_{n_2} \otimes \tau_{n_3} \cdots \otimes \tau_{n_M}\right), \tag{2.100}$$

where each n_i is an element of $\{0, 1, 2 \ldots N^2-1\}$. The full M quNit density matrix is given as

$$\rho = \sum_{n_1 n_2 n_3 \ldots n_M} \alpha_{n_1 n_2 n_3 \ldots n_M}\left(\tau_{n_1} \otimes \tau_{n_2} \otimes \tau_{n_3} \cdots \otimes \tau_{n_M}\right). \tag{2.101}$$

2.5.2 Spontaneous Parametric Down Conversion

The development of quantum optics and related applications such as quantum communication, quantum metrology, etc. depends upon a source for quantum light that has two crucial properties. A source that is capable of generating single photons, and a source that is able to generate pairs of photons that are entangled. Fortunately, spontaneous parametric down conversion (SPDC) is able to do both.

The SPDC is a non-linear optical process that produces a pair of entangled single photons from a single input pump photon. This process occurs when a pump optical field (beam) is incident upon a non-centrosymmetric non-linear optical material with sufficient intensity. Materials with a non-vanishing non-linear susceptibility $\chi^{(2)}$ are non-centrosymmetric [119, 59]. Therefore, it is only in such materials that SPDC is possible.

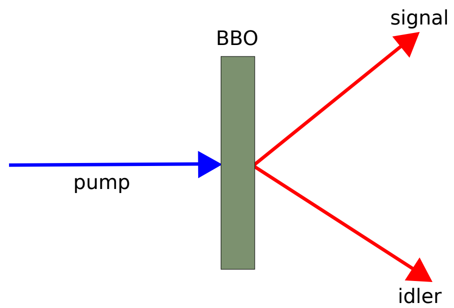

FIGURE 2.3: Schematic illustrating the SPDC process. An input beam is split into two photons, signal and idler, after passing through a non-linear crystal, β-Barium Borate (BBO).

The two photons generated in the SPDC process are referred to as the signal and idler photons. In Fig. 2.3 we show a simplified schematic of the SPDC process. The SPDC process photons satisfy two conditions; the frequency matching condition

$$\omega_\mathrm{p} \quad = \quad \omega_\mathrm{s} + \omega_\mathrm{i}, \tag{2.102}$$

which implies a conservation of energy, and the phase matching condition,

$$n_\mathrm{p}\mathbf{k}_\mathrm{p} \quad = \quad n_\mathrm{s}\mathbf{k}_\mathrm{s} + n_\mathrm{i}\mathbf{k}_\mathrm{i}, \tag{2.103}$$

which implies a conservation of momentum. The subscripts $\mathrm{p}, \mathrm{s}, \mathrm{i}$ are labels for the pump, signal and idler optical fields; the ω represents the angular frequencies, n represents the indices of refraction[5] and the $\mathbf{k}$ represents the vacuum wave vectors for each of the photons. The latter also contains information about the direction of propagation of each of the photons.

The probability amplitude for an input pump photon to be converted into a signal-idler pair is given by

$$\mathcal{P} = \Omega_0 \int \Psi(\mathbf{K}_p)\Psi^*(\mathbf{K}_s)\Psi^*(\mathbf{K}_i)\delta(\Delta\mathbf{K})S(\Delta k_z)\frac{\mathrm{d}^2K_\mathrm{p}}{4\pi^2}\frac{\mathrm{d}^2K_\mathrm{s}}{4\pi^2}\frac{\mathrm{d}^2K_\mathrm{i}}{4\pi^2}, \tag{2.104}$$

where $\Psi(\mathbf{k})$ denotes the respective angular spectra, $\mathbf{K}$ is the two-dimensional transverse wave vector (k_x, k_y), k_z is the longitudinal component of the full three dimensional wave vector $\mathbf{k}$, Ω_0 is an overall conversion efficiency factor that depends on the non-linear susceptibility $\chi^{(2)}$.

The transverse phase matching condition is represented by the Dirac delta function $\delta(\Delta\mathbf{K})$, where its argument is given as

$$\Delta\mathbf{K} = n_\mathrm{p}\mathbf{K}_p - n_\mathrm{s}\mathbf{K}_\mathrm{s} - n_\mathrm{i}\mathbf{K}_\mathrm{i}, \tag{2.105}$$

[5] In general the indices of refraction also depend on frequency.

the longitudinal phase matching condition is represented by the phase matching function [42]

$$S(\Delta k_z) = \mathrm{sinc}\left(\frac{\Delta k_z L}{2}\right), \tag{2.106}$$

where

$$\Delta k_z = n_\mathrm{p} k_{\mathrm{p},z} - n_\mathrm{s} k_{\mathrm{s},z} - n_\mathrm{i} k_{\mathrm{i},z}, \tag{2.107}$$

and L is the crystal longitudinal length.

In this work, we considered the so-called Type I phase matching condition in which the signal and idler have the same polarization - corresponding to the ordinary polarization and ordinary index of refraction, and the pump beam has the orthogonal polarization. That is, $n_\mathrm{s} = n_o = n_\mathrm{i}$.

In the degenerate case, the pump, signal and idler optical fields are related through

$$|\mathbf{k}_\mathrm{s}| = |\mathbf{k}_\mathrm{i}| = \frac{\omega_\mathrm{p}}{2c}. \tag{2.108}$$

Under perfect phase matching conditions it follows that the index of refraction of the pump optical field can be expressed in terms of the index of refraction of the signal and idler optical fields (n_o)

$$n_\mathrm{p} = n_o \cos\phi, \tag{2.109}$$

where ϕ is the angle between the pump optical field wave vector and that of either the signal or idler optical fields. Substituting Eq. (2.109) into Eq. (2.105) we find that

$$\Delta\mathbf{K} = n_o \cos\phi \mathbf{K}_\mathrm{p} - n_o \mathbf{K}_\mathrm{s} - n_o \mathbf{K}_\mathrm{i}. \tag{2.110}$$

In Eq. (2.104) the transverse integrals over the pump optical fields leads to the following expression for the pump field coordinates

$$\mathbf{K}_\mathrm{p} = \frac{\mathbf{K}_\mathrm{s} + \mathbf{K}_\mathrm{i}}{\cos\phi}. \tag{2.111}$$

Let us now turn our attention to the longitudinal phase matching condition. We begin by considering the signal and idler components

$$\begin{aligned} k_{n,z} &= \sqrt{\frac{\omega_n^2}{c^2} - k_{n,x}^2 - k_{n,y}^2} \\ &= \sqrt{\frac{\omega_\mathrm{p}^2}{4c^2} - \frac{\omega_\mathrm{p}^2 \sin^2\phi}{4c^2} - \left(k_{n,x}^2 + k_{n,y}^2 - \frac{\omega_\mathrm{p}^2 \sin^2\phi}{4c^2}\right)} \\ &= \frac{\omega_\mathrm{p}\cos\phi}{2c}\sqrt{1 - \frac{4c^2\left(k_{n,x}^2 + k_{n,y}^2 - \frac{\omega_\mathrm{p}^2\sin^2\phi}{4c^2}\right)}{\omega_\mathrm{p}^2\cos^2\phi}}, \end{aligned} \tag{2.112}$$

where $n = \mathrm{s}, \mathrm{i}$.

Invoking the paraxial approximation, and noticing that the term in the brackets is very small, we apply the binomial approximation to obtain

$$k_{n,z} = \frac{\omega_{\mathrm{p}}\cos\phi}{2c} - \frac{c\left(k_{n,x}^2 + k_{n,y}^2 - \frac{\omega_{\mathrm{p}}^2\sin^2\phi}{4c^2}\right)}{\omega_{\mathrm{p}}\cos\phi}. \tag{2.113}$$

For the pump optical field we have that

$$\begin{aligned} k_{p,z} &= \sqrt{\frac{\omega_{\mathrm{p}}^2}{c^2} - k_{p,x}^2 - k_{p,y}^2} \\ &= \frac{\omega_{\mathrm{p}}}{c}\sqrt{\left(1 - \frac{c^2\left[k_{p,x}^2 + k_{p,y}^2\right]}{\omega_{\mathrm{p}}^2}\right)} \\ &= \frac{\omega_{\mathrm{p}}}{c} - \frac{c\left(k_{p,x}^2 + k_{p,y}^2\right)}{2\omega_{\mathrm{p}}}, \end{aligned} \tag{2.114}$$

where we have also used the paraxial approximation and the binomial approximation.

Now, recalling the longitudinal phase matching condition

$$\Delta k_z = n_o\left[k_{p,z}\cos\phi - k_{\mathrm{s},z} - k_{\mathrm{i},z}\right], \tag{2.115}$$

and substituting the k_z expressions we obtain

$$\begin{aligned} \Delta k_z &= n_o\left[-\frac{|\mathbf{K}_{\mathrm{p}}|^2}{2k_{\mathrm{p}}} + \frac{\left(|\mathbf{K}_{\mathrm{s}}|^2 - \frac{k_{\mathrm{p}}^2\sin^2\phi}{4}\right)}{k_{\mathrm{p}}\cos\phi} + \frac{\left(|\mathbf{K}_{\mathrm{i}}|^2 - \frac{k_{\mathrm{p}}^2\sin^2\phi}{4}\right)}{k_{\mathrm{p}}\cos\phi}\right] \\ &= n_o\left[\frac{\lambda_p|\mathbf{K}_{\mathrm{s}} - \mathbf{K}_{\mathrm{i}}|^2}{4\pi\cos\phi} - \frac{\pi\sin^2\phi}{\lambda_{\mathrm{p}}\cos\phi}\right], \end{aligned} \tag{2.116}$$

where we have made use of Eq. (2.111) and $k_{\mathrm{p}} = 2\pi/\lambda_{\mathrm{p}}$.

The final expression for the probability amplitude becomes

$$\begin{aligned} \mathcal{P} &= \Omega_1 \int \Psi\left(\frac{\mathbf{K}_{\mathrm{s}} + \mathbf{K}_{\mathrm{i}}}{\cos\phi}\right)\Psi^*(\mathbf{K}_s)\Psi^*(\mathbf{K}_i) \\ &\quad \times \mathrm{sinc}\left(n_o L\left[\frac{\lambda_p|\mathbf{K}_{\mathrm{s}} - \mathbf{K}_{\mathrm{i}}|^2}{4\pi\cos\phi} - \frac{\pi\sin^2\phi}{\lambda_{\mathrm{p}}\cos\phi}\right]\right)\frac{\mathrm{d}^2K_{\mathrm{s}}}{4\pi^2}\frac{\mathrm{d}^2K_{\mathrm{i}}}{4\pi^2}, \end{aligned} \tag{2.117}$$

where

$$\Omega_1 = \frac{\Omega_0}{n_o^2\cos^2\phi}. \tag{2.118}$$

It is common to use as the pump optical field a Gaussian function. In such a case, conservation of OAM requires that the signal and the idler optical fields to be OAM modes with opposite azimuthal indices.

2.6 Atmospheric Turbulence

The atmosphere is made of a mixture of different gases, as such, it can be considered as a fluid. Being a fluid, the motion of its particles can be put into two categories: smooth motion, and rough motion. The smooth motion of the atmosphere is called laminar and has a uniform and structured pattern. The rough aspect of the motion of the atmosphere is referred to as turbulence and is not characterized by a structured and uniform flow.

Atmospheric turbulence arises due to random temperature variations, and convective air motion. During turbulent flow, air of different temperatures mixes and leads to the formation of randomly distributed pockets known as turbulent eddies. The eddies have a variety of sizes and temperatures. Since the temperature has an influence on the refractive index of a material(air), it follows that the atmosphere in turbulent flow will have a randomly varying index of refraction. The randomly varying index of refraction of the atmosphere leads to a distortion of light that propagates through the atmosphere.

A complete description, for fully developed turbulence, requires a solution to the Navier-Stokes equations [120]. However, this is a very challenging problem, therefore a lot of effort has also been put in statistical modeling. There are various statistical models [120, 121] that have been proposed to describe and understand the turbulent behavior of the atmosphere, most of which are based on the Kolmogorov theory of turbulence. Kolmogorov developed a statistical theory of turbulence based on physical insight and dimensional analysis [122].

In this work we are not interested in the fundamental aspects of turbulence, rather we are only concerned with the effects of the fluctuations of the index of refraction of the atmosphere on propagating optical fields. Therefore, in the rest of this discussion, we are only going to focus on the effects of atmospheric turbulence with respect to light propagation, rather than on the turbulence itself.

2.6.1 Scintillation

Atmospheric turbulence causes a distortion of the optical field profile. However, depending on the strength of the scintillation, the effect of the atmospheric turbulence can be limited to only the phase of the optical field. As the beam propagates farther or under more severe atmospheric conditions the scintillation becomes strong and the effects of the atmospheric turbulence lead to intensity fluctuations of the optical field.

The intensity fluctuations can be quantified in terms of the scintillation index which can be written as

$$\sigma_I^2 = \frac{\langle I^2 \rangle - \langle I \rangle^2}{\langle I \rangle^2}, \tag{2.119}$$

where I denotes the intensity of the optical field, and the angled brackets $\langle \cdot \rangle$ represent an ensemble average. Another common way of quantifying the strength of the scintillation to be experienced by the optical field is through the Rytov variance

$$\sigma_R^2 = 1.23 C_n^2 k_0^{7/6} z^{11/6}, \tag{2.120}$$

where C_n^2 is the refractive index structure constant, $k_0 = \frac{2\pi}{\lambda}$, and z is the total propagation direction. The scintillation is said to be weak when $\sigma_R^2 < 1$ and strong otherwise.

2.6.2 Kolmogorov power spectral density

An optical field propagating through atmospheric turbulence undergoes a phase perturbation that is imparted along the propagation path. This phase perturbation is a consequence of the fluctuations in the index of refraction of the atmosphere. The fluctuations in the index of refraction can be expressed as

$$\delta n\left(\mathbf{r}\right) = n\left(\mathbf{r}\right) - n_0. \tag{2.121}$$

where n_0 is the average index of refraction of the atmosphere and it has a value that is usually equal to unity. The fluctuations in the index of refraction are usually really small, however over large propagation distances the cumulative effects become substantial. Mathematically, the relationship between the index of refraction fluctuations and the phase is given as

$$\theta(\mathbf{R}) = k_0 \int_0^{\Delta z} \delta n(\mathbf{r}) dz, \tag{2.122}$$

where Δz is the propagation distance over which the light accumulates the above phase. Since $\delta n\left(\mathbf{r}\right)$ is a random function it follows therefore that the phase as given above is also a random function.

As commonly done in statistics, the recommended method for describing the random phase perturbation of the atmosphere is through moments and correlation functions. The autocorrelation function for the phase perturbation can be written as

$$W_\theta\left(\mathbf{R}_1, \mathbf{R}_2\right) = \langle \theta(\mathbf{R}_1)\theta(\mathbf{R}_2) \rangle = k_0^2 \int_0^{\Delta z} \int_0^{\Delta z} \langle \delta n(\mathbf{r}_1) \delta n(\mathbf{r}_2) \rangle dz_1 dz_2. \tag{2.123}$$

While the correlation function may seem an obvious method of characterizing the turbulent atmosphere, it is, however, susceptible to systematic changes of atmospheric conditions. As a consequence, the fluctuations in the results of measured quantities are not always due to pure turbulence. It, therefore, follows that in order to accurately depict the effect of atmospheric turbulence on light propagation (measured quantities) we should be able to use a method which is independent of these intermittent contributions. The structure function is best suited to characterize the random fluctuations in the phase since it is defined in terms of a difference in the phase of the optical and therefore any intermittent contributions are removed automatically. Furthermore, the correlation calculation diverges, in using the structure function instead the divergences are removed. The structure function is given by

$$\begin{aligned} D_\theta(\mathbf{R}_1,\mathbf{R}_2) &= \langle[\theta(\mathbf{R}_1)-\theta(\mathbf{R}_2)]^2\rangle \\ &= W_\theta(\mathbf{R}_1,\mathbf{R}_1)+W_\theta(\mathbf{R}_2,\mathbf{R}_2)-2W_\theta(\mathbf{R}_1,\mathbf{R}_2), \end{aligned} \tag{2.124}$$

this definition can be likened to an Allan variance which is used in atomic clock characterization to prevent divergences in other measures at zero frequency [123].

A look at the structure function expression reveals the ubiquitousness of the term $\langle\delta n(\mathbf{r}_1)\delta n(\mathbf{r}_2)\rangle$. It is usually necessary to have a spectral description of the fluctuations of the index of refraction, therefore instead of dealing with this term directly we will model turbulence through its power spectral density. Using Fourier analysis we relate the index of refraction fluctuations autocorrelation to its power spectral density $\Phi_n(\mathbf{k})$ using the Weiner-Kinchine theorem as follows

$$W_n(\mathbf{r}_1,\mathbf{r}_2)=\langle\delta n(\mathbf{r}_1)\delta n(\mathbf{r}_2)\rangle=\int\Phi_n(\mathbf{k})\exp\left[-\mathrm{i}\left(\mathbf{k}\cdot(\mathbf{r}_1-\mathbf{r}_2)\right)\right]\frac{d^3k}{(2\pi)^3}. \tag{2.125}$$

Using this approach implies that the atmospheric turbulence is completely described by the function $\Phi_n(\mathbf{k})$.

In the case that we consider the atmosphere as homogeneous and isotropic, the index of refraction autocorrelation depends only on the magnitude of the separation $r=|\mathbf{r}_1-\mathbf{r}_2|$, and the power spectral density on $q=|\mathbf{k}|$. Thus, Eq. (2.125) can be rewritten in spherical coordinates as follows

$$W_n(r) = \int_0^\infty q^2\Phi_n(q)\left(\int_0^\pi \sin\theta\mathrm{d}\theta\int_0^{2\pi}\exp[\mathrm{i}qr\cos\alpha]\mathrm{d}\alpha\right)\frac{\mathrm{d}q}{(2\pi)^3}, \tag{2.126}$$

where θ is the polar angle, and α is the azimuthal angle. The above equation is further simplified upon evaluating the α and the θ integrals to obtain

$$W_n(r) = 4\pi\int_0^\infty q^2\Phi_n(q)\frac{\sin(qr)}{qr}\frac{\mathrm{d}q}{(2\pi)^3}. \tag{2.127}$$

Using Eq. (2.124) and Eq. (2.127) it follows that the index of refraction structure function can be written as follows

$$D_n(r) = 8\pi \int_0^\infty q^2 \Phi_n(q) \left(1 - \frac{\sin(qr)}{qr}\right) \frac{dq}{(2\pi)^3}. \tag{2.128}$$

By inverting Eq. (2.128) the index of refraction power spectral density is found to be [124]

$$\Phi_n(q) = \frac{1}{4\pi^2 q^2} \int_0^\infty \frac{\sin(qr)}{qr} \frac{\partial}{\partial r} \left(r^2 \frac{\partial D_n(r)}{\partial r}\right) dr. \tag{2.129}$$

In literature most of the time the Fourier transform does not contain the term $(2\pi)^3$ therefore to align with what is usually done, we make the following transformation: $D_n(r) \rightarrow D_n(r)/\left(2\pi\right)^3$, where $D_n(r)$ is now defined by everything else except the denominator in Eq. (2.128).

In the so-called inertial range [121] where the refractive index structure function is described by the $2/3$ power law we have that [120]

$$D_n\left(r\right) = C_n^2 r^{\frac{2}{3}}, \tag{2.130}$$

Substituting the above structure function into Eq. (2.129) we find that the power spectral density becomes

$$\Phi_n(q) = \frac{0.033\left(2\pi\right)^3 C_n^2}{q^{\frac{11}{3}}} \qquad \text{with} \qquad \frac{2\pi}{L_0} < q < \frac{2\pi}{\ell_0}, \tag{2.131}$$

where L_0 is the outer scale of the atmospheric turbulence and ℓ_0 is the inner scale. This is the famous Kolmogorov power spectral density and it forms the basis of the work in this thesis.

2.6.3 Evolution of optical fields in turbulence

The Helmholtz equation as introduced in Sec.2.2.1 describes the evolution of optical fields in a source free medium. When vacuum is the source free medium we have that the index of refraction is given by $n = 1$. However, in general we can rewrite Eq. (2.7) as

$$\nabla^2 u(\mathbf{r}) + n^2 k_0^2 u(\mathbf{r}) = 0. \tag{2.132}$$

In the case of propagation through atmospheric turbulence the index of refraction is given by Eq. (2.121) with n_0 reliably represented by unity. This implies that after application of the binomial approximation, since we assume that the fluctuation in the index of refraction is very small $\delta n(\mathbf{r}) \ll 1$, we obtain

$$\nabla^2 u(\mathbf{r}) + k_0^2 u(\mathbf{r}) + 2\delta n(\mathbf{r}) k_0^2 u(\mathbf{r}) = 0, \tag{2.133}$$

where $u(\mathbf{r}) = f(\mathbf{r}) \exp[ik_0 z]$. Upon imposing the paraxial condition we get the stochastic parabolic equation

$$\mathrm{i}\partial_z f(\mathbf{r}) = -\frac{1}{2k_0}\nabla_\perp f(\mathbf{r}) + \delta n(\mathbf{r}) k_0 f(\mathbf{r}). \tag{2.134}$$

Next, we are going to discuss two methods that can be used to study the evolution of optical fields in turbulence, particularly the evolution of OAM carrying optical fields.

Single phase screen model

Turbulence, as has already been introduced and also represented in Eq. (2.134), causes random fluctuations in the index of refraction of the atmosphere. These random fluctuations show up in the optical field as scintillation. This occurs through the random phase that the optical acquires as it propagates. Since the fluctuations in the index of refraction are small compared to the average index of refraction, it is usually over long propagation distances that the scintillation becomes evident. This means that scintillation is a function of both the phase perturbation and the diffraction of the optical during propagation.

The evolution of an optical field in weak scintillation is well described by the single phase screen model (SPS)[71]. The single phase screen model is based on the notion that the only effect of the atmospheric turbulence on an optical field is a phase perturbation. In what follows we show how this model can be used to investigate the effect of atmospheric turbulence on OAM carrying optical fields (single photon quantum states).

To begin we can consider an input quantum state that is represented by $|\psi\rangle$ and represent the operation of the atmospheric turbulence by U such that it denotes a phase factor according to

$$U \equiv \exp[\mathrm{i}\theta(\mathbf{R})], \tag{2.135}$$

where $\theta(\mathbf{R})$ is the random phase that depends on the propagation distance and the index of refraction fluctuations as shown in Eq. (2.122). Furthermore, we assume that the atmospheric turbulence is a unitary process which implies that the quantum states can always be taken as pure states.

The evolution of the quantum state is given as follows

$$\rho(z) \quad = \quad U\rho_0 U^\dagger, \tag{2.136}$$

where $\rho_0 = |\psi\rangle\langle\psi|$ is the input quantum state density operator. In terms of a discrete set of orthogonal modes $|\ell\rangle$ we can determine the elements of the density matrix in Eq. (2.136) as follows

$$\rho_{mn}(z) \quad = \quad \langle m|\rho(z)|n\rangle. \tag{2.137}$$

We rewrite the above equation in terms of transverse coordinate space functions by using an identity operator that is given as

$$\mathcal{I} = \int |\mathbf{R}\rangle\langle\mathbf{R}|\mathrm{d}^2 r, \tag{2.138}$$

to obtain

$$\begin{aligned}\rho_{mn}(z) \quad = \quad & \int M_m^*(\mathbf{R}_1)\psi(\mathbf{R}_1)\psi^*(\mathbf{R}_2)M_n(\mathbf{R}_2)\exp\left[\mathrm{i}\left(\theta(\mathbf{R}_1)-\theta(\mathbf{R}_2)\right)\right] \\ & \times \mathrm{d}^2 r_1 \mathrm{d}^2 r_2. \end{aligned}\tag{2.139}$$

The input state wave function is given by

$$\psi(\mathbf{R}) = \langle\mathbf{R}|\psi\rangle. \tag{2.140}$$

The operation of the atmospheric turbulence is represented as follows

$$\langle\mathbf{R}|U|\psi\rangle = \psi(\mathbf{R})\exp\left[\mathrm{i}\theta(\mathbf{R})\right]. \tag{2.141}$$

Finally, the discrete modes which we consider to be the LG modes (Eq. (2.49)) are given as

$$\langle\mathbf{R}|\ell\rangle = M_\ell(\mathbf{R}), \tag{2.142}$$

where the subscript ℓ denotes the azimuthal index of modes .

Since turbulence is a statistical process, to obtain any meaningful information it is usually the case that we take an ensemble average. Taking an ensemble average only affects the exponential function which is introduced by the atmospheric turbulence therefore upon implementing the ensemble average we find that

$$\begin{aligned}\langle\rho_{mn}(z)\rangle \quad = \quad & \int M_m^*(\mathbf{R}_1)\psi(\mathbf{R}_1)\psi^*(\mathbf{R}_2)M_n(\mathbf{R}_2)\langle\exp\left[\mathrm{i}\left(\theta(\mathbf{R}_1)-\theta(\mathbf{R}_2)\right)\right]\rangle \\ & \times \mathrm{d}^2 r_1 \mathrm{d}^2 r_2 \\ = \quad & \int M_m^*(\mathbf{R}_1)\psi(\mathbf{R}_1)\psi^*(\mathbf{R}_2)M_n(\mathbf{R}_2)\exp\left[-\frac{1}{2}D\left(|\Delta\mathbf{R}|\right)\right] \\ & \times \mathrm{d}^2 r_1 \mathrm{d}^2 r_2, \end{aligned}\tag{2.143}$$

where we have made the substitution

$$\langle\exp\left[\mathrm{i}\theta(\mathbf{R}_1)-\mathrm{i}\theta(\mathbf{R}_2)\right]\rangle = \exp\left[-\frac{1}{2}D\left(|\Delta\mathbf{R}|\right)\right] \tag{2.144}$$

with $\Delta\mathbf{R} = \mathbf{R}_1 - \mathbf{R}_2$ and the structure function is given by [121]

$$D\left(|\Delta\mathbf{R}|\right) = 6.88\left(\frac{\Delta\mathbf{R}}{r_0}\right)^{5/3}, \tag{2.145}$$

where

$$r_0 = 0.185\left(\frac{\lambda^2}{C_n^2 z}\right)^{3/5}, \tag{2.146}$$

is the Fried parameter. Due to tractability reasons when performing the calculation in Eq. (2.143), it is common to use instead of the structure function given in Eq. (2.145) the quadratic structure function [85]

$$D_{\text{quad}}\left(\Delta\mathbf{R}\right) = 6.88\left(\frac{\Delta\mathbf{R}}{r_0}\right)^{2}. \tag{2.147}$$

Infinitesimal propagation equation

The SPS model gives reliable estimates to the effects of atmospheric turbulence under weak scintillation conditions. However, in strong scintillation, we require a different formulation. This is the domain of the infinitesimal propagation equation (IPE) [90, 91, 82]. The IPE is based on the multi-phase screen model. That is, it incorporates the incremental effect of the atmosphere on the optical field. The reason that the SPS becomes unreliable in strong scintillation is that it does not take into account intensity fluctuations and other propagation effects such as diffraction. Therefore, to accurately model the evolution of the optical field in atmospheric turbulence requires a model that takes these aspects into account.

To commence the derivation of the IPE we recall that derivatives can be evaluated with ease in the Fourier domain. Therefore, we re-express the functions in Eq. (2.134) in terms of their transverse inverse Fourier transforms as follows

$$\partial_z F\left(\mathbf{K}, z\right) = \frac{\mathrm{i}}{k_0}|\mathbf{K}|^2 F\left(\mathbf{K}, z\right) - \mathrm{i}k_0 \int \delta N\left(\mathbf{K}-\mathbf{q}, z\right) F\left(\mathbf{q}, z\right)\frac{d^2q}{(2\pi)^2}. \tag{2.148}$$

In quantum optics it is common to express the state of the optical field in terms of a density matrix

$$\begin{aligned}\rho\left(z\right) &= |\psi\rangle\langle\psi| \\ &= \int\int |\mathbf{K}_1\rangle F\left(\mathbf{K}_1, z\right) F^*\left(\mathbf{K}_2, z\right)\langle\mathbf{K}_2|\frac{d^2K_1}{(2\pi)^2}\frac{d^2K_2}{(2\pi)^2},\end{aligned} \tag{2.149}$$

where,

$$|\psi\rangle = \int |\mathbf{K}\rangle F\left(\mathbf{K}, z\right)\frac{d^2K}{(2\pi)^2}. \tag{2.150}$$

The above equation shows that $|\psi\rangle$ has a z dependence through the wave-function $F(\cdot)$, and $|\mathbf{K}\rangle$ is the basis for the transverse Fourier space.

Given the z dependence we can study the evolution of the density matrix ρ by an infinitesimal change in the z direction

$$\partial_z \rho(z) = \int\int |\mathbf{K}_1\rangle \partial_z \left[F(\mathbf{K}_1, z) F^*(\mathbf{K}_2, z)\right] \langle \mathbf{K}_2| \frac{d^2K_1}{(2\pi)^2} \frac{d^2K_2}{(2\pi)^2}. \tag{2.151}$$

By application of the product rule of differentiation to the term that contains the z dependence using (Eq. 2.148), making the substitution

$$\rho(\mathbf{K}_1, \mathbf{K}_2, z) = F(\mathbf{K}_1, z) F^*(\mathbf{K}_2, z), \tag{2.152}$$

and performing an integration along the z direction we obtain

$$\begin{aligned} \rho(\mathbf{K}_1, \mathbf{K}_2, z) \;=\;& \rho(\mathbf{K}_1, \mathbf{K}_2, z_0) + \frac{\mathrm{i}}{2k_0}\left(|\mathbf{K}_1|^2 - |\mathbf{K}_2|^2\right) \int_{z_0}^{z} \rho(\mathbf{K}_1, \mathbf{K}_2, z_1)\, dz_1 \\ & - \mathrm{i}k_0 \int_{z_0}^{z} \int \delta N(\mathbf{K}_1 - \mathbf{q}, z_1)\, \rho(\mathbf{q}, \mathbf{K}_2, z_1) \frac{d^2q}{(2\pi)^2} dz_1 \\ & + \mathrm{i}k_0 \int_{z_0}^{z} \int \delta N^*(\mathbf{K}_2 - \mathbf{q}, z_1)\, \rho(\mathbf{K}_1, \mathbf{q}, z_1) \frac{d^2q}{(2\pi)^2} dz_1. \end{aligned} \tag{2.153}$$

It is common when working with statistical quantities to perform ensemble averages as a means of removing the randomness, albeit in this case, the case of the above equation, performing an ensemble average does not lead to particularly useful results due to the statistics of the atmospheric turbulence

$$\langle \delta n(\cdot) \rangle = 0, \tag{2.154}$$

that is, the fluctuations in the refractive index of the atmosphere have zero mean. However, we can overcome this hurdle by application of the Dyson expansion. The Dyson expansion is a recursive substitution of the density matrix by itself evaluated at prior values of z. For instance, we can replace the density matrix $\rho(\cdot, z_1)$ on the right-hand side of Eq. (2.153) at some position z_1 in terms of itself at an earlier position z_2

$$\begin{aligned} \rho(\mathbf{K}_1, \mathbf{K}_2, z_1) \;=\;& \rho(\mathbf{K}_1, \mathbf{K}_2, z_0) + \frac{\mathrm{i}}{2k_0}\left(|\mathbf{K}_1|^2 - |\mathbf{K}_2|^2\right) \int_{z_0}^{z_1} \rho(\mathbf{K}_1, \mathbf{K}_2, z_2)\, dz_2 \\ & - \mathrm{i}k_0 \int_{z_0}^{z_1} \int \delta N(\mathbf{K}_1 - \mathbf{q}, z_2)\, \rho(\mathbf{q}, \mathbf{K}_2, z_2) \frac{d^2q}{(2\pi)^2} dz_2 \\ & + \mathrm{i}k_0 \int_{z_0}^{z_1} \int \delta N^*(\mathbf{K}_2 - \mathbf{q}, z_2)\, \rho(\mathbf{K}_1, \mathbf{q}, z_2) \frac{d^2q}{(2\pi)^2} dz_2. \end{aligned} \tag{2.155}$$

Substitution of the above equation into Eq. (2.153) gives

$$
\begin{aligned}
\rho\left(\mathbf{K}_1,\mathbf{K}_2,z\right) &= \rho\left(\mathbf{K}_1,\mathbf{K}_2,z_0\right)+\frac{\mathrm{i}}{2k_0}\left(|\mathbf{K}_1|^2-|\mathbf{K}_2|^2\right)\int_{z_0}^{z}\rho\left(\mathbf{K}_1,\mathbf{K}_2,z_0\right)dz_1 \\
&-\left[\frac{1}{k_0}\left(|\mathbf{K}_1|^2-|\mathbf{K}_2|^2\right)\right]^2\int_{z_0}^{z_1}\int_{z_0}^{z_2}\rho\left(\mathbf{K}_1,\mathbf{K}_2,z_2\right)dz_2dz_1 \\
&+k_0^2\int_{z_0}^{z_1}\int_{z_0}^{z_2}\int\Big\{\delta N\left(\mathbf{K}_1-\mathbf{q},z_1\right)\delta N\left(\mathbf{q}-\mathbf{q}',z_2\right)\rho\left(\mathbf{q}',\mathbf{K}_2,z_2\right) \\
&-\delta N\left(\mathbf{K}_1-\mathbf{q},z_1\right)\delta N^*\left(\mathbf{K}_2-\mathbf{q}',z_2\right)\rho\left(\mathbf{q},\mathbf{q}',z_2\right) \\
&-\delta N\left(\mathbf{K}_1-\mathbf{q}',z_2\right)\delta N^*\left(\mathbf{K}_2-\mathbf{q},z_1\right)\rho\left(\mathbf{q}',\mathbf{q},z_2\right) \\
&+\delta N^*\left(\mathbf{K}_2-\mathbf{q},z_1\right)\delta N^*\left(\mathbf{q}-\mathbf{q}',z_2\right)\rho\left(\mathbf{K}_1,\mathbf{q}',z_2\right)\Big\} \\
&\times\frac{d^2q}{(2\pi)^2}\frac{d^2q'}{(2\pi)^2}dz_2dz_1,
\end{aligned}
\tag{2.156}
$$

where we have eliminated terms that involve a single refractive index in anticipation of the ensemble average.

Application of the Dyson expansion one last time before we take the ensemble average allows for the removal of the density matrix from the z integrals, finally taking the ensemble average leads to

$$
\begin{aligned}
\rho\left(\mathbf{K}_1,\mathbf{K}_2,z\right) &= \rho\left(\mathbf{K}_1,\mathbf{K}_2,z_0\right)+\frac{\mathrm{i}}{2k_0}\left(|\mathbf{K}_1|^2-|\mathbf{K}_2|^2\right)\int_{z_0}^{z}\rho\left(\mathbf{K}_1,\mathbf{K}_2,z_0\right)dz_1 \\
&+k_0^2\int\Big\{\rho\left(\mathbf{q}',\mathbf{K}_2,z_0\right)\int_{z_0}^{z_1}\int_{z_0}^{z_2}\langle\delta N\left(\mathbf{K}_1-\mathbf{q},z_1\right)\delta N\left(\mathbf{q}-\mathbf{q}',z_2\right)\rangle dz_2dz_1 \\
&-\rho\left(\mathbf{q},\mathbf{q}',z_0\right)\int_{z_0}^{z_1}\int_{z_0}^{z_2}\langle\delta N\left(\mathbf{K}_1-\mathbf{q},z_1\right)\delta N^*\left(\mathbf{K}_2-\mathbf{q}',z_2\right)\rangle dz_2dz_1 \\
&-\rho\left(\mathbf{q}',\mathbf{q},z_0\right)\int_{z_0}^{z_1}\int_{z_0}^{z_2}\langle\delta N\left(\mathbf{K}_1-\mathbf{q}',z_2\right)\delta N^*\left(\mathbf{K}_2-\mathbf{q},z_1\right)\rangle dz_2dz_1 \\
&+\rho\left(\mathbf{K}_1,\mathbf{q}',z_0\right)\int_{z_0}^{z_1}\int_{z_0}^{z_2}\langle\delta N^*\left(\mathbf{K}_2-\mathbf{q},z_1\right)\delta N^*\left(\mathbf{q}-\mathbf{q}',z_2\right)\rangle dz_2dz_1\Big\} \\
&\times\frac{d^2q}{(2\pi)^2}\frac{d^2q'}{(2\pi)^2}.
\end{aligned}
\tag{2.157}
$$

In applying the Dyson expansion again, the second term in Eq. (2.156) will contain terms with a single index of refraction, furthermore the terms that do not contain any index of refraction will lead to a second-order term in Δz after evaluating the z integrals. Since the single index of refraction goes to zero with an ensemble average, and the terms that are second order in Δz are very small, we have thus eliminated them from the final expression. The recursive substitution in the remaining terms leads to higher order terms in the index of refraction, since the fluctuations are small we have also excluded these terms from the final expression on the ground of smallness.

The z integrals of the ensemble average can be evaluated in a series of steps. First we express the index of refraction fluctuations in terms of the power spectral density and some random function

$$\delta n(\mathbf{k}) = \chi(\mathbf{k}) \sqrt{\frac{\Phi_n(\mathbf{k})}{\Delta_k^3}}, \tag{2.158}$$

where $\chi(\cdot)$ is a Gaussian random variable with zero-mean and correlation

$$\langle \chi(\mathbf{k}_1) \chi^*(\mathbf{k}_2) \rangle = \delta(\mathbf{k}_1 - \mathbf{k}_2) (2\pi\Delta_k)^3, \tag{2.159}$$

with the property[6] $\chi^*(\mathbf{k}) = \chi(-\mathbf{k})$, and Δ_k is a correlation length in the Fourier domain that is introduced by way of dimensional analysis. The second step involves taking a product of the index of refraction fluctuation with its conjugate. Fourier transforming along the z direction, and taking the ensemble average leads to

$$\begin{aligned} \langle \delta N(\mathbf{K}_1, z_1) \delta N^*(\mathbf{K}_2, z_2) \rangle = & \int \langle \chi(\mathbf{k}_1) \chi^*(\mathbf{k}_2) \rangle \sqrt{\frac{\Phi_n(\mathbf{k}_1) \Phi_n^*(\mathbf{k}_2)}{\Delta_k^3 \Delta_k^3}} \\ & \times \exp[-ik_{z_1} z_1] \exp[ik_{z_2} z_2] \\ & \times \frac{dk_{z_1}}{2\pi} \frac{dk_{z_1}}{2\pi}. \end{aligned} \tag{2.160}$$

Substituting the correlation of the $\chi(\cdot)$ function, evaluating one of the k_z integrals, and using the fact that the power spectral density $\Phi_n(\mathbf{k})$ is real we obtain

$$\begin{aligned} & \langle \delta N(\mathbf{K}_1, z_1) \delta N^*(\mathbf{K}_2, z_2) \rangle \\ = 4\pi^2 & \int \delta(\mathbf{K}_1 - \mathbf{K}_2) \Phi_n(\mathbf{K}_1, k_z) \exp[-ik_z(z_1 - z_2)] \frac{dk_z}{2\pi}. \end{aligned} \tag{2.161}$$

The last step requires that we invoke the z-integrals. Since the only term that depends on z is the exponential we can remove the terms that are constant with respect to z

$$\begin{aligned} & \int_{z_0}^{z} \int_{z_0}^{z_1} \exp[-ik_z(z_1 - z_2)] \, dz_2 dz_1 \\ = & \frac{1 - \cos(k_z \Delta z)}{k_z^2} + \frac{\sin(k_z \Delta z) - k_z \Delta z}{k_z^2}, \end{aligned} \tag{2.162}$$

where $\Delta z = z_1 - z_2$. Since the power spectral density $\Phi_n(\mathbf{k})$ is an even function, it follows that we can ignore the imaginary term since it will not contribute to the final expression. In accordance with the Markov approximation we can assume that the turbulent atmosphere is uncorrelated along the propagation distance. Therefore we can set $k_z = 0$, as such we can remove the power spectral density $\Phi_0(\mathbf{K}) \equiv \Phi_n(\mathbf{K}, 0)$ from the k_z integral which leads to

$$\int \frac{1 - \cos(k_z \Delta z)}{k_z^2} \frac{dk_z}{2\pi} = \frac{\Delta z}{2}. \tag{2.163}$$

[6] δn is an asymmetric real valued function.

Putting everything together we obtain

$$\int_{z0}^{z}\int_{z_0}^{z_1}\langle\delta N\left(\mathbf{K}_1,z_1\right)\delta N^*\left(\mathbf{K}_2,z_2\right)\rangle dz_2 dz_1 \tag{2.164}$$

$$= 2\pi^2\Delta z\delta\left(\mathbf{K}_1-\mathbf{K}_2\right)\Phi_0\left(\mathbf{K}_1\right). \tag{2.165}$$

A similar analysis can be done for the term $\langle\delta N\left(\mathbf{k}_1\right)\delta N\left(\mathbf{k}_2\right)\rangle$ and its conjugate $\langle\delta N^*\left(\mathbf{k}_1\right)\delta N^*\left(\mathbf{k}_2\right)\rangle$ by using the property $\chi^*\left(\mathbf{k}\right)=\chi\left(-\mathbf{k}\right)$, and the fact that the power spectral density is an even function $\Phi_n\left(\mathbf{k}\right)=\Phi_n\left(-\mathbf{k}\right)$. Evaluating all other integrals, substitution of the results into Eq. (2.157), and re-expressing the equation as a differential equation we obtain

$$\begin{aligned}\partial_z\rho\left(\mathbf{K}_1,\mathbf{K}_2,z\right) \quad = \quad & \frac{\mathrm{i}}{2k_0}\left(|\mathbf{K}_1|^2-|\mathbf{K}_2|^2\right)\rho\left(\mathbf{K}_1,\mathbf{K}_2,z\right)\\ & +k_0^2\int\Phi_0\left(\mathbf{q}\right)\left[\rho\left(\mathbf{K}_1-\mathbf{q},\mathbf{K}_2-\mathbf{q},z\right)-\rho\left(\mathbf{K}_1,\mathbf{K}_2,z\right)\right]\\ & \times\frac{d^2q}{4\pi^2}.\end{aligned} \tag{2.166}$$

The convolution in the above equation comes from the refractive indices that had the correct combination, that is a multiplication of the indices of refraction with one of them being a complex conjugate, and the normal multiplication (second term in the square brackets) between the power spectral density and the density matrix is due to the multiplication that had either both normal indices of refraction or both conjugates. Nonetheless, the differential equation given in Eq. (2.166) cannot be readily solved. In the next section, we elaborate further on the steps that are necessary to solve it, and therefore continue to find its solution.

The solution to the IPE

In deriving the IPE, we have converted one differential equation Eq. (2.134) into another Eq. (2.166). Therefore, we still have to embark in a process of finding the solution. As a starting point, we use the old trick in solving differential equations, that is, we guess the form solution which is given as

$$\rho\left(\mathbf{K}_1,\mathbf{K}_2,z\right)=H\left(\mathbf{K}_1,\mathbf{K}_2,z\right)\exp\left[\frac{\mathrm{i}}{2k_0}\left(|\mathbf{K}_1|^2-|\mathbf{K}_2|^2\right)z\right]. \tag{2.167}$$

From the above ansatz we proceed by substituting in Eq. (2.166) to further obtain

$$\begin{aligned}\partial_z\rho\left(\mathbf{K}_1,\mathbf{K}_2,z\right) \quad = \quad & \frac{\mathrm{i}}{2k_0}\left(|\mathbf{K}_1|^2-|\mathbf{K}_2|^2\right)\rho\left(\mathbf{K}_1,\mathbf{K}_2,z\right)\\ & +\partial_z H\left(\mathbf{K}_1,\mathbf{K}_2,z\right)\exp\left[\frac{\mathrm{i}}{2k_0}\left(|\mathbf{K}_1|^2-|\mathbf{K}_2|^2\right)z\right].\end{aligned} \tag{2.168}$$

When we set Eq. (2.166) equal to the above equation Eq. (2.168) we find that the first terms cancel out and we are left with the following expression

$$\begin{aligned} \partial_z H(\mathbf{K}_1, \mathbf{K}_2, z) &= k_0^2 \int \Phi_0(\mathbf{q}) \left\{ H(\mathbf{K}_1 - \mathbf{q}, \mathbf{K}_2 - \mathbf{q}, z) \exp\left[\frac{\mathrm{i}}{k_0} z (\mathbf{K}_2 - \mathbf{K}_1) \cdot \mathbf{q}\right] \right. \\ &\quad \left. - H(\mathbf{K}_1, \mathbf{K}_2, z) \right\} \frac{d^2 q}{4\pi^2}. \end{aligned} \tag{2.169}$$

Now, to facilitate the solution to the IPE we further define new variables, the sum and difference variables

$$\mathbf{K}_s = \frac{1}{2}[\mathbf{K}_1 + \mathbf{K}_2] \qquad \mathbf{K}_d = \mathbf{K}_1 - \mathbf{K}_2, \tag{2.170}$$

with

$$\mathbf{K}_1 = \mathbf{K}_s + \frac{1}{2}\mathbf{K}_d \qquad \mathbf{K}_2 = \mathbf{K}_s - \frac{1}{2}\mathbf{K}_d. \tag{2.171}$$

In terms of these new variables we can make the following assignment

$$H(\mathbf{K}_1, \mathbf{K}_2, z) \longrightarrow \mathcal{H}(\mathbf{K}_s, \mathbf{K}_d, z). \tag{2.172}$$

This leads to the restatement of Eq. (2.169) accordingly

$$\begin{aligned} \partial_z \mathcal{H}(\mathbf{K}_s, \mathbf{K}_d, z) &= k_0^2 \int \Phi_0(\mathbf{q}) \left\{ \mathcal{H}(\mathbf{K}_s - \mathbf{q}, \mathbf{K}_s, z) \exp\left[-\frac{\mathrm{i}}{k_0} z \mathbf{K}_d \cdot \mathbf{q}\right] \right. \\ &\quad \left. - \mathcal{H}(\mathbf{K}_s, \mathbf{K}_d, z) \right\} \frac{d^2 q}{4\pi^2}. \end{aligned} \tag{2.173}$$

We further take the inverse Fourier transform in the sum coordinate

$$\begin{aligned} \partial_z T(\mathbf{x}, \mathbf{K}_d, z) &= -k_0^2 T(\mathbf{x}, \mathbf{K}_d, z) \int \Phi(\mathbf{q}) \left\{ \exp\left[-\mathrm{i}\left(\frac{z}{k_0}\mathbf{K}_d + \mathbf{x}\right) \cdot \mathbf{q}\right] - 1 \right\} \\ &\quad \times \frac{d^2 q}{4\pi^2}, \end{aligned} \tag{2.174}$$

where

$$T(\mathbf{x}, \mathbf{K}_d, z) = \int \mathcal{H}(\mathbf{K}_s, \mathbf{K}_d, z) \exp[-\mathrm{i}\mathbf{K}_s \cdot \mathbf{x}] \frac{d^2 K_s}{(2\pi)^2}. \tag{2.175}$$

The solution to Eq. (2.174) is given as

$$T(\mathbf{x}, \mathbf{K}_d, z) = T_0(\mathbf{x}, \mathbf{K}_d) \exp\left[-k_0^2 \int_0^z Q\left(\frac{z'}{k_0}\mathbf{K}_d + \mathbf{x}\right) dz'\right], \tag{2.176}$$

with

$$Q(\mathbf{y}) = \int \Phi_0(\mathbf{q}) \{1 - \exp[-\mathrm{i}\mathbf{y} \cdot \mathbf{q}]\} \frac{d^2 q}{4\pi^2}. \tag{2.177}$$

The above expression can be simplified and also the integral evaluated with ease if we invoke the isotropy and homogeneity of the atmospheric turbulence

$$Q\left(y\right)=\frac{1}{4\pi^{2}}\int\Phi_{1}\left(q\right)\left\{1-\exp\left[-iyq\cos\phi\right]\right\}qdqd\phi. \tag{2.178}$$

The above expression can further be simplified by considering each term separately, for instance the first term is given by

$$Q_{A}(y) \quad = \quad \frac{1}{2\pi}\int\Phi_{1}\left(q\right)qdq \tag{2.179}$$

where we have already evaluated the ϕ integral. We further consider the power spectral density

$$\Phi_{1}(q;\kappa)=\frac{0.033(2\pi)^{3}C_{n}^{2}}{\left(|q|^{2}+\kappa^{2}\right)^{11/6}} \tag{2.180}$$

where κ is introduced as a means of dealing with the singularity at $q=0$. Substituting the above power spectral density into Eq. (2.179), and evaluating the integral we obtain

$$Q_{A}(y)=\frac{0.396\pi^{2}C_{n}^{2}}{5\kappa^{5/3}}. \tag{2.181}$$

The second term is a bit involved, it requires for simplification the Jacobi-Anger identity such that

$$Q_{B}\left(y\right)=\frac{1}{2\pi}\int\Phi_{1}\left(q\right)J_{0}\left(yq\right)qdq. \tag{2.182}$$

where J_0 is the Bessel function of the first kind. The above integral is a Henkel-Nicholson type integral and is given by

$$Q_{B}\left(y\right)=\frac{0.396C_{n}^{2}\pi^{2}}{5\kappa^{5/6}}\frac{2^{1/6}y^{5/6}K_{5/6}(y\kappa)}{\Gamma(5/6)}, \tag{2.183}$$

where K_ν is the modified Bessel function of the second kind. Individually, both the terms Q_A and Q_B diverge as $\kappa\to 0$. However, by taking the limit of the difference as $\kappa\to 0$, the outcome is a finite result

$$Q\left(y\right)=Q_{0}C_{n}^{2}y^{5/3}, \tag{2.184}$$

where

$$Q_{0}=\frac{36}{25}\frac{2^{1/3}\pi^{3}}{\Gamma(5/6)^{2}}=1.457. \tag{2.185}$$

The result in Eq. (2.184) implies that we have

$$T\left(\mathbf{x},\mathbf{K}_{d},z\right)=T_{0}\left(\mathbf{x},\mathbf{K}_{d}\right)\exp\left[-k_{0}^{2}Q_{0}C_{n}^{2}\int_{0}^{z}\left|\frac{z'}{k_{0}}\mathbf{K}_{d}+\mathbf{x}\right|^{5/3}dz'\right]. \tag{2.186}$$

The z integral is difficult, it is therefore evaluated by way of approximation. That is, we make the so-called quadratic approximation [85] by using, instead of the exponent 5/3, the exponent 2. This simplifies the term in the absolute value bracket in the following way

$$\begin{aligned} h(\mathbf{x},\mathbf{K}_d,z) &= \int_0^z \left|\frac{z'}{k_0}\mathbf{K}_d+\mathbf{x}\right|^2 dz' \\ &= z|\mathbf{x}|^2+z^2\mathbf{x}\cdot\frac{\mathbf{K}_d}{k_0}+\frac{1}{3}z^3\left|\frac{\mathbf{K}_d}{k_0}\right|^2. \end{aligned} \tag{2.187}$$

In making the quadratic approximation, we introduce an imbalance of dimensions in the exponential, therefore to correct for this we introduce a parameter, d, which has units of length. This parameter, whilst it is introduced operationally, will always represent the beam radius. Now, we can rewrite Eq. (2.186) as follows

$$T(\mathbf{x},\mathbf{K}_d,z) = T_0(\mathbf{x},\mathbf{K}_d)\exp\left[\frac{-4\mathcal{K}Q_0\lambda h(\mathbf{x},\mathbf{K}_d,z)}{\pi d^4}\right], \tag{2.188}$$

where

$$\mathcal{K} = \frac{\pi^3 C_n^2 d^{11/3}}{\lambda^3}, \tag{2.189}$$

is the normalised turbulence strength.

The density matrix is obtainable from the above results by working backwards. As a first step, we take the Fourier transform of Eq. (2.188) this leads to

$$\begin{aligned} \mathcal{H}(\mathbf{K}_s,\mathbf{K}_d,z) &= \int \mathcal{H}_0(\mathbf{K}_s-\mathbf{K},\mathbf{K}_d)\,\mathcal{F}_{\mathbf{x}}\left\{\exp\left[\frac{-4\mathcal{K}Q_0\lambda h(\mathbf{x},\mathbf{K}_d,z)}{\pi d^4}\right]\right\} \\ &\quad\times\frac{d^2K}{(2\pi)^2}, \end{aligned} \tag{2.190}$$

where $\mathcal{F}_{\mathbf{x}}$ denotes the Fourier transform with respect to the $\mathbf{x}$ co-ordinate. As a final step, we have to multiply by an exponential as required by the ansatz in Eq. (2.167). The Fourier transform is given as

$$\begin{aligned} \mathcal{F}_{\mathbf{x}}\{\cdot\} &= \frac{\pi d^2}{4\mathcal{K}Q_0 t}\exp\left\{-\frac{\mathcal{K}Q_0 d^2 t^3}{12}|\mathbf{K}_1-\mathbf{K}_2|^2-\frac{\mathrm{i}d^2 t}{4}(\mathbf{K}_1-\mathbf{K}_2)\cdot\mathbf{K}\right. \\ &\quad\left.-\frac{d^2}{16\mathcal{K}Q_0 t}|\mathbf{K}|^2\right\}, \end{aligned} \tag{2.191}$$

where

$$t = \frac{z\lambda}{\pi d^2}. \tag{2.192}$$

The final expression for the solution of the IPE becomes

$$\begin{aligned}\rho\left(\mathbf{K}_1,\mathbf{K}_2,t\right) &= \frac{\pi d^2}{4\mathcal{K}Q_0 t}\int \rho_0\left(\mathbf{K}_1-\mathbf{K},\mathbf{K}_2-\mathbf{K}\right)\exp\left\{-\frac{\mathcal{K}Q_0 d^2 t^3}{12}\left|\mathbf{K}_1-\mathbf{K}_2\right|^2\right. \\ &\quad \left.+\frac{\mathrm{i}d^2 t}{4}\left(\left|\mathbf{K}_1\right|^2-\left|\mathbf{K}_2\right|^2\right)-\frac{\mathrm{i}d^2 t}{4}\left(\mathbf{K}_1-\mathbf{K}_2\right)\cdot\mathbf{K}-\frac{d^2}{16\mathcal{K}Q_0 t}\left|\mathbf{K}\right|^2\right\} \\ &\quad \times\frac{d^2 K}{(2\pi)^2}. \end{aligned} \tag{2.193}$$

The solution of the IPE as given above represents a single photon state that has been propagated through atmospheric turbulence. Save for some discrepancies which may arise due to the quadratic structure function approximation, the solution given above should be able to hold in all turbulence conditions. The reason for this universal applicability is because it has been derived according to the multiphase screen approach, which means that it is able to reliably represent both weak and strong scintillation conditions.

2.7 Compressive sensing

In conventional compression techniques, the signal is acquired first and stored, only at a later stage is it compressed. However, in compressive sensing, this procedure is reversed. The signal is first compressed and then stored. The compression takes place during the measurement process.

2.7.1 The problem

Let us consider a signal $f \in R^N$ which is expressible in some orthonormal basis A_i, where $i = 1...N$, as follows

$$f = \sum_{i=1}^{N} x_i A_i, \tag{2.194}$$

where x_i are the coefficients of the signal in the said basis. In matrix notation, we can rewrite the signal f as follows

$$f = Ax, \tag{2.195}$$

where x is the vector of coefficients and A a matrix of the basis elements.

Compressive sensing concerns itself with the recovery of an S-sparse N-dimensional signal from $m << N$ measurements. That is, from a significantly smaller number of measurements. A signal is said to be S-sparse if it has S non-zero entries.

In mathematical form, the problem that compressive sensing solves is given as follows:

Can we recover the signal f given a set of undersampled data

$$y = Bf? \tag{2.196}$$

where B is an $m \times N$ matrix called the sensing/measurement matrix.

It turns out, the answer to this question is yes. The signal can be recovered using the ℓ_1-norm

$$\min\|x_s\|_{\ell_1} \text{ such that } Bx_s = y, \tag{2.197}$$

where x_s is the solution of the optimization. It is important to note that in order for compressive sensing to be successful there are certain conditions that have to be satisfied.

2.7.2 Restricted isometry property

The success of the compressive sensing method depends on the sensing matrix. It is important to choose a sensing matrix such that it is possible, from the set of observed results, to recover the original full signal. For an $S-$sparse signal, the sensing matrix satisfies the so-called restricted isometry property (RIP) if

$$(1-\delta_S)\|x\|^2_{\ell_2} \leq \|Bx\|^2_{\ell_2} \leq (1+\delta_S)\|x\|^2_{\ell_2}, \tag{2.198}$$

for all signals with sparsity upto S for some isometry constant δ_S, where $\|\cdot\|$ is the Euclidean norm. The RIP property essentially requires that the sensing matrix be nearly orthonormal. When the RIP property holds, it means that the sensing matrix preserves the Euclidean-length of the $S-$sparse signals. This, in turn, means that the $S-$sparse signals are not in the null space of the sensing matrix, B. This is quite important since, if the signals were in the null space, it would be impossible to recover them.

2.7.3 Incoherence

Another important concept in compressive sensing is the coherence between the representation basis A and the sensing basis B. Coherence in compressive sensing language pertains to the largest correlation between any two elements of the two bases A and B. It is expressed mathematically as

$$\mu(A,B) = \sqrt{N}\cdot\max|\langle A_i, B_j\rangle| \text{ for } 1 \leq i,j \leq N, \tag{2.199}$$

where $\langle \#, * \rangle$ denotes an inner product. In the above definition it follows that $\mu(A,B) \in [1,\sqrt{N}]$.

Compressive sensing works best with incoherent pairs. This is why standard compressive sensing techniques are based on random matrices, as they are largely incoherent with fixed bases.

2.8 Summary

In this chapter we have introduced and discussed the main ideas that will be used in this thesis. We started from Maxwell's equations and in conjunction with the monochromatic condition established the Helmholtz equation. As a next step, we introduced the Poynting vector which is used to describe the flow of energy in an optical field. The Poynting vector was used to define the linear momentum density of an optical. The former was further used to define the angular momentum density. From the angular momentum density, we then proceeded to derive the total angular momentum of an optical field. Upon introducing the total angular it is noted that the separation into a spin and an orbital component is not, in general, well defined for arbitrary fields. Nonetheless, this difficulty is removed when we consider paraxial optical fields. The paraxial optical field is obtained as a solution to the paraxial equation, which is obtained as an approximation to the Helmholtz equation.

Of particular interest for the work in this thesis are paraxial optical fields that carry OAM. The LG modes are considered for our study and a method of how to generate them was discussed.

A discussion on quantum states, quantum entanglement, quantum tomography, and the spontaneous parametric downconversion process was also given.

Atmospheric turbulence was also discussed; we discussed scintillation, introduced the Kolmogorov spectral density and also discussed some common models for the evolution of optical fields in atmospheric turbulence. These are the SPS and MPS based models. The SPS model is based on the work done by Paterson [71] and the MPS model is called the IPE [90].

Lastly, we gave a very brief discussion of compressive sensing.

In the following chapters, we present the results of the work done for this thesis and also finish off with the conclusions.

Chapter 3

Orbital angular momentum under strong scintillation

3.1 Introduction

Numerical simulations have become ubiquitous in research due to their ability to establish results which would otherwise be difficult to evaluate theoretically and-or setup experimentally. They have, in particular, been used extensively in the studies of propagation in random media [125, 126, 127, 128]. This has been done in the context of wave propagation in the ocean, propagation through the ionosphere and also wave propagation in the atmosphere. The latter is the main focus of this work. In the previous chapter, it was discussed in detail how turbulence affects the index of refraction of the atmosphere. The random variation of the index of refraction causes an optical field to be randomly distorted as it propagates through the atmosphere.

The effect of atmospheric turbulence on OAM carrying optical fields has been a subject of many studies [71, 72, 73, 74, 75, 76, 77, 78, 79, 80, 81, 82]. However, most of these studies have been based on the single-phase screen (SPS) model [71]. The single phase screen model is based on the notion that the only effect of the index of refraction fluctuation on the optical field is a mere phase perturbation. It has recently been shown that this is not always the case, especially in strong scintillation [86]. In strong scintillation, the best method to represent the effect of the atmospheric turbulence on OAM carrying optical fields is the multi-phase screen (MPS) approach. Using such an approach, the effects of the variation in the amplitude of the optical field become represented. An analytical model that is based on the MPS approach has been recently employed to formulate the evolution of the photonic quantum states propagating through atmospheric turbulence. The formulation is based on an infinitesimal propagation equation (IPE) [82, 90, 91] and has also been discussed in detail in Chapter 2. The IPE is valid in both weak and strong scintillation conditions since it is based on the MPS approach. Although the IPE was proposed in the context of entangled photonic quantum states, we show here that it also holds for single photonic states. Therefore, it could also be applied to classical fields.

In this chapter, we study the evolution of optical fields under arbitrary scintillation conditions. For this purpose, we consider an input optical field with an amplitude profile given by a certain OAM mode — an LG mode with azimuthal index $\ell = 1$ and radial index $p = 0$. Then we investigate the effect of the scintillation on this mode by computing the overlap between the distorted LG mode and different LG modes to determine the fraction of optical power in the different modes. Both the IPE approach and the SPS approach are used to predict these power fractions as a function of propagation distance. We then compare these predictions against numerical simulations.

There are several numerical and experimental studies that tested the SPS model [73, 72, 77, 78, 79], none so far have provided either experimental or numerical testing of the IPE. Here we use MPS numerical simulations that are based on the Kolmogorov theory of turbulence to determine whether the IPE predictions are more reliable than the SPS predictions. We find that the numerical results agree well with the IPE predictions under all scintillation conditions. Since the IPE predictions deviate from the SPS predictions under strong scintillation conditions, the numerical results show that the IPE predictions are favored over those of the SPS approach.

The work presented in this chapter has been published [129].

This chapter is organized as follows: Section 3.2 is based on the MPS algorithm that is used for the numerical simulations. It is broken down into subsections, the first subsection discusses the part of the algorithm that is responsible for the refractive properties of the atmosphere, and the second subsection describes the part of the algorithm that pertains to the propagation of the optical field in the atmosphere. Section 3.3 discusses the theoretical framework against which we are to compare the results of the numerical simulation of Sec. 3.2. Here, we discuss the power fractions as given by both the SPS and the IPE models. The comparison to numerical simulations is presented in Sec. 3.4. Finally, we finish the chapter with some conclusions in Sec. 3.5.

3.2 Multi-phase screen

Let us begin by rewriting the stochastic parabolic equation [87, 88, 130]

$$\mathrm{i}\partial_z f(\mathbf{r}) = -\frac{1}{2k_0}\nabla_\perp^2 f(\mathbf{r}) + k_0\delta n(\mathbf{r}) f(\mathbf{r}) \tag{3.1}$$

where $k_0 = \frac{2\pi}{\lambda}$ is the wave number in vacuum, $\delta n(\mathbf{r})$ represents the fluctuations due to the atmospheric turbulence, and $\nabla_\perp^2 = \partial_x^2 + \partial_y^2$ is the transverse Laplacian operator. Equation (3.1) holds under the condition that the wavelength λ of the optical field is very small compared to scale size of the medium, and that the atmospheric turbulence scatters the optical field only weakly.

In dealing with turbulence over some distance z, we can divide the propagation distance into a series of slices such that each slice represents a weakly scattering medium. The condition for weak scattering ensures that the only effect of the atmospheric turbulence on the optical field is a phase perturbation. The effect of atmospheric turbulence on the amplitude of the optical field is introduced by diffraction as the optical field propagates through the series of slices. Within this approach, we can solve the problem of the propagation of an optical field through turbulence by dividing the propagation into a series of slices separated by a distance Δz as in Fig. 3.1 [131, 132, 133]. The slices are statistically independent, and each one represents a random phase screen. The statistical independence of the phase screens is the equivalent of the Markov approximation that is used in the analytical calculations, see for instance the

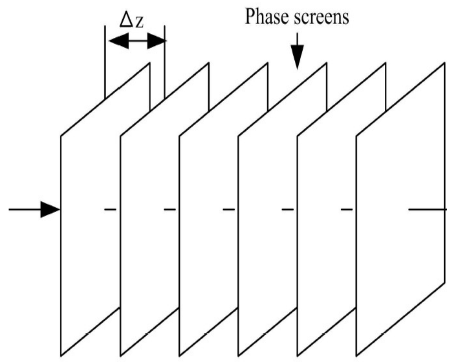

FIGURE 3.1: Schematic illustration of the approach used to perform a numerical simulation of the propagation of an optical field in atmospheric turbulence.

discussion in Chapter 2 on the IPE. The algorithm for the generation of the phase screens is discussed next.

3.2.1 Phase screen generation

The phase screen that is used to represent the random phase perturbation at each slice during the numerical simulation of the propagation of the optical field in turbulence is generated by transforming a 2D array of complex numbers that have zero mean and unit variance into an array that has the same statistics as the atmospheric turbulence. This process is often referred to as filtering white Gaussian noise, and is mathematically given by [87, 130]

$$\theta_1 + \mathrm{i}\theta_2 = \left(2\pi k_0^2 \Delta z\right)^{1/2} \mathcal{F}^{-1}\left\{\chi(\mathbf{K})\left[\frac{\Phi_n(\mathbf{K})}{\Delta_k^2}\right]^{1/2}\right\}, \tag{3.2}$$

where Δz is the distance between two phase screens, $\mathcal{F}^{-1}$ is the inverse transverse Fourier transform, $\Phi_0(\mathbf{K})$ is the index of refraction Kolmogorov power spectral density, $\chi(\mathbf{K})$ is a normally distributed complex random function, that has zero mean and is δ-correlated

$$\langle \chi(\mathbf{K}_1)\chi^*(\mathbf{K}_2)\rangle = (2\pi\Delta_k)^2\, \delta(\mathbf{K}_1 - \mathbf{K}_2), \tag{3.3}$$

Δ_k is a correlation length of the random function in the spatial frequency domain that is introduced for dimensional analysis reasons, the angled brackets $\langle\cdot\rangle$ denote an ensemble average, and $\mathbf{K} = (k_x, k_y)$ is the transverse propagation wave vector. A phase screen that is generated by taking the real part of Eq. (3.2) is shown in Fig. 3.2.

The digital implementation of Eq. (3.2) introduces a limit to the spatial frequencies and thus the spatial scales that can be represented in the numerical simulation. This effect, due to sampling, filters the contribution from certain harmonics that would otherwise be present in real turbulence. Since the smallest spatial frequency is bounded by the sampling unit in the Fourier domain, it follows that the Kolmogorov power spectral density is not properly sampled at the

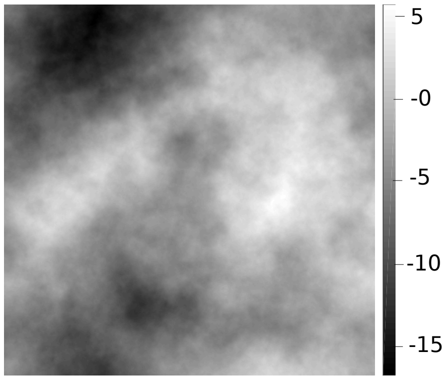

FIGURE 3.2: A typical turbulence random phase screen. This image was generated with 2^{10} in each direction.

lowest spatial frequencies. Since the Kolmogorov power spectral density is a delta-like function that peaks at the origin, a thorough analysis shows that the biggest contribution comes from the low spatial frequencies. The crucial frequency components that are excluded by the sampling process are in the range $(-\Delta_{kx}/2, \Delta_{kx}/2)$ and $(-\Delta_{ky}/2, \Delta_{ky}/2)$.

One, and probably the most intuitive, way to increase the accuracy of the phase screens is to increase the number of points that are used to perform the sampling of the Kolmogorov power density (by decreasing the length of the sampling unit), this method would reduce the intervals $(-\Delta_{kx}/2, \Delta_{kx}/2)$ and $(-\Delta_{ky}/2, \Delta_{ky}/2)$ substantially and thus foster the inclusion of the crucial lower frequency components. However, this would also lead to a higher computational cost with regards to time and memory. Thus to mitigate the issue of improper sampling, we will instead use a method that was developed by Lane et al. [134]. This method is known as the method of sub-harmonics, and it works by including an additional phase to the one generated using the FFT method (Eq. (3.2)) according to the algorithm

$$\begin{aligned} \theta_{SH}(j\Delta x, l\Delta y) &= \sum_{n=1}^{N_p}\sum_{p=-1}^{1}\sum_{q=-1}^{1}[a(p,q,n)+\mathrm{i}b(p,q,n)] \\ &\quad\times\exp\left[2\pi\mathrm{i}\left(\frac{jp}{3^n N_x}+\frac{lq}{3^n N_y}\right)\right], \end{aligned} \tag{3.4}$$

such that the variance of the randomly generated a and b is given as

$$\langle a^2(p,q,n)\rangle = \langle a^2(p,q,n)\rangle = 2\pi k_0^2 \Delta z \Delta p_n \Delta q_n \Phi_\theta(p\Delta p_n, q\Delta q_n), \tag{3.5}$$

where, $\Delta p_n = \Delta p/3^n$ and $\Delta q_n = \Delta q/3^n$.

The method of sub-harmonics works by sampling the interval that is not covered by the FFT method in Eq. (3.2). This additional sampling is done within a single cell of the bigger mesh. That is, rather than re-sampling the entire Fourier domain, we replace the sample at the origin with a new mesh in such a way that the new mesh still corresponds to a single cell in the overall Fourier domain. This means that rather than representing the value of the Kolmogorov spectral density with a single point at the origin, we represent it with more points since it is changing very rapidly in this region, and thus a single point cannot represent it accurately. As an aid to understanding the method of sub-harmonics we show in Fig. 3.3 how the method

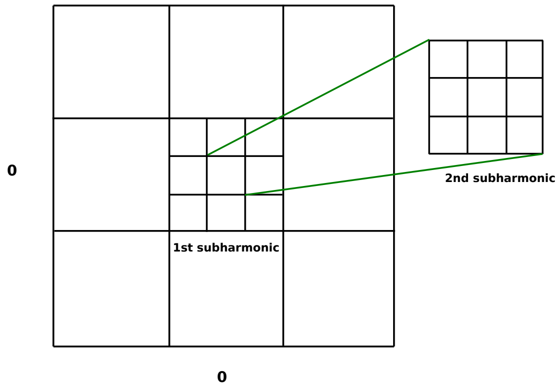

FIGURE 3.3: An illustration of the method of sub-harmonics.

works. The first sub-harmonic is generated by replacing the $(0,0)$ point by 9 points, that is, we reduce the size of the $(0,0)$ and add 8 additional points around it. The second sub-harmonic is generated in the same way, as shown in Fig. 3.3. The addition of higher sub-harmonics is also done in the same way.

3.2.2 Propagation

As already mentioned, the effect of the phase screen is only contained in the phase of the optical field. However, depending on the conditions of the atmosphere, the turbulence can also induce some amplitude variations in the optical field. These amplitude variations accumulate with propagation. This implies that the propagation process, over several phase screens, converts the phase perturbations into amplitude effects. Therefore, the next part of the simulation algorithm involves the propagation of the optical field. This is done by solving the paraxial equation given in Eq. (3.1), as if there is no turbulence, for free-space propagation in a vacuum. This condition can easily be met by setting the fluctuations of the index of refraction to $\delta n = 0$. The optical fields that is used in the propagation process contains the effects of the phase perturbation. The equation that has to be solved is the standard paraxial equation

$$\frac{\partial f(\mathbf{r})}{\partial z} = \frac{\mathrm{i}}{2k_0}\nabla_{\perp}^2 f(\mathbf{r}). \tag{3.6}$$

There are a number of ways to solve Eq. (3.6), however, here will we solve it in the Fourier domain as it makes it easy to remove the transverse derivatives. We rewrite Eq. (3.6) in the Fourier domain

$$\frac{\partial F(\mathbf{K},z)}{\partial z} = \frac{\mathrm{i}|\mathbf{K}|^2}{2k_0}F(\mathbf{K},z), \tag{3.7}$$

where $F(\mathbf{K},z)$ is the two-dimensional transverse Fourier transform of $f(\mathbf{r})$.

In the above form, we have a standard one-dimensional partial differential equation which has the simple solution given as

$$F(\mathbf{K},z) = F(\mathbf{K},z_0)\exp\left(\frac{\mathrm{i}|\mathbf{K}|^2\Delta z}{2k_0}\right), \tag{3.8}$$

where $z = z_0 + \Delta z$.

With regards to the propagation in atmospheric turbulence, we thus employ the following procedure: We first modulate the input function $f_{\text{in}}(\mathbf{r})$ with the phase function that represents the phase screen

$$f_{\text{out}}(\mathbf{r}) = f_{\text{in}}(\mathbf{r}) \exp\left[\mathrm{i}\theta(\mathbf{R})\right], \tag{3.9}$$

where $\theta(\mathbf{R})$ is the phase screen function that is generated using Eq. (3.2) and Eq. (3.5). The propagation is performed by first taking $f_{\text{out}}(\mathbf{r})$ into the Fourier domain and multiplying it by the function as described in Eq. (3.8), the propagation process is completed by taking the inverse Fourier transform.

This process is repeated over all the phase screens until the full propagation distance has been covered.

3.3 Power fraction calculation

In Chapter 2 we derived the infinitesimal propagation equation (IPE) for a single photon optical field and we found that it is given as

$$\begin{aligned} \partial_z \rho(\mathbf{K}_1, \mathbf{K}_2, z) &= \frac{\mathrm{i}}{2k_0}\left(|\mathbf{K}_2|^2 - |\mathbf{K}_1|^2\right)\rho(\mathbf{K}_1, \mathbf{K}_2, z) \qquad (3.10)\\ &+k_0^2 \int \Phi(\mathbf{q})\left[\rho(\mathbf{K}_1 - \mathbf{q}, \mathbf{K}_2 - \mathbf{q}, z)\right.\\ &\left.-\,\rho(\mathbf{K}_1, \mathbf{K}_2, z)\right] d^2q \qquad (3.11)\end{aligned}$$

where $\Phi_0(\mathbf{q}) = \Phi(2\pi\mathbf{q}, 0)$.

The solution to the above differential equation was obtained by using the quadratic structure approximation, and is rewritten here for convenience

$$\begin{aligned} \rho(\mathbf{a}_1, \mathbf{a}_2, t) &= \frac{\pi w_0^2}{4Q_0\mathcal{K}t}\int \rho_0(\mathbf{a}_1 - \mathbf{b}, \mathbf{a}_2 - \mathbf{b}) \exp\left\{-\pi^2 w_0^2\left[\frac{\mathcal{K}Q_0t^3}{3}|\mathbf{a}_1 - \mathbf{a}_2|^2\right.\right.\\ &\left.\left.-\mathrm{i}t\left(|\mathbf{a}_1|^2 - |\mathbf{a}_2|^2\right) + \frac{|\mathbf{b}|^2}{4\mathcal{K}Q_0t} - \mathrm{i}t\mathbf{b}(\mathbf{a}_1 - \mathbf{a}_2)\cdot\mathbf{b}\right]\right\} d^2b, \end{aligned} \tag{3.12}$$

where

$$\mathbf{a} = \frac{\mathbf{K}}{2\pi}, \tag{3.13}$$

is the spatial frequency vector

$$\mathcal{K} = \frac{\pi^3 C_n^2 w_0^{11/3}}{\lambda^3}, \tag{3.14}$$

is the normalised turbulence strength

$$t = \frac{z\lambda}{\pi w_0^2}, \tag{3.15}$$

is the normalized propagation distance, w_0 is the Gaussian beam waist, with $Q_0 = 1.457$ is a multiplicative constant, for details see Chapter 2.

3.3.1 Generating function

The solution of the IPE as given by Eq. (3.12) allows for an input state that can be specified by the matrix elements $\rho_0(\mathbf{a}_1, \mathbf{a}_2)$, which can be further expressed in terms of Laguerre-Gaussian (LG) modes. Rather than using the generic expression for the LG (angular spectra) modes, we instead present the generating function for the angular spectra of LG modes with the radial index $p = 0$ [90]

$$\mathcal{G}_{\pm}(\mathbf{a}, t; \mu) = \exp[\mathrm{i}\pi w_0 (a_x \pm a_y)\mu - \pi(a_x^2 + a_y^2)(1 - \mathrm{i}t)], \tag{3.16}$$

where μ is the azimuthal generating parameter for a particular LG mode, and $\mathbf{a} = (a_x, a_y)$. Given the above generating function, an arbitrary spectrum of the LG modes for the radial index $p = 0$ can be obtained according to the following operation

$$\Phi_0^{\ell}(\mathbf{a}) = \mathcal{N}\left(\frac{\partial^{|\ell|}}{\partial\mu}\mathcal{G}_{\mu=0}\right), \tag{3.17}$$

where

$$\mathcal{N} = w_0\left(\frac{2^{|\ell|+1}\pi}{|\ell|!}\right)^{1/2} \tag{3.18}$$

is a normalization constant.

The input state density matrix elements in the solution of the IPE in Eq. (3.12) can be expressed in terms of the generating function as follows

$$\rho_0(\mathbf{a}_1, \mathbf{a}_2, 0) = \mathcal{G}_{\pm}(\mathbf{a}_1, 0; \mu_1)\,\mathcal{G}_{\pm}^{*}(\mathbf{a}_2, 0; \mu_2), \tag{3.19}$$

where μ_n is a generating parameter for the azimuthal indices and $n = 1, 2$.

3.3.2 Overlap calculation

The expression in Eq. (3.19) can be substituted into the solution of the IPE, whereafter the integration over $\mathbf{b}$ is performed to obtain a final expression in terms of the generating parameters for the input state. The latter result for the case of an input LG mode with azimuthal index $\ell = 1$ is shown below

$$\begin{aligned}\rho(\mathbf{a}_1, \mathbf{a}_2, t) &= \frac{\pi^4 w_0^4}{A_1^3}\left[A_2|\mathbf{a}_1|^2 + A_2^{*}|\mathbf{a}_2|^2 + A_3\mathbf{a}_1\cdot\mathbf{a}_2 + \mathrm{i}A_1(\mathbf{a}_2\times\mathbf{a}_1)\cdot\hat{z} + A_6\right] \\ &\quad\times\exp\left[-\frac{\pi^2 w_0^2}{3A_1}\left(A_4|\mathbf{a}_1|^2 - A_5\mathbf{a}_1\cdot\mathbf{a}_2 + A_4^{*}|\mathbf{a}_2|^2\right)\right]\end{aligned} \tag{3.20}$$

where

$$
\begin{aligned}
A_1 &= 8Yt + 1, \\
A_2 &= 2\mathrm{i}Yt^2 - 4Yt - 4Y^2t^4 - 16Y^2t^2, \\
A_3 &= 8Y^2t^4 + 32Y^2t^2 + 8Yt + 1, \\
A_4 &= 8Y^2t^4 - 12\mathrm{i}Yt^2 + 4Yt^3 + 12Yt - 3\mathrm{i}t + 3, \\
A_5 &= 16Y^2t^4 + 8Yt^3 + 24Yt, \\
A_6 &= \frac{32Y^2t^2 + 4Yt}{\pi^2 w_0^2},
\end{aligned}
$$

and

$$Y = Q_0\mathcal{K}. \tag{3.21}$$

Equation (3.20) represents the state of the input optical field after propagation through atmospheric turbulence.

As is well known, the propagation of an OAM carrying optical field through atmospheric turbulence leads to the population of OAM modes which were initially empty in the input state. This population of adjacent modes is called crosstalk. Using the expression in Eq. (3.20) we can be able to quantify the crosstalk (to other modes) for an optical field with input OAM $\ell = 1$ propagating through a turbulent atmosphere.

The crosstalk calculation is done by evaluating the overlap between the output density matrix given in Eq. (3.20) and the generating function for the LG modes in Eq. (3.16). The overlap calculation is an integral calculation given as follows

$$\eta = \int \rho\left(\mathbf{a}_1, \mathbf{a}_2, z\right) \mathcal{G}_{\pm}^{*}\left(\mathbf{a}_1, \mathbf{a}_2; \mu_3\right) \mathcal{G}_{\pm}\left(\mathbf{a}_1, \mathbf{a}_2; \mu_4\right) d^2a_1 d^2a_2. \tag{3.22}$$

The final result is a generating function for the crosstalk coefficients. In order to obtain the crosstalk into other LG modes, one has to apply the procedure outlined in Eq. (3.17). In this particular instance, we would have to apply the procedure four times since there is a total of four generating parameters represented in the above equation for the overlap calculation.

To avoid confusion, we will from now on refer to the crosstalk interchangeably with power fraction in a certain mode, where the power fraction is the power in the mode normalized to the input mode power. This prevents a huge confusion that would result when we are interested in calculations relating to the same azimuthal index as the input state. As a case in point, let us consider the power fraction retained in the input mode with azimuthal index $\ell = 1$

$$
\begin{aligned}
\mathcal{P}_{1\to 1}^{IPE} = {} & \frac{1}{\Gamma^3}\Big[27(8X^2+4X+1)Y^4 + 36X^3(2X+1)^2Y^2 \\
& +24X^6(2X^2+2X+1)\Big]\, Y^2
\end{aligned} \tag{3.23}
$$

where

$$\Gamma = 4X^4 + 4X^3 + 12XY^2 + 3Y^2, \tag{3.24}$$

$$X = 0.59 Q_0 W^{5/3}, \tag{3.25}$$

and

$$W = \frac{w_0}{r_0}. \tag{3.26}$$

The subscript $1 \to 1$ denotes that the input mode has azimuthal index $\ell = 1$ and the overlap mode has azimuthal index $\ell = 1$. The generic expression is given as $\mathcal{P}_{m \to n}$, where m denotes the input mode and n the overlap mode. Below, we show the power fractions for $n = 2, 3, 5$

$$\begin{aligned}
\mathcal{P}_{1\to2}^{IPE} &= \frac{12X\Lambda}{\Gamma^4}\left[9(6X^2+4X+1)Y^4 + 12X^3(X+1)(2X+1)Y^2 + 2X^6(4X^2+4X+3)\right] Y^2, \\
\mathcal{P}_{1\to3}^{IPE} &= \frac{12X^2\Lambda^2}{\Gamma^5}\left[(144X^2+108X+27)Y^4 + 12X^3(2X+3)(2X+1)Y^2 \right. \\
&\quad \left. + 16X^6(X^2+X+1)\right] Y^2, \\
\mathcal{P}_{1\to5}^{IPE} &= \frac{48X^4\Lambda^4}{\Gamma^7}\left[(216X^2+180X+45)Y^4 + 12X^3(2X+5)(2X+1)Y^2 \right. \\
&\quad \left. + 8X^6(2X^2+2X+3)\right] Y^2
\end{aligned}$$

where

$$\Lambda = 2X^3 + X^2 + 3Y^2. \tag{3.27}$$

Weak scintillation

Scintillation strength is characterized by the Rytov variance which can be expressed in terms of the dimensionless parameters t and $\mathcal{K}$ as

$$\sigma_R^2 = 2.76\mathcal{K}t^{11/6}, \tag{3.28}$$

or in terms of the dimensionless parameters W and $\mathcal{K}$ as

$$\sigma_R^2 = 1.055\frac{W^{55/18}}{\mathcal{K}^{5/6}}. \tag{3.29}$$

The SPS model holds in weak scintillation and thus can be obtained from the IPE expressions above by taking the limit as $\mathcal{K} \to \infty$. Under this condition, the power fraction expressions that have been calculated above for the IPE reduce to the expressions

$$\begin{aligned}
\mathcal{P}_{1\to1}^{\mathrm{SPS}} &= \frac{8X^2+4X+1}{(4X+1)^3} \\
\mathcal{P}_{1\to2}^{\mathrm{SPS}} &= \frac{24X^3+16X^2+4X}{(4X+1)^4} \\
\mathcal{P}_{1\to3}^{\mathrm{SPS}} &= \frac{4X^2(16X^2+12X+3)}{(4X+1)^5} \\
\mathcal{P}_{1\to5}^{\mathrm{SPS}} &= \frac{16X^4(24X^2+20X+5)}{(4X+1)^7}
\end{aligned} \tag{3.30}$$

The SPS expressions as given above only depend on the parameter W through X, whereas the IPE expressions depend on two parameters, W and $\mathcal{K}$ through X and Y. This has interesting consequences for the behavior of optical fields in turbulence. This implies that while the behavior in weak scintillation can be described by a single dimensionless parameter W, we need two dimensionless parameters to accurately describe the behavior of OAM carrying optical fields in strong scintillation conditions. The comparison of the SPS and IPE as a function of the parameter W will be given together with the numerical results later. In the next part, we will start our discussion by focusing on the relationship between the power fractions and normalized propagation distance t for both the SPS and the IPE models.

3.3.3 Analysis of weak and strong scintillation

In this section, we compare the SPS and the IPE prediction by plotting the power fractions from each model against the normalized propagation distance t. Figure 3.4 shows the power fraction curves as a function of normalized propagation distance. In the figure, four different graphs are shown each containing the power fraction of the output modes with azimuthal indices $\ell = 1, 2, 3$ given that the input mode had azimuthal index $\ell = 1$. The four graphs correspond to four different normalized turbulence strengths $\mathcal{K} = 10, 1, 0.1$ and 0.01. Furthermore, each graph has an additional curve (represented by the gray dashed line with a positive slope) that denotes the Rytov variance as a function of the normalized propagation distance. The magnitude of the Rytov variance is shown by the vertical axis on the right-hand side. All the graphs shown in Fig. 3.4 are log-log plots. The SPS plots in Fig. 3.4 are governed by a single scale parameter which can be determined from the location that corresponds to the maxima of the plots. In the region that corresponds to the slope change, the SPS curves display a power law behavior and are thus scale invariant. An expression for the SPS scale can be obtained by noticing that the transition region is always located close to $W \approx \sqrt{\ell}$. By using the expression for W, the latter equation can be solved for the propagation distance to obtain the SPS scale

$$z_{ws} \approx \frac{0.06\lambda^2 \ell^{5/6}}{w_0^{5/3} C_n^2}. \tag{3.31}$$

This quantity will be called the weak scintillation scale. It corresponds to the scale determined in [86] for the case where the quantum entanglement decays to zero. However, such an observation was based on the fact that all the analyses were done for quantum entanglement within the SPS model. The situation for single photon or classical OAM coupling under strong scintillation is more complicated.

Also in Fig. 3.4 we observe that a change in the normalized turbulence strength $\mathcal{K}$ leads to a horizontal shift of the SPS curves. The SPS curves do not change shape as the value of $\mathcal{K}$ is changed. A shift on the logarithmic axis implies a scaling in the linear axis, that is for different turbulence strengths we have that $t \to \alpha t$, where α is some positive scalar. Therefore, the SPS curves for smaller $\mathcal{K}$ are stretched out over larger propagation distances.

The IPE curves and the SPS curves start out by lying on top of each other, however, for a fixed turbulence strength as the normalized propagation distance increases the two curves start to deviate from each other. The point(normalized propagation distance) at which the two curves start to deviate is a function of turbulence strength. Generally, the IPE curves appear as horizontally squashed relative to the SPS curves in the region beyond the deviation point.

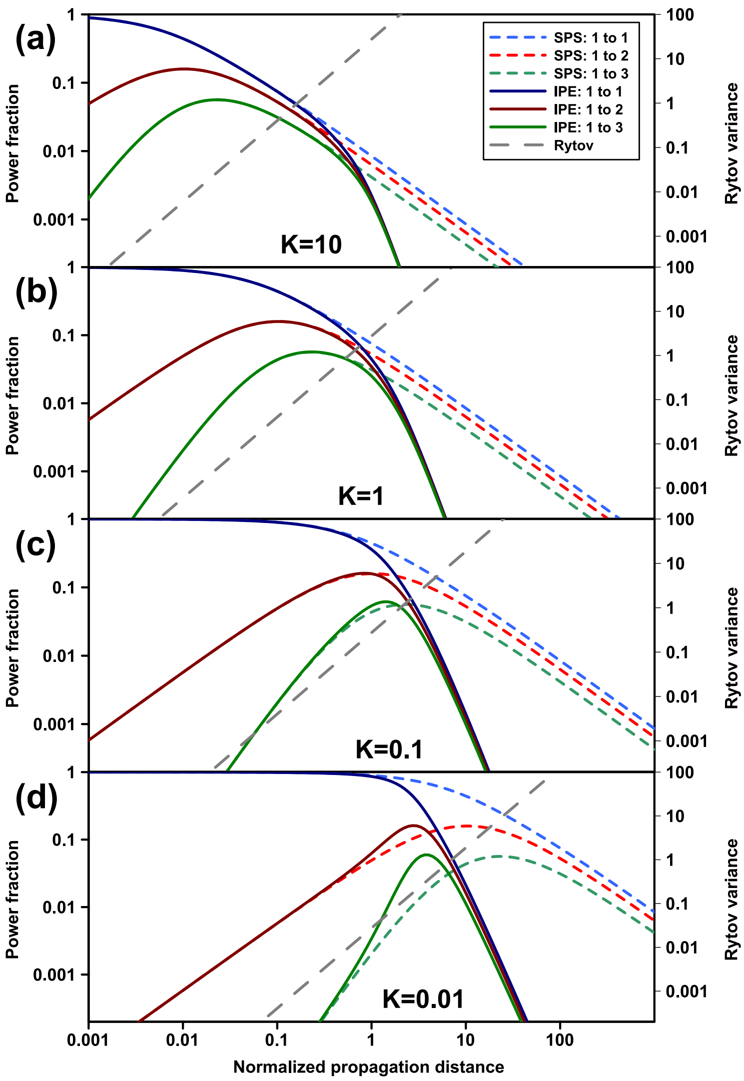

FIGURE 3.4: Comparison of the SPS and IPE models as a function of propagation distance under different turbulent conditions. a) Shows the predictions of the two models for $\mathcal{K} = 10$, b) $\mathcal{K} = 1$, c) $\mathcal{K} = 0.1$ and c) $\mathcal{K} = 0.01$. Included in each of the plots is a line that represents the amount of scintillation (Rytov variance) as a function of normalized propagation distance. 1 to n denotes that the input mode is $\ell = 1$ and n is the scattering mode.

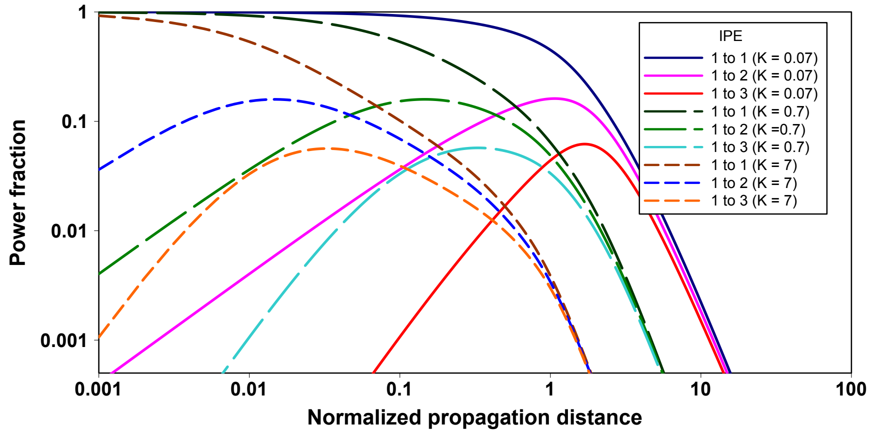

FIGURE 3.5: The power fraction, as predicted by the IPE, in the input OAM mode and its neighboring modes after propagating through turbulence described by three different normalized turbulence strengths. The power fraction is plotted as a function of normalized propagating distance. 1 to n denotes that the input mode is $\ell = 1$ and n is the scattering mode.

The IPE curves much like the SPS curves also have a region that follows a power law, as is depicted by the straight line behavior after reaching a peak. Scaling on the logarithmic axis represents a change in the power of the independent variable $t \to t^{\gamma}$, with $\gamma > 1$. We can see that those regions of the SPS curves that represent power laws correspond to power laws for the IPE curves as well. This implies that the squashing is uniform beyond the transition region. Therefore, γ does not depend on the normalized propagation distance t beyond the transition region. In Fig. 3.5 we further show the behavior of the IPE curves as a function of the normalized turbulence strength. It can be seen that the curves shift towards the right-hand side when the normalized turbulence strength $\mathcal{K}$ is reduced.

The points at which the IPE curves and the SPS curves start to deviate represents a different scale from the weak scintillation scale. This scale will be referred to as the deviation scale. As can be seen from Fig. 3.4, for strong turbulence which is represented by a larger normalized turbulence strength $\mathcal{K}$, the deviation scale is larger than the weak scintillation scale. That is, the deviation scale lies at a larger value of t than the weak scintillation scale. This is in contrast to the weak turbulence case, which is represented by a smaller normalized turbulence strength, where the deviation scale is smaller than the weak scintillation scale. In the latter case, the deviation scale occurs at a shorter normalized propagation distance compared to the weak scintillation scale. The findings that are presented in Fig. 3.4 imply that for weak turbulence the SPS deviates from the IPE curves at an earlier stage compared to the strong turbulence case. This behavior can be seen clearly in the case that curves are plotted as a function of W rather than a function of t, see Fig. 3.6. In the case that the results are plotted as a function W the SPS curves always lie on top of each other irrespective of the value $\mathcal{K}$, while the IPE curves deviate quicker for weak turbulence, that is smaller values of $\mathcal{K}$ the IPE curves deviate at a smaller value of W.

The observations made in this work cast into the question the notion that the deviation of the SPS curve from the IPE curve is an indication of the commencement of strong scintillation. This is because the value of the Rytov variance at which we observe the deviation is not fixed, as

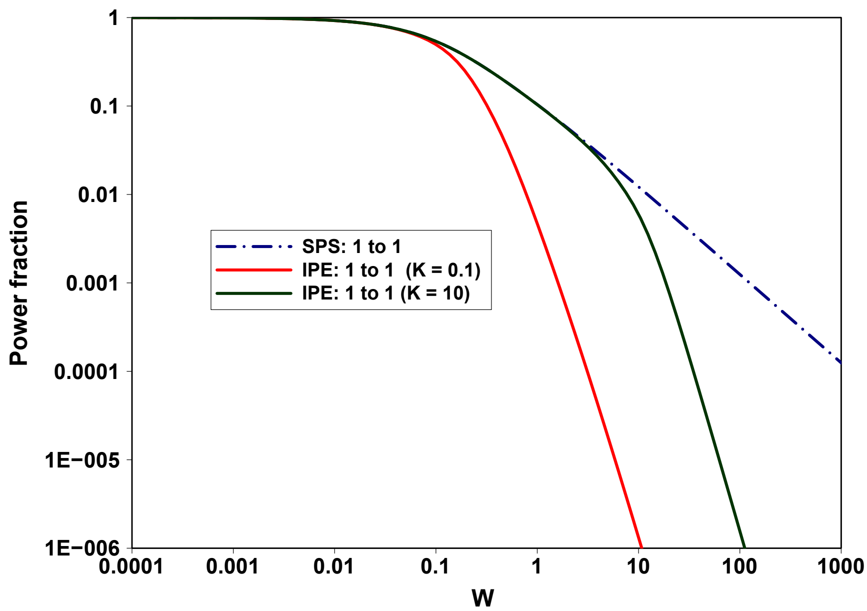

FIGURE 3.6: The power fraction as predicted by the IPE and the SPS as function W for different normalized turbulence strengths.

can be observed from the straight line, in Fig. 3.4, that corresponds to the Rytov variance. The value at which the SPS deviates from the IPE changes with normalized turbulence strength from around unity to about a few orders of magnitude less. Therefore, it is possible that the deviation of the two simply implies the breakdown of the SPS for the given conditions. The nature of the decay scale, for now, remains unanswered and is a matter to be further investigated.

3.4 Numerical Results

The analytical expressions obtained from the IPE and those that correspond to the SPS are compared with numerical simulations to assess their reliability in predicting the behavior of OAM carrying optical fields in atmospheric turbulence. Here, we consider the case of an input LG mode with azimuthal index $\ell = 1$ and radial index $p = 0$ under two different turbulence conditions given by $\mathcal{K} = 0.07$ for weak turbulence and $\mathcal{K} = 0.7$ for strong turbulence. As was the case with the theoretical expressions, we look at the power fractions in the other LG modes due to the crosstalk. Particularly, we consider the power fraction in the output modes specified by the azimuthal indices $\ell = 1, 2, 3$. The power fractions for the turbulence conditions with $\mathcal{K} = 0.07$ are shown in Fig. 3.7, and those that correspond to $\mathcal{K} = 0.7$ are shown in Fig. 3.8. In contrast to the case in the theoretical analysis of the SPS and the IPE given above, all the figures in this discussion are given as a function of the dimensionless parameter W instead of the normalized propagation distance t. In the plots given in Fig. 3.7 and Fig. 3.8, the IPE is represented by the solid lines, the SPS is represented by the dashed lines, and the numerical simulations are represented by the markers with error bars. The numerical simulation results represent the average power fraction, and the error bars represent the standard error, whereby standard error we mean the standard deviation in the mean.

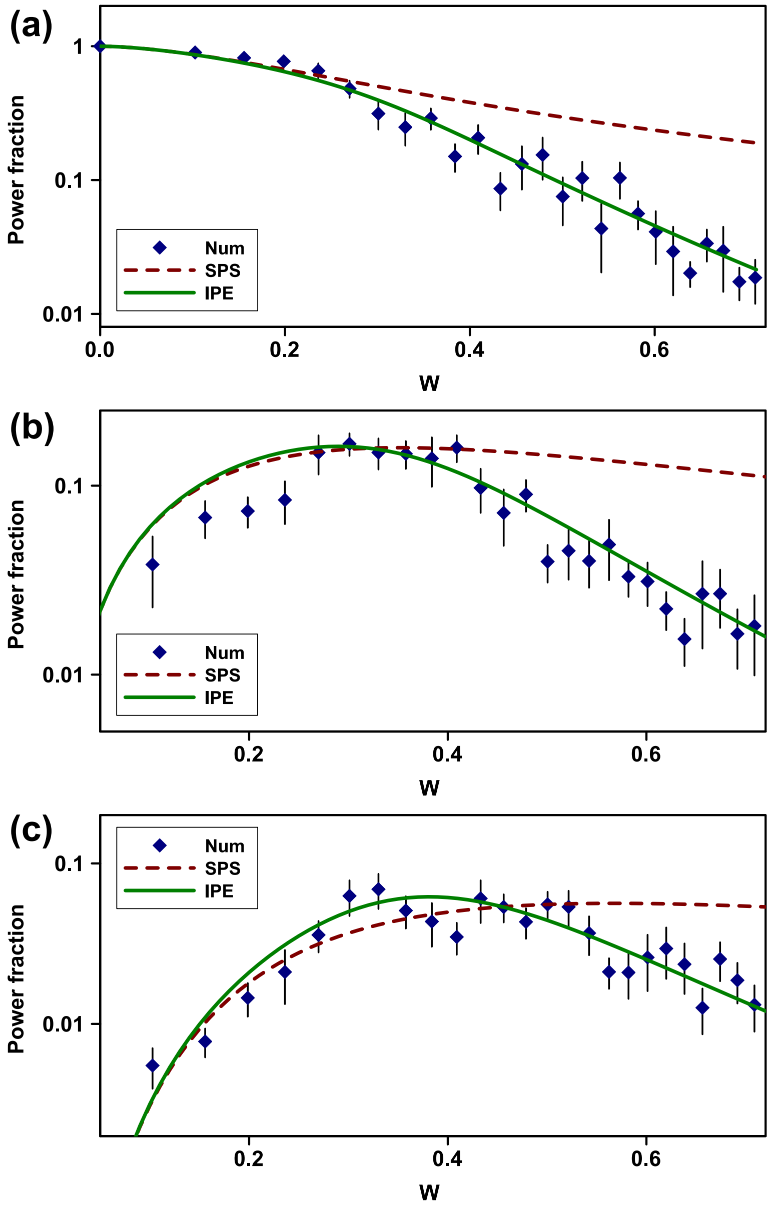

FIGURE 3.7: OAM Content as a function of scintillation strength, for turbulence conditions described by the normalized turbulence strength $K = 0.07$. a) Gives the amount of power in the input mode $\ell = 1$; b) Gives the amount of power in the mode $\ell = 2$; c) Gives the amount of power in the mode $\ell = 3$. The markers are the numerical simulation data, the dashed line is the SPS data, and the solid line is the IPE prediction.

The results have been gathered for different ranges of W so as to capture the regions which show the significant deviation of the IPE and SPS. In both Fig. 3.7 and Fig. 3.8, the IPE is a better fit to the numerical data compared to the SPS model. The first plot in both figures Fig. 3.7(a) and Fig. 3.8(a), shows the power fraction that is retained by the input LG mode as it propagates through the turbulent atmosphere. The second plots, Fig. 3.7(b) and Fig. 3.8(b), show the crosstalk to the LG mode with azimuthal index $\ell = 2$. Finally, the third plots, Fig. 3.7(c) and Fig. 3.8(c) show the crosstalk to the mode with azimuthal index $\ell = 3$. The crosstalk curves show how the power fraction in these higher modes increases from zero as more optical power is transferred from the input LG mode.

In the plots that represent the power fraction retained in the input mode, it can be seen that the two models SPS and IPE agree at the beginning. However, they start to deviate with increasing W. In Fig. 3.7(a) the deviation sets in very early around $W = 0.2$, whereas in Fig. 3.8(a) the deviation sets in at a slightly higher value of W.

In the crosstalk curves, similar behavior is also observed. For instance, initially, the SPS and IPE curves sit on top of each other but start to deviate with increasing values of W. Moreover, for weak turbulence in Fig. 3.7(b) and Fig. 3.7(c) it is observed that the deviation sets in early, even before the curves reach their peaks. The IPE curves first startup above the SPS curves and thus cross the SPS curves to further drop below them due to the accelerated decay. This is in contrast to the case of strong turbulence as depicted in Fig. 3.8(b) and Fig. 3.8(c). In strong turbulence, the deviation only occurs after the SPS curves reach their respective peaks. At this point, the optical power is lost to other modes, the neighboring modes of the neighboring modes. The loss of optical power is more drastic or accelerated in the IPE curves than in the SPS curves.

In all cases considered it is observed that for values of W that are after the peaks of the SPS curves, the SPS seems to over-estimate the power fractions, whether it be the power retained or the crosstalk. In all these cases the numerical simulations seem to agree more with the IPE curves than the SPS. However, it is observed that in some instances the IPE predictions are slightly above the numerical simulations results. The reason may be that in deriving the IPE predictions, we make use of the quadratic structure function approximation, whereas the numerical simulations are done with the original Kolmogorov structure function.

Using the results of this work, we further consider a typical scenario where a laser beam with a waist radius of 1cm and a wavelength of 532 nm propagates over a distance of 1 km through moderate turbulence with $C_n^2 = 0.733 \times 10^{-14}$ m$^{-2/3}$. The above parameters correspond to a normalized turbulence strength of $\mathcal{K} = 0.07$. In the case that the laser beam profile is an LG mode with $\ell = 1$ and $p = 0$ our results indicate that only about 28 % of the power would be retained in this mode.

3.5 Conclusions

The coupling of optical power from one OAM mode, represented as an LG mode, to other different OAM modes due to atmospheric scintillation is investigated with the aid of the IPE model, SPS model, and numerical simulations. We compare the predictions of the IPE with those of the SPS. The IPE is valid under all scintillation conditions, whilst the SPS is only valid

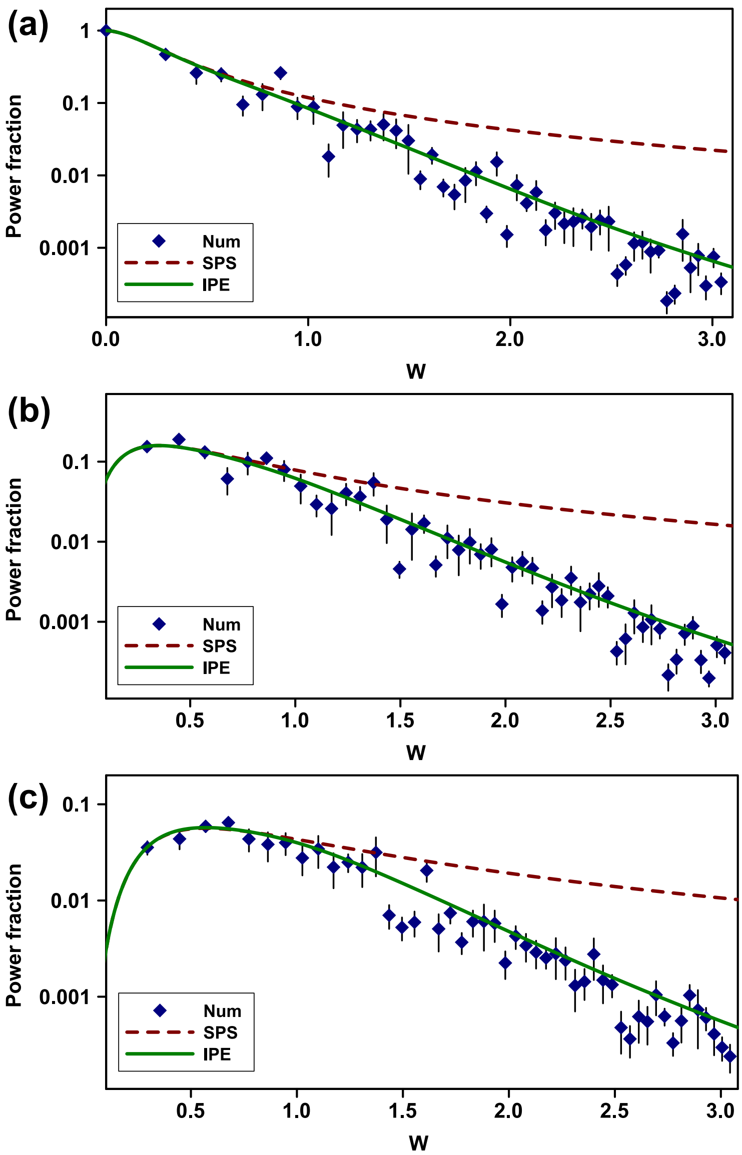

FIGURE 3.8: OAM Content as a function of scintillation strength, for turbulence conditions described by the normalized turbulence strength $K = 0.7$. a) Gives the amount of power in the input mode $\ell = 1$; b) Gives the amount of power in the mode $\ell = 2$;c) Gives the amount of power in the mode $\ell = 3$. The markers are the numerical simulation data, the dashed line is the SPS data, and the solid line is the IPE prediction.

under weak scintillation conditions. This comparison allows us to describe the qualitative behavior under various conditions. By way of independent numerical simulations based on the MPS approach, we show that the IPE predictions are more reliable over the SPS predictions, especially in strong scintillation.

Chapter 4

Hong-Ou-Mandel in turbulence

4.1 Introduction

Current research shows that for long distance quantum communication to be feasible there needs to be well developed quantum repeaters on quantum teleportation [28, 135]. The implementation of quantum teleportation requires a system that can perform joint measurements. Such measurements are also known as Bell measurements because they require the projection of the state of a pair of photons onto a Bell state. One way to perform such a joint measurement is with the aid of the Hong-Ou-Mandel (HOM) effect [136], according to which a photon pair entering both input ports of a balanced (50:50) beam splitter in an (anti)symmetric state leads to photon (anti)bunching at the output ports. A filter for antisymmetric Bell states can thus be realized by conditioning on coincidence photo-detection in the output ports of a balanced beam splitter. The HOM effect can also be used in a protocol to synchronize clocks remotely [137, 138] with high accuracy.

Free-space quantum communication uses the atmosphere as a transmission channel. Since the atmosphere can exhibit turbulent behavior, it is expected that this would interfere with the teleportation process. This expectation is based on the experience that turbulence can cause considerable disturbance of light modes traversing atmospheric channels, and thus may affect the quantum interference observed in the HOM effect. If the HOM synchronization protocol is implemented over an atmospheric channel [139], turbulence may in a similar way cause the synchronization process to fail.

In this chapter, a theoretical investigation of the effect of turbulence on the HOM interference effect is performed and experimental confirmation of the results is also provided. In particular, it is demonstrated that under certain conditions turbulence does not have any effect on the quantum interference in the HOM effect. This opens up the use of quantum communication and quantum synchronization via free-space channels.

The work on this chapter was done collaboratively with Dr. Shashi Prabhakar, Prof. Thomas Konrad, and Dr. Filippus S. Roux [140]. Particularly, I contributed to the theoretical calculations.

This chapter is organized as follows. We start in Sec. 4.2 with a brief explanation of the HOM effect. In Sec. 4.3 we consider the HOM for the situation of a one-sided channel, where one of the two photons after the SPDC process passes through turbulence under weak scintillation conditions. The other photon does not experience any turbulence. In Sec. 4.4 we discuss the situation for a two-sided channel, where both photons after the SPDC process pass through turbulence under weak scintillation conditions. The experimental setup is explained and the results are presented in Sec. 4.5. We provide some discussion in Sec. 4.6 and give a final summary in Sec. 4.7.

4.2 The Hong Ou Mandel effect

The Hong Ou Mandel (HOM) effect is a quantum mechanical interference effect that occurs when two photons meet at a 50:50 beam splitter. Let us consider a two-photon system state

$$|\psi\rangle = \sum_{j,k=1}^{N} \alpha_{jk}|1_j\rangle|1_k\rangle, \tag{4.1}$$

where (j,k) represents the label for the two photons in modes j and mode k, N is the Hilbert space dimension of the photons, α_{jk} is a complex amplitude which is required by normalization of the state to satisfy the condition

$$\sum_{j,k=1}^{N} |\alpha_{jk}|^2 = 1. \tag{4.2}$$

In terms of the creation operators $\hat{a}^\dagger$ the above state can be written as

$$|\psi\rangle = \sum_{j,k=1}^{N} \alpha_{jk}\hat{a}_j^\dagger\hat{a}_k^\dagger|0\rangle. \tag{4.3}$$

The state given in Eq. (4.3) is said to be symmetric if the interchange in the labels for the two photons does not change it. That is, in the case that $\alpha_{jk} = \alpha_{kj}$

$$|\psi^+\rangle = \sum_{j>k=1} \alpha_{jk}\left(\hat{a}_j^\dagger\hat{a}_k^\dagger + \hat{a}_k^\dagger\hat{a}_j^\dagger\right)|0\rangle + \sum_{jj}\alpha_{jj}\hat{a}_j^\dagger\hat{a}_j^\dagger|0\rangle. \tag{4.4}$$

It is considered to be anti-symmetric if $\alpha_{jk} = -\alpha_{kj}$ which leads to the state

$$|\psi^-\rangle = \sum_{j>k=1} \alpha_{jk}\left(\hat{a}_j^\dagger\hat{a}_k^\dagger - \hat{a}_k^\dagger\hat{a}_j^\dagger\right)|0\rangle. \tag{4.5}$$

Without any loss of generality, we can consider the state of the two-photon system prior to entering the beam splitter to be given by

$$|\psi_{\text{in}}\rangle = \hat{a}_A^\dagger\hat{a}_B^\dagger|0\rangle_A|0\rangle_B, \tag{4.6}$$

where A and B denote the two different paths of the input photons, $\hat{a}_A^\dagger$ and $\hat{a}_B^\dagger$ are the creation operators for the photons in the respective paths. The two different paths can be referenced to the two input ports of the beam splitter as is shown in Fig. 4.1.

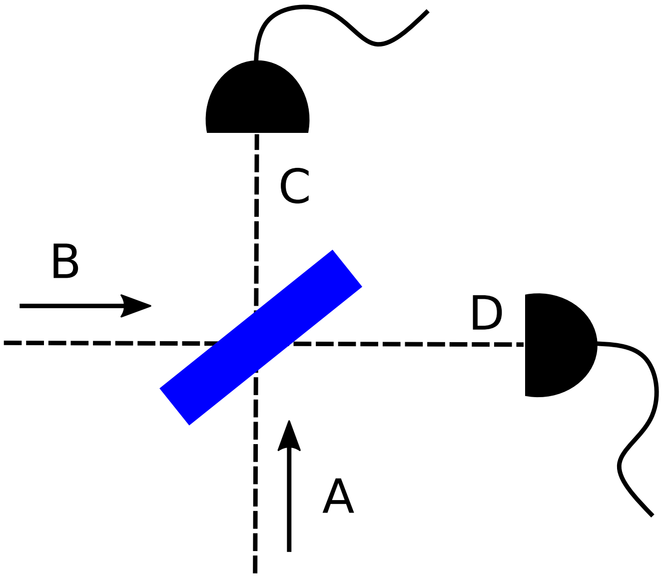

FIGURE 4.1: Schematic representation of a 50:50 beam splitter. The two photons are incident on ports A and B, respectively. They can exit through the ports C and D. Upon exit, they are recorded by avalanche photodetectors (APDs).

The operation of the beam splitter is represented by a unitary operator $\hat{U}_{\text{bs}}$ [141] such that

$$\begin{aligned} \hat{a}_A^{\dagger} &\longrightarrow \frac{1}{\sqrt{2}}\left(\hat{a}_C^{\dagger} + \hat{a}_D^{\dagger}\right) \\ \hat{a}_B^{\dagger} &\longrightarrow \frac{1}{\sqrt{2}}\left(\hat{a}_C^{\dagger} - \hat{a}_D^{\dagger}\right), \end{aligned} \tag{4.7}$$

where C and D represent the output ports of the beam splitter as can be seen in Fig. 4.1. Upon entering the beam splitter, the output state is given by

$$\begin{aligned} |\psi_{\text{out}}\rangle &= \hat{U}_{\text{bs}}|\psi_{\text{in}}\rangle \\ &= \frac{1}{2}\left(\hat{a}_C^{\dagger}\hat{a}_C^{\dagger} - \hat{a}_C^{\dagger}\hat{a}_D^{\dagger} + \hat{a}_D^{\dagger}\hat{a}_C^{\dagger} - \hat{a}_D^{\dagger}\hat{a}_D^{\dagger}\right)|0\rangle, \end{aligned} \tag{4.8}$$

where the second equality is obtained upon substitution of Eq. (4.7) into Eq. (4.6). The four terms in the above equation correspond to the four different configurations of the output of the beam splitter. These output configurations are shown in Fig. 4.2.

In the case that the input state is the symmetric state in Eq. (4.4), the output becomes

$$\begin{aligned} |\psi_{\text{out}}\rangle &= \sum_{j>k=1} \alpha_{jk}\left[|1_j, 1_k\rangle_C \otimes |0\rangle_D - |0\rangle_C \otimes |1_j, 1_k\rangle_D\right] \\ &\quad + \frac{1}{\sqrt{2}}\sum_j \alpha_{jj}[|2_j\rangle_C \otimes |0\rangle_D - |0\rangle_C \otimes |2_j\rangle_D]. \end{aligned} \tag{4.9}$$

This means that when the two input photons are described by a symmetric state and enter a 50:50 beam splitter the output state represents a bunching phenomenon. That is, the two-photons always come out from the same port of the beam splitter; either both exit through port C or they both exit through port D. This result implies that a measurement of the coincidence

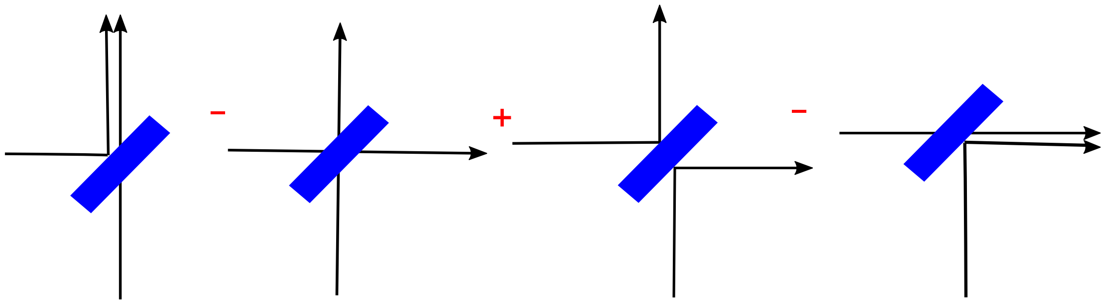

FIGURE 4.2: Simplified schematic representation of the possible output configurations when two indistinguishable photons are incident on a 50:50 beam splitter.

counts of two photons(in a symmetric state) incident on a beam splitter would yield zero results.

In the case that the two photon system is described by an anti-symmetric state we have that

$$|\psi_{\text{out}}\rangle = \sum_{j,k>1} \alpha_{jk} \left[|1_j\rangle_C \otimes |1_k\rangle_D - |1_k\rangle_C \otimes |1_j\rangle_D \right] . \tag{4.10}$$

This result implies that in the case of an anti-symmetric input state the probability of measuring coincidence counts is non-zero. We note that because of the condition imposed on the complex coefficients, $\alpha_{jk} = -\alpha_{kj}$, the case for $j = k$ gives a null result. Therefore, in the anti-symmetric state, the mode labels j and k are always different.

The discussed results, especially the symmetric input state case, are the basis upon which the applications of the HOM are based. In the next few sections, we will look at the consequences of atmospheric turbulence on the above phenomenon. We consider two different cases: The first case is based on sending only one of the two photons through the atmospheric turbulence, and the second case is based on propagating both the photons through atmospheric turbulence.

4.3 One-sided weak scintillation

In weak scintillation, we assume that the only effect of the atmospheric turbulence is a mere phase perturbation. Therefore, an optical field propagating through the atmosphere does not experience any amplitude variations. In this section we look at the instance where for the entangled photonic system prepared by way of spontaneous parametric down conversion (SPDC)[1], only one of the entangled photons is propagated through the atmosphere. The atmospheric turbulence is considered to be well within the conditions of weak scintillation.

We performed an analytical calculation and an experiment for the one-sided case, and we observed that the visibility of the HOM dip does not change so long as the atmospheric turbulence conditions are those of weak scintillation, see Fig. 4.4. In the experiment, we, however, observed some fluctuations which could be attributed to the noise in the system. The visibility, which is defined as the counts outside minus counts inside divided by counts outside plus

[1] The spontaneous parametric downconversion process is discussed in Chapter 2.

counts inside,

$$\mathcal{V} = \frac{C_{\text{out}} - C_{\text{in}}}{C_{\text{out}} + C_{\text{in}}}, \tag{4.11}$$

where C_{out} and C_{in} are the coincidence counts outside and inside the dip, respectively, remains the same even if we increase the turbulence strength as long as the scintillation is within the weak limit. This result is counter-intuitive as one would have expected the scintillation to pollute the symmetric SPDC input state with an antisymmetric component. In the remainder of this section, we explore the physics of how this counter-intuitive phenomenon comes about.

The model for the analytical calculations follows the order and detail as the experimental setup for observation of the robustness of the HOM dip which is described in detail below, Sec. 4.5. This order can be summarised as follows: (a) The input state is an SPDC state, which is symmetric with respect to an exchange of the photon-paths. (b) The turbulence is modeled as a single phase screen (assuming weak scintillation conditions). (c) The single phase screen for the turbulence is only placed in one of the two paths, representing a one-sided turbulence channel. (d) The output after the HOM filter (beam splitter) is measured by means of projections onto particular LG modes in the respective output ports. These modes all have radial index $p = 0$ and the magnitude of their azimuthal index is $|\ell| = 1$.

The state obtained from the SPDC process can be expressed in terms of an expansion of symmetric Bell-states $|\Psi_\ell^+\rangle$, consisting of LG modes with azimuthal index ℓ

$$|\psi_{\text{SPDC}}\rangle = \sum_{\ell=0}^{\infty} |\Psi_\ell^+\rangle \alpha_\ell, \tag{4.12}$$

where α_ℓ are the expansion coefficients, and the symmetric (antisymmetric) Bell-state $|\Psi_\ell^+\rangle$ ($|\Psi_\ell^-\rangle$) is defined by

$$|\Psi_\ell^\pm\rangle = \frac{1}{\sqrt{2}} \left(|\ell\rangle_A |\bar{\ell}\rangle_B \pm |\bar{\ell}\rangle_A |\ell\rangle_B \right), \tag{4.13}$$

with $\bar{\ell} = -\ell$.

In the absence of atmospheric turbulence, the HOM filter performs as expected and we should be able to use it for any of its intended applications. This implies, as can be seen from the SPDC state above, that the HOM effect (dip) is made possible by the symmetric Bell states. In the one-sided case, it turns out that to ascertain or rather investigate the effect of atmospheric turbulence on HOM interference it is sufficient to check if the atmospheric turbulence leads to a generation of antisymmetric Bell states. This is because the antisymmetric Bell state adds coincidence counts inside the dip, therefore it should gradually fill in the dip. However, this does not happen.

To commence our investigation we consider the transition amplitude

$$\eta_\ell = \langle \Psi_\ell^- | \mathbb{1}_A \otimes \hat{T}_B | \psi_{\text{SPDC}} \rangle, \tag{4.14}$$

where $\hat{T}_B$ is the turbulence operator (in path B) representing a particular realization of the turbulence, and $\mathbb{1}_A$ is the identity operator (in path A). The robustness of the HOM dip implies that $\eta_\ell = 0$ for all ℓ, irrespective of the scintillation strength. In the statistical analysis, the results are averaged over all possible realizations. However, to observe on average a vanishing coincidence count for the HOM dip, all the individual realizations must show vanishing transition amplitudes $\eta_\ell = 0$ in the dip. Therefore, we need to consider the individual realizations.

By substituting the expanded SPDC state, given in Eq. (4.12), into the transition amplitude we obtain

$$\eta_\ell = \sum_{m=0}^{\infty} \langle \Psi_\ell^- | \mathbb{1}_A \otimes \hat{T}_B | \Psi_m^+ \rangle \alpha_m. \tag{4.15}$$

Due to the identity operation in path A, initial and final azimuthal indices must coincide $m = \ell$. Hence, the only term that can contribute to the transition is

$$\eta_\ell = \langle \Psi_\ell^- | \mathbb{1}_A \otimes \hat{T}_B | \Psi_\ell^+ \rangle \alpha_\ell. \tag{4.16}$$

Thus we see that η_ℓ reduces to the transition amplitude between the symmetric Bell state and its corresponding antisymmetric Bell state.

Next, we substitute Eq. (4.13) into Eq. (4.16) and evaluate the inner products in path A (the side without turbulence) to obtain

$$\begin{aligned} \eta_\ell &= \frac{\alpha_\ell}{2} \left(\langle \bar{\ell} |_B \hat{T}_B | \bar{\ell} \rangle_B - \langle \ell |_B \hat{T}_B | \ell \rangle_B \right) \\ &= -\frac{\alpha_\ell}{2} \mathrm{tr}\{ \hat{T}_B \hat{\sigma}_z \}, \end{aligned} \tag{4.17}$$

where

$$\hat{\sigma}_z = \begin{bmatrix} 1 & 0 \\ 0 & -1 \end{bmatrix}$$

is the operator for the Pauli z-matrix (it has already been introduced in Chapter 2, but it is restated here again for convenience), defined in the $|\ell|$-subspace. It thus turns out that the transition amplitude is given by the coefficient of the $\hat{\sigma}_z$ component of the turbulence operator when expanded as a Bloch representation for a qubit channel.

To determine the coefficient for $\hat{\sigma}_z$ in the Bloch representation of $\hat{T}_B$, we convert the expression to the spatial domain. For this purpose we define the single phase screen turbulence operator by

$$\hat{T}_B = \int |\mathbf{x}\rangle \exp[\mathrm{i}\theta_i(\mathbf{x})] \langle \mathbf{x}| \ \mathrm{d}^2 x, \tag{4.18}$$

where $\theta_i(\mathbf{x})$ is a particular realization of a random phase function that represents the effect of the turbulence. Applying this definition in the expression for the transition amplitude, we obtain

$$\begin{aligned} \eta_\ell = \ & \frac{\alpha_\ell}{2} \int \langle \bar{\ell} | \mathbf{x} \rangle \exp[\mathrm{i}\theta_i(\mathbf{x})] \langle \mathbf{x} | \bar{\ell} \rangle \\ & - \langle \ell | \mathbf{x} \rangle \exp[\mathrm{i}\theta_i(\mathbf{x})] \langle \mathbf{x} | \ell \rangle \ \mathrm{d}^2 x. \end{aligned} \tag{4.19}$$

Next, we define the OAM modes in polar coordinates

$$\langle \mathbf{x} | \ell \rangle = R_{|\ell|}(r) \exp(\mathrm{i}\ell\phi), \tag{4.20}$$

and apply them in the expression. Since the turbulence is represented by a single local phase modulation (all located in the same plane), the input and output phase functions of the modes cancel each other, leaving only the r-dependent parts of the modes, which only depends on the magnitudes of the azimuthal index. These functions are the same for modes with the same magnitude of the azimuthal index. As a result, the two terms in Eq. (4.19) are equal and cancel each other, leaving us with $\eta_\ell = 0$. So we see that the transition amplitude is zero and the Bloch representation of $\hat{T}_B$ does not contain $\hat{\sigma}_z$.

In the next part, we try to put the above findings on a physical ground. What does it mean that the Bloch representation of $\hat{T}_B$ does not contain $\hat{\sigma}_z$?

To commence, we consider the matrix form and thus represent the turbulence operator as a 2×2 matrix as follows

$$\hat{T}_B = \begin{bmatrix} T_{11} & T_{12} \\ T_{21} & T_{22} \end{bmatrix}.$$

where the subscripts of the above matrix can be interpreted to mean that given T_{mn}, m is the input mode and n is the mode to which it scatters due to the turbulence. Therefore, T_{11} represents the complex amplitude for scattering into mode ℓ given that the photon started in mode ℓ, and T_{22} represents the complex amplitude for scattering into mode $\bar{\ell}$ for the photon that started in mode $\bar{\ell}$. That is, T_{11} and T_{22} describe the complex amplitudes for the photons to remain in their initial modes.

The trace operation in Eq. (4.17) becomes

$$\text{tr}\{\hat{T}_B\hat{\sigma}_z\} = T_{11} - T_{22}. \tag{4.21}$$

Since $\eta_\ell = 0$, it follows therefore that the complex amplitudes for the two photons to remain in their respective modes are exactly the same. That is, the atmospheric does not discriminate between ℓ and $\bar{\ell}$, it affects both modes in precisely the same manner.

The above results show why the HOM dip remains well-defined regardless of the scintillation strength. The atmospheric turbulence does not destroy the symmetry of the SPDC state. The only effect, which appears as a normalization factor in the more detailed calculations, is a decrease in the rate of the coincidence counts. As will be shown below in the experimental section, the visibility of the HOM dip is preserved even though the rate of data collection is slower. Nonetheless, it is however important to note that this explanation relies on the fact that the turbulence is simulated with a single phase screen (which is valid for weak scintillation conditions) and that it only acts on one of the two photons. Under different conditions, this mechanism may not apply anymore.

4.4 Two-sided weak scintillation

The second part of this work is based on the case where both photons are propagated through the atmosphere, albeit the conditions are still those of weak atmospheric scintillation. In contrast to the case of one-sided atmospheric turbulence, we observe a slight decrease in the quality of the HOM dip. The model and experimental setup are the same as those of Sec. 4.3, the only difference is that now both the photons produced through an SPDC process are propagated the atmospheric turbulence.

The analytical calculations for the two-sided case are more involved since two independent azimuthal indices have to be taken into account. We do not obtain the same simplification as was the case in Sec. 4.3. In the latter section, the identity operator in path A "forced" the indices m and ℓ to be the same. Therefore, we need to consider the calculations for this case in more detail.

Generically, one can represent the biphoton input state as produced by the SPDC process in terms of its spatial degrees of freedom as follows

$$|\psi\rangle = \int |\mathbf{r}_1\rangle_A |\mathbf{r}_2\rangle_B \psi(\mathbf{r}_1, \mathbf{r}_2)\ \mathrm{d}^3 r_1\ \mathrm{d}^3 r_2, \tag{4.22}$$

where $|\mathbf{r}\rangle$ represents a three-dimensional coordinate basis. In other words, we include the z-dependence, which relates to the path length, in addition to the two transverse (x, y) dependences. The wavefunction $\psi(\mathbf{r}_1, \mathbf{r}_2)$ is given in terms of the coordinate basis as

$$\psi(\mathbf{r}_1, \mathbf{r}_2) = \langle \mathbf{r}_1, \mathbf{r}_2 | \psi \rangle, \tag{4.23}$$

and it contains information about the SPDC state including the normalization of the state. The two photons are separated into different paths (or channels), labelled A and B, respectively.

It is shown in Chapter 2 that the phase matching conditions that lead to the momentum conservation are directly related to the transverse wave function of the SPDC state. Therefore, we can always separate the three-dimensional wave function into a transverse part and a longitudinal part as follows

$$\psi(\mathbf{r}_1, \mathbf{r}_2) = F(\mathbf{R}_1, \mathbf{R}_2) G(z_1, z_2). \tag{4.24}$$

By implication, the basis states also separate

$$|\mathbf{r}_1\rangle_A |\mathbf{r}_1\rangle_B = |\mathbf{R}_1, z_1\rangle_A |\mathbf{R}_2, z_2\rangle_B. \tag{4.25}$$

The HOM curve, and subsequently the dip is observed as a function of the relative path lengths, centered at zero relative path length.

To consider the effect of the path length difference for an SPDC state, we convert the expression to the Fourier domain in the z-dependence. Hence, we have

$$\begin{aligned} |\psi\rangle \quad = \quad & \int |\mathbf{R}_1, c_1\rangle_A |\mathbf{R}_2, c_2\rangle_B F(\mathbf{R}_1, \mathbf{R}_2) \exp(-\mathrm{i}2\pi c_1 z_1) \exp(-\mathrm{i}2\pi c_2 z_2) \\ & \times G(z_1, z_2)\ \mathrm{d}^2 r_1\ \mathrm{d}^2 r_2\ \mathrm{d}z_1\ \mathrm{d}z_2 \mathrm{d}c_1\ \mathrm{d}c_2, \end{aligned} \tag{4.26}$$

where $\mathbf{R}_1$ and $\mathbf{R}_2$ are two-dimensional transverse position vectors (x_1, y_1) and (x_2, y_2), respectively ; c_1 and c_2 are the longitudinal spatial frequency components (directly related to the wavelength of the light) associated with the z-components of the position vectors. The spatial correlations (due to momentum conservation in the SPDC process) are incorporated into $F(\mathbf{R}_1, \mathbf{R}_2)$. In changing the z dependent parts of the state vectors we have made use of the following rule

$$\begin{aligned} |\mathbf{R}_1, z_1\rangle_A |\mathbf{R}_2, z_2\rangle_B \quad = \quad & \int |\mathbf{R}_1, c_1\rangle_A |\mathbf{R}_2, c_2\rangle_B \exp(\mathrm{i}2\pi c_1 z_1) \exp(-\mathrm{i}2\pi c_2 z_2) \\ & \times \mathrm{d}c_1\ \mathrm{d}c_2. \end{aligned} \tag{4.27}$$

We proceed by making the following substitution for the z dependence

$$z_1 = z_0 + dz \quad \text{and} \quad z_2 = z_0 - dz, \tag{4.28}$$

whereafter we make a change of variables in the integrals (and on the z dependent function accordingly). As consequence of the change of variables we obtain a dependence on z_0 and on dz. In anticipation of the final effect which is meant to depend on the path length difference of the two photons we do not remove (we leave the final expression with the dz dependence) the dz integral. Nonetheless, after rearranging all the other integrals and associated terms we end up with an expression that contains the following term

$$\int S(z_0) \exp[-\mathrm{i}2\pi(c_1 + c_2)z_0] \mathrm{d}z_0, \tag{4.29}$$

where $S(\cdot)$ is the term obtained from $G(z_1, z_2)$ after the change of variables. After evaluation of the integral we obtain

$$\Pi(c_1, c_2) = h(2c_0 - c_1 - c_2)H(c_1)H(c_2). \tag{4.30}$$

The term $h(2c_0 - c_1 - c_2)$ captures the wavelength correlation (due to energy conservation in the SPDC process), where c_0 is the longitudinal spatial frequency that is associated with the wavelength of the pump beam. The nature of $h(\cdot)$ is discussed below. The individual spectra of the two photons, as determined by wavelength filters, are given by $H(c_1)$ and $H(c_2)$, respectively (see below). The final expression for the SPDC state is given by

$$\begin{aligned} |\psi\rangle \quad = \quad & \int |\mathbf{R}_1, c_1\rangle_A |\mathbf{R}_2, c_2\rangle_B F(\mathbf{R}_1, \mathbf{R}_2) \\ & \times \exp(\mathrm{i}2\pi c_1 dz) \exp(-\mathrm{i}2\pi c_2 dz) h(2c_0 - c_1 - c_2) \\ & \times H(c_1)H(c_2)\, \mathrm{d}^2r_1\, \mathrm{d}^2r_2\, \mathrm{d}c_1\, \mathrm{d}c_2. \end{aligned} \tag{4.31}$$

Both photons of the input state pass through simulated turbulence under weak scintillation conditions. As a result, we apply unitary operators $\hat{U}_A$ and $\hat{U}_B$ for the respective channels, representing the scintillation process caused by the turbulence. For single phase screen turbulence (weak scintillation), these unitary operators implement phase modulations $\hat{U}|\mathbf{R}\rangle = |\mathbf{R}\rangle \exp[\mathrm{i}\theta(\mathbf{R})]$. Hence

$$\begin{aligned} \hat{U}_A |\mathbf{R}_1, c_1\rangle_A \quad &= \quad |\mathbf{R}_1, c_1\rangle_A \exp[\mathrm{i}\theta_A(\mathbf{R}_1)] \\ \hat{U}_B |\mathbf{R}_2, c_2\rangle_B \quad &= \quad |\mathbf{R}_2, c_2\rangle_B \exp[\mathrm{i}\theta_B(\mathbf{R}_2)]. \end{aligned} \tag{4.32}$$

After the turbulence, the photons in paths A and B are sent into the two input ports of a balanced (50 : 50) beam splitter, as shown in Fig. 4.3, to perform the HOM filtering and obtain HOM interference. The unitary operator $\hat{U}_{\mathrm{bs}}$ that represents this beam splitter, performs the following transformations

$$\begin{aligned} |\mathbf{R}_1, c_1\rangle_A \quad &\to \quad \frac{1}{\sqrt{2}} \left(|\mathbf{R}_1, c_1\rangle_C + |\mathbf{R}_1, c_1\rangle_D\right) \\ |\mathbf{R}_2, c_2\rangle_B \quad &\to \quad \frac{1}{\sqrt{2}} \left(|\mathbf{R}_2, c_2\rangle_C - |\mathbf{R}_2, c_2\rangle_D\right), \end{aligned} \tag{4.33}$$

where the output ports are denoted by C and D, as shown in Fig. 4.3. Mirrors are added in the setup for the HOM filter so that every path from A or B to C or D have an even number of reflections, thus avoiding the inversion of the helicity of the modes. We apply the beamsplitter operation and then condition on observing coincidences at the two output ports. The result, just before the detection, reads

$$|\psi'\rangle = \hat{\mathcal{P}}_{\rm CC}\hat{U}_{\rm bs}\hat{U}_A\hat{U}_B|\psi\rangle, \tag{4.34}$$

where $\hat{\mathcal{P}}_{\rm CC}$ is a projection operator that selects out the coincidence part of the state. The operation of the beam splitter as depicted in Eq. (4.33) leads to a generation of four terms, however only two of those correspond to the detection of coincidences as is shown in Fig. 4.2. Therefore, $\hat{\mathcal{P}}_{\rm CC}$ corresponds to a selection of that part of the state, and it can be represented as follows

$$\begin{aligned}\hat{\mathcal{P}}_{\rm CC} \to \int |\mathbf{R}'_1, c'_1\rangle\langle\mathbf{R}'_1, c'_1|_D \otimes |\mathbf{R}'_2, c'_2\rangle\langle\mathbf{R}'_2, c'_2|_C \\ \times {\rm d}r'^2_1{\rm d}r'^2_2{\rm d}c'_1{\rm d}c'_2.\end{aligned} \tag{4.35}$$

To show how the above operator works we first start with the expression of the kets after the beam splitter

$$\begin{aligned}|\mathbf{R}_1, \mathbf{R}_2, c_1, c_2\rangle \equiv\; & |\mathbf{R}_1, c_1\rangle_C \otimes |\mathbf{R}_2, c_2\rangle_C - |\mathbf{R}_1, c_1\rangle_C \otimes |\mathbf{R}_2, c_2\rangle_D \\ & +|\mathbf{R}_1, c_1\rangle_D \otimes |\mathbf{R}_2, c_2\rangle_C \\ & -|\mathbf{R}_1, c_1\rangle_D \otimes |\mathbf{R}_2, c_2\rangle_D,\end{aligned} \tag{4.36}$$

the left-hand side is used loosely as a place holder of the right-hand side expression.

Upon acting on the beam splitter output state kets with $\hat{\mathcal{P}}_{\rm CC}$ it can be seen that the inner product of terms that correspond to the two photons coming out in the same port will go to zero, therefore we proceed by showing only the terms that correspond to the two photons coming out from different ports

$$\begin{aligned}\hat{\mathcal{P}}_{\rm CC}|\mathbf{R}_1, \mathbf{R}_2, c_1, c_2\rangle \equiv\; & -\int |\mathbf{R}_1, c_1\rangle_C \otimes |\mathbf{R}_2, c_2\rangle_D \delta\left(\mathbf{R}_1 - \mathbf{R}'_1\right)\delta\left(\mathbf{R}_2 - \mathbf{R}'_2\right) \\ & \times\delta\left(c_1 - c'_1\right)\delta\left(c_2 - c'_2\right){\rm d}r'^2_1{\rm d}r'^2_2{\rm d}c'_1{\rm d}c'_2 \\ & +\int |\mathbf{R}_1, c_1\rangle_D \otimes |\mathbf{R}_2, c_2\rangle_C \delta\left(\mathbf{R}_1 - \mathbf{R}'_1\right)\delta\left(\mathbf{R}_2 - \mathbf{R}'_2\right) \\ & \times\delta\left(c_1 - c'_1\right)\delta\left(c_2 - c'_2\right){\rm d}r'^2_1{\rm d}r'^2_2{\rm d}c'_1{\rm d}c'_2 \\ =\; & -|\mathbf{R}_1, c_1\rangle_C \otimes |\mathbf{R}_2, c_2\rangle_D \\ & +|\mathbf{R}_1, c_1\rangle_D \otimes |\mathbf{R}_2, c_2\rangle_C.\end{aligned} \tag{4.37}$$

To observe the HOM dip, we use SLMs to project the respective photon states onto particular spatial modes. For this purpose, we select a pair of LG modes with opposite azimuthal indices for the two respective photons, under condition of coincidence detection. The longitudinal degrees of freedom (associated with z) are not affected (filtered) in this process. The result is a post-selection in the transverse degrees of freedom onto a two-dimensional subspace of LG modes. We express the result of this projective measurement as the detection probability P, given by

$$P = \mathrm{tr}\{\hat{\mathcal{P}}_\ell \hat{\rho}\} = \langle\psi'|\hat{\mathcal{P}}_\ell|\psi'\rangle \tag{4.38}$$

where $\hat{\rho} = |\psi'\rangle\langle\psi'|$ is the density operator for the state after the beamsplitter and $|\psi'\rangle$ is given in Eq. (4.34). The projection operator, associated with the projective measurement, is given by

$$\hat{\mathcal{P}}_\ell = \mathbb{1}_z \otimes (|\ell_C, \bar{\ell}_D\rangle\langle\ell_C, \bar{\ell}_D|), \tag{4.39}$$

where $\mathbb{1}_z$ is an identity operator for the longitudinal degrees of freedom (associated with z). By implication, we assume that the LG modes are independent of the wavelength

$$\langle\mathbf{R}, c_1|\ell\rangle = \langle\mathbf{R}|\ell\rangle = u_\ell(\mathbf{R}), \tag{4.40}$$

where $u_\ell(\mathbf{R})$ is the LG mode with azimuthal index ℓ.

Note that, because the longitudinal degrees of freedom are not filtered, the expression for P would contain the squares of the functions that depend on the variables c_1 and c_2. In the measurement, therefore, we trace over the longitudinal degrees of freedom, which means that we need to integrate over c_1 and c_2. For this purpose, we replace the square of the h-function with a Dirac delta function,

$$h^2(2c_0 - c_1 - c_2) \to \delta(2c_0 - c_1 - c_2). \tag{4.41}$$

The function $h(\cdot)$ imposes energy conservation. However, if we assume that it is given by a Dirac delta function, then we will end up with a squared Dirac delta function, which would give a divergent result. Therefore, the above assignment, which considers the square of the function $h(\cdot)$, rather than the actual function itself as a Dirac delta function avoids such a complication.

We continue by redefining the integration variables $c_1 = c_0 + c_3$ and $c_2 = c_0 + c_4$. The Dirac delta will then assign $c_4 = -c_3$ after integrating over c_4. We will assume that the spectra can be defined in terms of a hat-function

$$H(c) = \Pi\left(\frac{c - c_c}{W}\right), \tag{4.42}$$

where W is the width of the spectrum (determined by the bandwidth of the line filters), c_c is the center frequency (of the line filters) and

$$\Pi(x) = \begin{cases} 1 & \text{for } |x| < 1/2 \\ 0 & \text{otherwise} \end{cases}. \tag{4.43}$$

Note that $\Pi^2(x) = \Pi(x)$. In the end, we have terms that contain either of two possible integrals over c_3:

$$\begin{aligned} \int H^2(c_0 + c_3) H^2(c_0 - c_3)\, \mathrm{d}c_3 &= W \\ \int H^2(c_0 + c_3) H^2(c_0 - c_3) & \\ \times \exp(\pm \mathrm{i} 8\pi c_3 dz)\, \mathrm{d}c_3 &= W \mathrm{sinc}(4\pi W dz). \end{aligned} \tag{4.44}$$

The random phase functions $\theta(\mathbf{R})$ in Eq. (4.32) represent specific realizations of the turbulent medium. We compute the ensemble average over all such realizations in both photon paths, independently, to obtain the averaged coincidence counts. The effect of the ensemble averaging is to convert the random phase factors into exponential functions

$$\mathcal{E}\{\exp[\mathrm{i}\theta(\mathbf{R}_1) - \mathrm{i}\theta(\mathbf{R}_2)]\} = \exp\left[-\frac{1}{2}D(\mathbf{R}_1 - \mathbf{R}_2)\right], \tag{4.45}$$

that contain the phase structure function $D(\mathbf{R}_1 - \mathbf{R}_2)$ [121]. One can now express the ensemble averaged detection probability by

$$\begin{aligned} P &= \int \exp\left[-\frac{1}{2}D(\mathbf{R}_1 - \mathbf{R}_3)\right] \exp\left[-\frac{1}{2}D(\mathbf{R}_2 - \mathbf{R}_4)\right] \\ &\quad \times [F(\mathbf{R}_1, \mathbf{R}_2)F^*(\mathbf{R}_3, \mathbf{R}_4) + F(\mathbf{R}_2, \mathbf{R}_1)F^*(\mathbf{R}_4, \mathbf{R}_3)] \\ &\quad \times \left[u_\ell^*(\mathbf{R}_1)u_{\bar{\ell}}^*(\mathbf{R}_2) - \mathrm{sinc}(4\pi W dz)u_\ell^*(\mathbf{R}_2)u_{\bar{\ell}}^*(\mathbf{R}_1)\right] \\ &\quad \times u_\ell(\mathbf{R}_3)u_{\bar{\ell}}(\mathbf{R}_4)\ \mathrm{d}^2r_1\ \mathrm{d}^2r_2\ \mathrm{d}^2r_3\ \mathrm{d}^2r_4. \end{aligned} \tag{4.46}$$

For the purpose of the calculations, we will assume $|\ell| = 1$ and radial index $p = 0$. In Cartesian coordinate, the LG mode with these indices is simply expressed by

$$u_1(\mathbf{R}) = (x + \mathrm{i}y)\exp\left(-\frac{|\mathbf{R}|^2}{w_0^2}\right), \tag{4.47}$$

where w_0 is the mode size for the LG mode and where we ignore the normalization constant.

The function $F(\mathbf{R}_1, \mathbf{R}_2)$, which represents the spatial correlation of the down-converted state, can be represented in the Fourier domain as the product of the pump beam

$$\exp\left(-\frac{w_p^2}{4}|\mathbf{K}_1 + \mathbf{K}_2|^2\right), \tag{4.48}$$

and the phase matching function,

$$\mathrm{sinc}\left(\frac{\beta w_p^2}{8}|\mathbf{K}_1 - \mathbf{K}_2|^2\right), \tag{4.49}$$

where $\mathbf{K}_1$ and $\mathbf{K}_2$ are the two dimensional transverse Fourier coordinates (k_{x1}, k_{y1}) and (k_{x2}, k_{y2}), respectively.

The argument of the pump beam consists of the sum of the Fourier domain coordinate vectors of the down-converted beams, due to the transverse phase matching condition (momentum conservation). The argument of the phase matching function, on the other hand, is the difference of the coordinate vectors of the down-converted beams, as a result of the paraxial condition. Details of the SPDC process are given in Chapter 2.

Often, the phase matching function is approximated by a Gaussian function [142], which is more tractable than the sinc-function found in the expression of the actual phase matching function. Such an approximation is only valid in the thin crystal limit. Beyond this limit, the sub-leading term of the Gaussian approximation gives a different scale behavior than that of the sinc-function

$$\exp(-\beta|\mathbf{K}|^2) \approx 1-\beta|\mathbf{K}|^2+\mathrm{O}\left(\beta^2\right) \tag{4.50}$$

$$\mathrm{sinc}(\beta|\mathbf{K}|^2) \approx 1-\frac{1}{6}\beta^2|\mathbf{K}|^4+\mathrm{O}\left(\beta^4\right). \tag{4.51}$$

Since we are interested in the behavior beyond the thin crystal limit, we need to consider the phase matching function in terms of the sinc-function. To alleviate the calculation, we'll use an auxiliary integral to represent the sinc-function [143]

$$\mathrm{sinc}(x)=\frac{1}{2}\int_{-1}^{1}\exp(\mathrm{i}x\xi)\,\mathrm{d}\xi. \tag{4.52}$$

After an inverse Fourier transform, the spatial correlation function is expressed as

$$\begin{aligned} F(\mathbf{R}_1,\mathbf{R}_2) &= \frac{\mathcal{N}}{2w_p^2}\exp\left(-\frac{|\mathbf{R}_1+\mathbf{R}_2|^2}{4w_p^2}\right) \\ &\quad\times\int_{-1}^{1}\frac{1}{\xi}\exp\left(-\mathrm{i}\frac{|\mathbf{R}_1-\mathbf{R}_2|^2}{2\xi\beta w_p^2}\right)\,\mathrm{d}\xi, \end{aligned} \tag{4.53}$$

where $\mathcal{N}$ is a normalization constant, w_p is the pump beam radius and β is the crystal ratio, defined as the crystal length L (times the ordinary refractive index of the crystal n_o) divided by the pump Rayleigh range z_R

$$\beta=\frac{n_o L}{z_R}=\frac{n_o L\lambda}{\pi w_p^2}, \tag{4.54}$$

with λ being the pump wavelength.

To enable the analytic evaluation of the integrals, we use a quadratic structure function approximation [85]

$$D(\Delta\mathbf{R})=6.88\mathcal{W}^{5/3}\frac{|\Delta\mathbf{R}|^2}{w_p^2}, \tag{4.55}$$

where

$$\mathcal{W}=\frac{w_p}{r_0}, \tag{4.56}$$

with

$$\Delta\mathbf{R}=\mathbf{R}_1-\mathbf{R}_2, \tag{4.57}$$

and

$$r_0=0.185\left(\frac{\lambda^2}{C_n^2 z}\right)^{3/5}, \tag{4.58}$$

being the Fried parameter [144]. Here, C_n^2 is the refractive index structure constant and z is the propagation distance.

Once all these functions, Eqs. (4.47), (4.53) and (4.55), are substituted into Eq. (4.46), one can evaluate the integrals. Those that involve $\mathbf{R}_1$, $\mathbf{R}_2$, $\mathbf{R}_3$ and $\mathbf{R}_4$ are readily evaluated. The remaining auxiliary integrations (associated with the sinc-functions) are somewhat more challenging but still tractable. The resulting expression for the probability to measure coincidence counts is complicated we performed a truncation with respect to β, and only present the expression for the values of up to order 5. This truncation is only for the purpose of presenting the expressions in a contained way. However, in the case of calculations, we do not have to limit accuracy in any way. Performing such a truncation leads to expressions that are relatively simpler and thus easier to simplify. Nonetheless, this approximation is tenable since β is an experimental parameter that is very small, and can be regulated if required. After performing the truncation and a series of simplifying steps we find that the expression has the form

$$P = f_1(\alpha,\beta,\zeta)\left[1-\mathrm{sinc}(4\pi W dz)\right] + \zeta^2\beta^4 f_2(\alpha,\zeta), \tag{4.59}$$

where

$$\begin{aligned} f_1(\alpha,\beta,\zeta) = \frac{\mathcal{N}_0}{\mathcal{Y}_0}\Big[& \alpha^6\beta^4\zeta^2\mathcal{Y}_{10} + 2\alpha^5\beta^4\zeta\mathcal{Y}_{11} \\ & -30\alpha^6\beta^2\zeta\mathcal{Y}_8 - 120\alpha^5\beta^2\mathcal{Y}_2^2\mathcal{Y}_3 + \alpha^4\beta^4\mathcal{Y}_{12} \\ & -120\alpha^4\beta^2\mathcal{Y}_2\mathcal{Y}_4 + \alpha^3\beta^4\mathcal{Y}_9 + \alpha^6\mathcal{Y}_6 \\ & +\alpha^2\beta^4\mathcal{Y}_7 - 720\alpha^5\mathcal{Y}_1 - \alpha^3\beta^2\mathcal{Y}_1 \\ & +\alpha\beta^4\mathcal{Y}_5 + 720\alpha^4 - 1440\alpha^2\beta^2 + 2160\beta^4\Big], \end{aligned} \tag{4.60}$$

$$f_2(\alpha,\zeta) = \alpha^2\frac{\mathcal{N}_0}{\mathcal{Y}_0}\left[\mathcal{Y}_{13}\alpha^4 + 2\mathcal{Y}_{14}\alpha^3 + \mathcal{Y}_{15}\alpha^2 + \mathcal{Y}_{16}\alpha + 320\right] \tag{4.61}$$

with

$$\begin{aligned} \mathcal{Y}_0 &= \alpha^2(2\alpha\zeta+\alpha+2)^3(\alpha+2)^3 \\ \mathcal{Y}_1 &= 2880\zeta + 1920 \\ \mathcal{Y}_2 &= \zeta + 1 \\ \mathcal{Y}_3 &= 5\zeta + 1 \\ \mathcal{Y}_4 &= 17\zeta + 7 \\ \mathcal{Y}_5 &= 6480\zeta + 3216 \\ \mathcal{Y}_6 &= 360\zeta^2 + 360\zeta + 180 \\ \mathcal{Y}_7 &= 7824\zeta^2 + 8040\zeta + 1676 \\ \mathcal{Y}_8 &= 2\zeta^3 + 6\zeta^2 + 7\zeta + 2 \\ \mathcal{Y}_9 &= 4848\zeta^3 + 8016\zeta^2 + 3352\zeta + 344 \\ \mathcal{Y}_{10} &= 24\zeta^4 + 60\zeta^3 + 136\zeta^2 + 73\zeta + 10 \\ \mathcal{Y}_{11} &= 126\zeta^4 + 456\zeta^3 + 509\zeta^2 + 159\zeta + 10 \\ \mathcal{Y}_{12} &= 1596\zeta^4 + 3984\zeta^3 + 2694\zeta^2 + 516\zeta + 20 \\ \mathcal{Y}_{13} &= 60\zeta^3 + 30\zeta^2 \\ \mathcal{Y}_{14} &= 60\zeta^3 + 140\zeta^2 + 40\zeta \\ \mathcal{Y}_{15} &= 440\zeta^2 + 480\zeta + 80 \\ \mathcal{Y}_{16} &= 640\zeta + 320 \end{aligned}$$

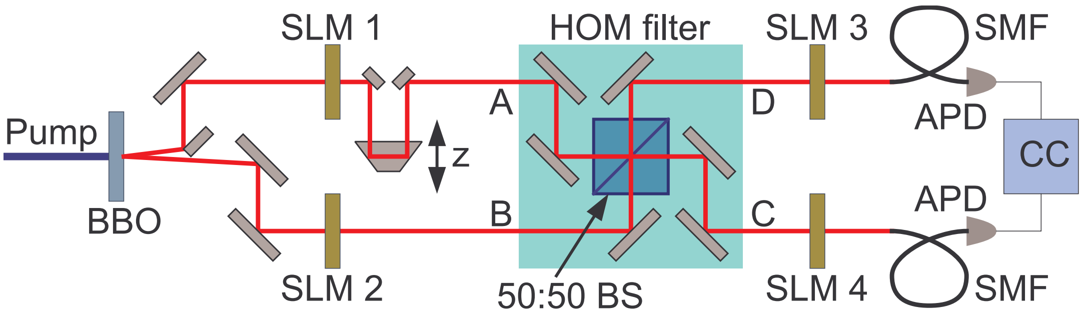

FIGURE 4.3: Experimental setup used to observe the Hong-Ou-Mandel dip after the quantum state has passed through one-sided or two-sided single phase screen turbulence.

β is defined in Eq. (4.54) and

$$\alpha = \frac{w_0^2}{w_p^2} \tag{4.62}$$

$$\zeta = 6.88\mathcal{W}^{5/3}, \tag{4.63}$$

$\mathcal{N}_0$ is a normalization constant.

The factor $[1 - \text{sinc}(4\pi W dz)]$ represents the shape of the HOM dip. The first term in Eq. (4.59), $f_1(\alpha, \beta, \zeta)$, by itself gives a constant dip. It represents a scaling factor, that can be thought of in terms of the overall counts. That is, it indicates the level of coincidence counts for the curve. The second term, $f_2(\alpha, \zeta)$, on the other hand, serves to fill in the dip and thereby reduces its quality. Therefore, this is the term that represents the washing-out of the HOM dip. Nonetheless, we see that this term contains a factor of ζ^2, which means that, for no turbulence, it is zero, as it should, and we thus observe the HOM dip as normal. We also see that it contains a factor of β^4, which implies that this term is quite small because the value of β tends to be small in typical experiments. Therefore, we see that even in the two-sided channel, the effect of the turbulence on the quality of the dip is small.

4.5 Experimental setup and results

The experimental setup is shown in Fig. 4.3. A mode-locked laser source with a wavelength of 355 nm, an average power of 350 mW and a repetition rate of 80 MHz is used. The pump beam has a beam radius of 58.9 μm and was characterized with a spirikon camera. It pumps a 3 mm-thick type I BBO crystal to produce noncollinear, degenerate photon pairs via SPDC with a wavelength of 710 nm. A small noncollinear angle of $\sim$3 degrees exists between the signal and idler beams. The plane of the crystal is imaged onto SLM1 and SLM2, via paths A and B, respectively, with a magnification of $\times 4$ (4-f system with $f_1 = 100$ mm and $f_2 = 400$ mm not shown). The atmospheric turbulence is simulated by random phase modulations, using either SLM1 (in path A) for the single-sided case or with both SLM1 and SLM2 (in path A

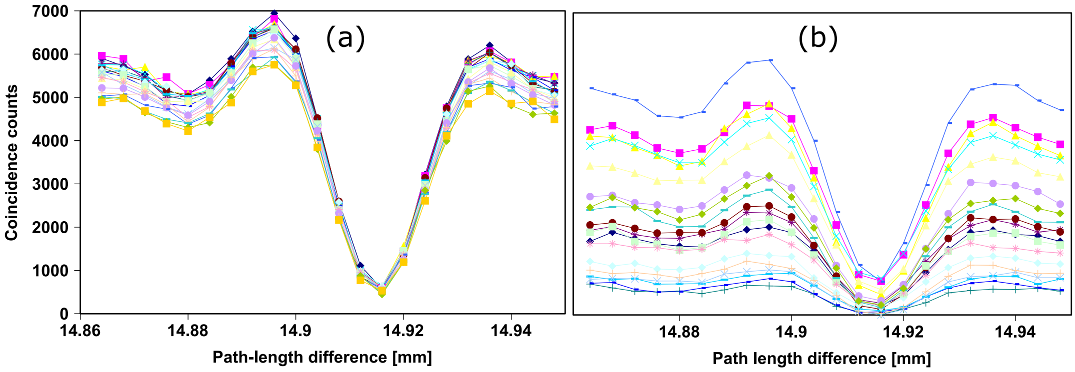

FIGURE 4.4: Experimentally observed HOM dip curves in the one-sided case for (a) $\mathcal{W} = 0$ and (b) $\mathcal{W} = 0.4$.

and B, respectively) for the double-sided case. The SLM that were used are both HOLOEYE PLUTO-2 with resolution 1920 x 1080, pixel-pitch of 8 μm, wavelength range 350-1700 nm, and Fill factor 93%.

The atmospheric turbulence is simulated according to the Kolmogorov theory of turbulence and modeled as a single phase screen approximation. The two mirror combination in arm A, which is used for changing the relative path length between the two arms, is mounted on a motorized translation stage. This allows one to scan through the dip in coincidence counts as a function of the relative path length difference dz. The plane of SLM1 and SLM2 are imaged onto SLM3 and SLM4 without magnification (4f system with $f_3 = 500$ mm and $f_4 = 500$ mm not shown).

By selecting particular LG modes for detection, projective measurements are performed using SLM3 and SLM4, together with the single mode fibers (SMFs). We detect $\ell = 1$ on SLM3 and $\ell = -1$ on SLM4. The mode size of the LG modes programmed on SLM3 and SLM4 is $w_0 = 450.0$ μm. Diffraction gratings are included in the random functions in both SLMs to separate different diffraction orders. The SLM3 and SLM4 planes are re-imaged with a demagnification factor of $\times 375$ (4-f system with $f_5 = 750$ mm and $f_6 = 2$ mm not shown) onto the SMFs. The back-propagated beams from the SMFs have beam radii of 882 μm and 838 μm on the planes of SML3 and SLM4, respectively. After SLM3 and SLM4, the two beams pass through 10 nm bandwidth interference filters (IF) before coupling into the SMFs. Avalanche photodiodes (APDs) at the ends of the SMFs are used to register the photon pairs with the aid of a coincidence counter (CC). The measured coincidence counts are accumulated over a 25 s integration time, with a gating time of 12.5 ns (based on the repetition rate of the laser).

The experimental parameters give $\alpha = 4.19$ and $\beta = 0.173$. They are specifically chosen to give a value of β that is not too small.

We performed several runs for each of the different values of the parameter $\mathcal{W}$, ranging from 0 to 2. During each run, the same random phase screen is used to measure the coincidence counts after the HOM filter over a range of path-length differences. In Fig. 4.4, we show the experimentally observed curves of the HOM dip in the case of a one-sided turbulence channel,

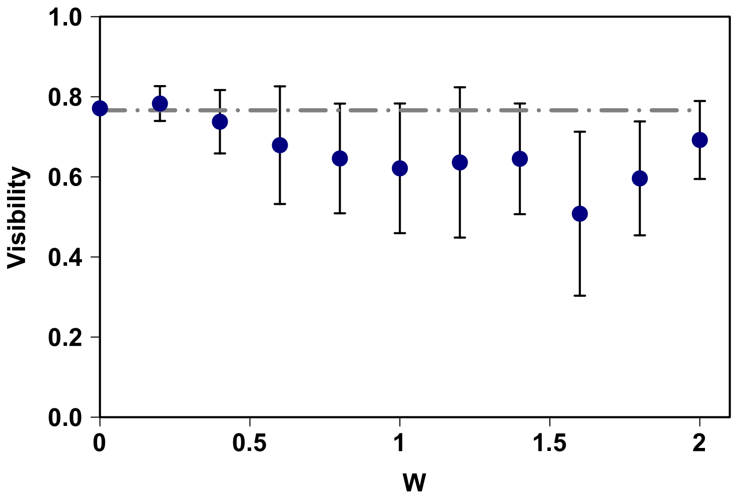

FIGURE 4.5: Visibility of the HOM dip as a function of $\mathcal{W}$ for the case of a one-sided turbulent channel. Experimental values are shown as blue-filled circles with vertical error bars, denoting the standard deviation. The horizontal gray dashed line represents the best fit constant visibility.

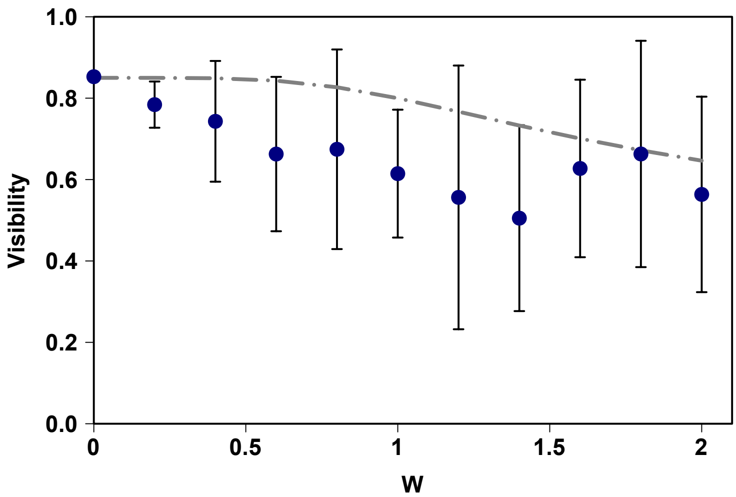

FIGURE 4.6: Visibility of the HOM dip as a function of $\mathcal{W}$ for the case of a two-sided turbulent channel. Experimental values are shown as blue-filled circles with vertical error bars, denoting the standard deviation. The gray dashed curve represents the theoretically calculated result, but with lower initial visibility to fit the experimental value for no turbulence.

for $\mathcal{W} = 0$ and $\mathcal{W} = 0.4$. The data points of each run are connected by straight lines to guide the eye. The curves in Fig. 4.4(a) are for no turbulence, $\mathcal{W} = 0$. One can see well-defined curves with very little variation among the different runs. The observed variation in Fig. 4.4(a) is caused by variations in the experimental conditions (laser intensity and optical alignment) that occurred over the duration of the experiment.

For a moderate scintillation of $\mathcal{W} = 0.4$ in the one-sided turbulence channel, one observes much more fluctuation in the curves for the different runs, as seen in Fig. 4.4(b). The large deviations, in this case, are caused by the different random phase screens that are used in the different runs. Although these phase screens are all produced to represent the same scintillation strength $\mathcal{W} = 0.4$, they cause different levels of scattering, leading to different levels of coincidence counts. Despite the large variation in the levels of coincidence counts among these curves, the shape of the dip is still clearly recognizable in them.

The background counts, which are caused by accidental coincidence counts and are readily calculated from the single beam counts and the gating time of the coincidence counter, have been subtracted from the raw data. The curves in Fig. 4.4 show the data after background subtraction.

By plotting the coincidence counts as a function of the path-length differences, one can clearly see the shape of the HOM dip. The inverted sinc-function shape is an artifact of the wavelength filters that were used in the experiment as is shown by calculations in Sec. 4.4.

For each of the curves, we computed the visibility of the dip which is defined in Eq. (4.11). We computed the averages and standard deviations of these visibilities for each value of $\mathcal{W}$. The result of the one-sided case is shown in Fig. 4.5. We also show a constant value as a gray dashed line with the best fit value for the constant visibility of $\mathcal{V} = 0.77 \pm 0.03$. Due to experimental imperfections, this value is smaller than the ideal value of 1. We see that the experimental results maintain this constant value with good agreement, even up to a value of $\mathcal{W} = 2$, which is considered to be a fairly large value for $\mathcal{W}$. Variations in the behavior are usually expected to occur in the vicinity of $\mathcal{W} = 1$ for $\ell = 1$ [78]. One can argue that, if the visibility of the HOM dip behaved in a way similar to entanglement [78], then for $\ell = 1$ it would undergo decay in the region of $\mathcal{W} = 1$. One would then have expected to see the visibility approaching zero at $\mathcal{W} = 2$. Our results show unambiguously that the visibility is still much larger than zero at $\mathcal{W} = 2$ by several standard deviations, without any indication of a decaying trend.

The visibility for the two-sided case is shown in Fig. 4.6. Here, we also show the curve for the theoretical calculation as a gray dashed curve. The theoretical curve has been multiplied with a factor to lower the initial value down from 1 so that it would match the lower visibility of the experimental results when no turbulence is present. The theoretical curve remains at a fairly high value of the visibility, even up to a value of $\mathcal{W} = 2$. The experimental results follow this trend fairly well.

Due to the large fluctuations, which cause relatively large error bars, typical in turbulence experiments, one cannot confirm the precise shape of the predicted curve. However, the experimental data is consistent with the theoretical curve. It shows that the visibility remains above zero up to a value of $\mathcal{W} = 2$. As with the one-sided case, one would have expected that, if the visibility were to decay, it should happen around $\mathcal{W} = 1$. Since this is not observed, the data support the theoretical finding that the visibility is fairly insensitive to scintillation.

4.6 Discussion

Our analysis shows that the fact the HOM dip is not affected by subjecting the photons to atmospheric turbulence is not a consequence of the second order quantum interference, rather it is a result of the properties of the atmospheric turbulence. Particularly, it is because in weak scintillation the atmospheric turbulence does not convert symmetric states into antisymmetric states. Since the HOM dip is produced by the antisymmetric states, it follows that in their absence the HOM remains robust.

While our analyses are based on LG modes, in deriving the results of Sec. 4.3 we ignore the radial index and only consider the azimuthal degree of freedom. It is this undertaking that led to the simplicity of the results thus obtained. Nonetheless, we acknowledge that in the most general case, the individual Bell states, which are defined in terms of LG modes, can also have an additional summation over all the different radial (p) indices. If the LG modes are the Schmidt basis for the SPDC state, then these summations over the radial index would break up into individual Bell states in which the radial indices appear in the same way as the azimuthal indices. One would then be able to select a particular set of radial indices just like we selected a particular set of azimuthal indices and follow the argument through, as presented in Sec. 4.3. As a result the radial index would not affect the argument. Unfortunately, the LG states are not the exact Schmidt basis for the SPDC process [145]. However, one can argue that the actual Schmidt basis is not significantly different from the LG modes; under the Gaussian approximation of the phase-matching function [142], the Schmidt basis does turn out to be the LG modes [146]. As a result we don't expect the radial index to play a significant role in the analysis of Sec. 4.3.

The analyses that are reported here are restricted to the domain of weak scintillation. It may therefore seem to be an artefact of the single phase screen approximation that bestows this property on turbulence that it does not convert symmetric states into antisymmetric states.

In the theoretical results, to alleviate the calculations, we used instead of the Kolmogorov structure function the quadratic structure function. The quadratic structure function is an approximation to the Kolmogorov structure function. This may therefore contribute towards the deviation of the theoretical results from the experimental results. However, from the consistency between the two sets of results as shown in Fig. 4.6, we conclude that this contribution may not be significant.

4.7 Summary

Two analyses were provided, one for the one-sided turbulence channel and one for the two-sided turbulence channel. The former was simpler because it exploited the orthogonality of the modal basis to simplify the analysis. The latter was more involved and required a more thorough calculation. The analysis for the one-sided case clearly demonstrates that the HOM interference effect is not affected by one-sided weak scintillation. The more detailed analysis for the two-sided case showed that, although not completely unaffected, the HOM interference effect is only slightly affected by the scintillation.

In the experiment, the input state of the photon pair was prepared with spontaneous parametric down-conversion (SPDC). The turbulence was simulated by random phase modulations with the aid of phase-only spatial light modulators (SLMs). As such, the turbulence was represented by a single phase screen, which is valid for weak scintillation conditions. This implies that we did not consider the conditions associated with strong scintillation. The random phase modulations on the SLMs were computed according to the Kolmogorov theory of turbulence. However, for tractability, a quadratic structure function approximation was used in the calculations. The HOM interference was obtained with the aid of a balanced (50:50) beam splitter; the HOM filter. The SPDC process naturally produces a symmetric state, which leads to a lack of coincidence counts (a HOM dip) on the detection system after the HOM filter. We measured the influence of turbulence by assessing the visibility of the HOM dip. The photons after the HOM filter were observed with the aid of additional SLMs in the Laguerre-Gauss (LG) basis with opposite signs for the azimuthal indices at the two output ports. The Schmidt basis of the biphoton state after the turbulence is known to be an OAM basis.

With this it has been shown, both theoretically and experimentally that the HOM interference is not affected by one-sided turbulence under weak scintillation conditions. It has also been shown that the effect of turbulence for a two-sided channel remains small under weak scintillation conditions.

The results of this work show that free-space implementation of long distance quantum communication using quantum repeaters is viable, and may be able to succeed. This conclusion also holds for other applications which depend on the HOM, including the remote clock synchronization protocols.

Chapter 5

High-dimensional quantum channel estimation using classical light

5.1 Introduction

The orbital angular momentum (OAM) degree of freedom spans an infinite dimensional Hilbert space and can lead to the practical realization of high-dimensional quantum digits. This is in contrast to the polarization degree of freedom which allows for the generation of two-dimensional quantum digits.

In the previous chapters, we have only assessed and discussed atmospheric turbulence from the perspective of how it affects optical fields. This is an important aspect of the successful implementation of free-space quantum and optical communication systems. For instance, some of the quantum communication protocols [19] are based on quantum entanglement. As has been studied [77, 72, 75, 78, 80, 81, 147, 82, 79], propagation through the atmosphere leads to a distortion of the optical fields and a degradation of quantum entanglement. This implies that the success of a free-space communication system requires an active correction system.

In light of the requirement for a correction system, a recent study has proposed a method to characterize a quantum channel using classical light [103]. In the study, it is shown that the evolution of two classically entangled degrees of freedom and two quantum entangled degrees of freedom is in a one-to-one correspondence in the case where the channel for both systems acts on only one degree of freedom. Therefore, they show, using vector beams, that classical light could be used to obtain information about a quantum channel.

In this chapter, we propose a method to characterize a high-dimensional quantum channel with the aid of classical light. The work we present here is a generalization of the method for classical characterization (using polarization) [103] of quantum channels to higher dimensions. The work which was done by Ndagano *et al.* [103] was based on a qubit system. This is because they used vector beams as their non-separable state to characterize the channel. This implies that their method has the limitation of dimension since it is based on polarization. They can only work with two dimensional states.

Our method uses a single non-separable input optical field that has correlations between the spatial (OAM) modes and the wavelength degrees of freedom to determine the effect of the channel on the OAM modes. The wavelength degree of freedom is used here, instead of polarization, to facilitate the generalization to high-dimensions. The channel estimation process incorporates spontaneous parametric up-conversion (SPUC) also known as sum frequency generation (SFG) to perform the pertinent measurements.

The work presented in this chapter has been published [148].

The chapter is organized as follows: Section 5.2 provides a heuristic discussion about the principle and how this scheme works. In Sec. 5.3 we focus on the SFG process and perform a detailed calculation to show that the scheme does indeed work. Finally, in Sec. 5.4 we present a brief discussion and our conclusions.

5.2 Classical estimation of a quantum channel

5.2.1 Principle

To estimate the quantum channel with the use of classical light, we use a general approach and assume that we can use two different degrees of freedom of light, wherein only one of them is affected by the channel. We also assume that the channel maintains the purity of any quantum state that propagates through it. We further prepare an input state (optical field) that contains correlations between these different degrees of freedom. Although a classical optical field, the input field is represented here in terms of the Dirac ket notation

$$|\psi_{\text{in}}\rangle = \sum_n |A_n\rangle|B_n\rangle\alpha_n, \tag{5.1}$$

where A_n and B_n represent two different degrees of freedom denoted by separate kets, the n indicates the different basis elements in these degrees of freedom and α_n denotes the expansion coefficients, such that $\sum_n |\alpha_n|^2 = 1$. The expansion coefficients are complex and when squared they represent the probability of occurrence of the n^{th} basis elements. Hence, it is required that the sum of all the squares be equal to unity.

It is assumed that the channel only affects the B degree of freedom. The output after the channel is obtained by replacing each $|B_n\rangle$ in terms of a superposition of several of them to represent the scattering process. The number of such kets that form the superposition is determined by the intensity of the scattering process.

In order to determine the channel, we perform a tomography on the system. The tomography is done by way of projective measurements on both degrees of freedom. This is done in terms of the basis given by the original kets and in terms of a mutually unbiased basis with respect to these original kets. Classical light has the advantage of brightness and thus we do not have to perform the projective measurements sequentially, rather we can divide the output into separate channels where all the different measurements are performed simultaneously. Through these measurements, we can then determine the complex coefficients of the kets that are in the output state. Given these coefficients, we can further proceed to determine the channel matrix since it is in these complex coefficients that the information about the channel is contained.

In the rest of this chapter, the B degree of freedom denotes the spatial modes, particularly the (OAM) modes. The A degree of freedom denotes the wavelength (frequency), which is not affected by turbulence. Given these assignments, we can re-express the input state in Eq. (5.1) as follows

$$|\psi_{\text{in}}\rangle = \sum_n |\lambda_n\rangle|\ell_n\rangle\alpha_n, \tag{5.2}$$

where λ_n represents the different wavelengths and ℓ_n is the azimuthal index of different OAM modes, and α_n still represents the complex expansion coefficients.

We consider a free-space channel that represents the effects of the atmospheric turbulence on the OAM modes. The atmospheric turbulence, which is represented by a Kraus operator $\hat{\Lambda}$, would scatter the OAM modes to other OAM modes

$$\hat{\Lambda}|\ell_n\rangle = \sum_m |\ell_m\rangle\Lambda_{mn}. \tag{5.3}$$

As a consequence of the scattering process, the output state will contain new (additional) kets that lead to a different superposition from that of the input state. In tensor representation, we will denote the channel Kraus operator as Λ_{mn}. It is the purpose of this scheme to determine the matrix Λ_{mn} and to measure the values of its matrix elements. The distortion correction involves the design of another matrix that would compensate for the distortion caused by the Kraus operator. After going through the channel we obtain

$$\begin{aligned} |\psi_{\text{out}}\rangle = \hat{\Lambda}\otimes\mathbb{1}|\psi_{\text{in}}\rangle &= \sum_n |\lambda_n\rangle\hat{\Lambda}|\ell_n\rangle\alpha_n \\ &= \sum_{mn} |\lambda_n\rangle|\ell_m\rangle\Lambda_{mn}\alpha_n, \end{aligned} \tag{5.4}$$

where $\mathbb{1}$ is the identity operator on the wavelength degree of freedom. Since the indices of Λ_{mn} are respectively contracted on the basis elements of the different degrees of freedom, a clever selection of measurements can uncover all the information about Λ_{mn}. That is, all magnitudes and phases except an overall phase. In spite of the overall phase issue[1], the information obtained in this way is sufficient to characterize the channel.

It is common in optical experiments to use polarization as a degree of freedom. If this were the case for the unaffected degree of freedom, the measurements would be trivial to perform by use of polarization optics. For instance, projective measurements could be performed on the perturbed state by using half and quarter wave-plates. In the work done by Ndagano *et al.* [103], vector beams were used as the model state for the classical non-separability. Their input state consisted of the OAM degree of freedom and the polarization degree of freedom. The latter was the one that was resilient against atmospheric turbulence. Therefore, within their scheme, they were able to perform the projective measurements using polarization optics.

[1] In a tomographic reconstruction, we determine the density matrix of the system of interest. The elements of the density matrix (pure state) appear as products of the basis expansion coefficients. Therefore, in determining these elements we only determine the relative phases between them, not the absolute phase.

In this work, we use the wavelength degree of freedom instead of polarization. Hence, we propose the use of SFG for the projective measurements. The measurements are made by preparing optical fields, which we call the measurement states, in terms of combinations of the different bases for the different degrees of freedom. These measurement states are sent through a nonlinear crystal, together with the output field to perform the upconversion.

The main issues concerned with the implementation of this method are: (a) the preparation of the input state; (b) the preparation of the measurement states; and (c) the measurement process itself. We will start by discussing the preparation of the input state.

5.2.2 Input state preparation

Our scheme is based on an input state that is nonseparable in terms of the wavelength degree of freedom and the OAM degree of freedom. Here, we give the details of the procedure that is to be followed in preparing such an input state. The preparation would start with a light beam that consists of several discrete frequencies. Such a light beam is well represented by a frequency comb laser beam [149]. The frequency comb laser beam consists of a sequence of laser pulses that occur at a rate given by the pulse repetition frequency. The spectral components of the frequency comb are separated by the pulse repetition frequency, which is typically on the order of a 100 MHz to a few GHz.

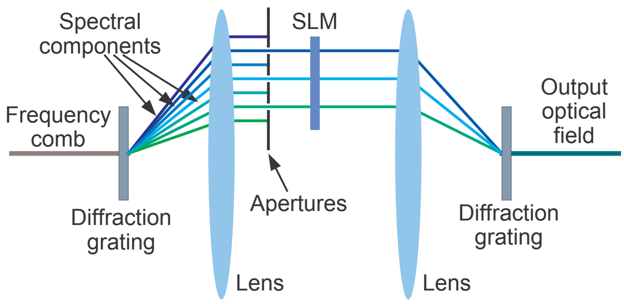

FIGURE 5.1: Optical setup used to prepare the input optical field.

The proposed setup to prepare the input optical field is shown in Fig. 5.1. One can use a diffraction grating to separate the different spectral components of the frequency comb. Using some apertures, one can, therefore, select out specific components. In our scheme, we select components that are separated by twice the pulse repetition frequency. The reason for this is explained below when we discuss the preparation of the measurement states. Having dispersed the different spectral components, we would further apply a 2-f setup using a lens to redirect the selected components side by side on a spatial light modulator (SLM). Upon incidence on the SLM, each of the spectral components is modulated with a specific OAM mode, thus associating to each spectral component a specific spatial distribution.

At this point, we have successfully generated different light beams that are monochromatic such that associated with each frequency is a different spatial distribution. However, we have not generated the input state in Eq. (5.2). The input state in the latter equation is enforced by recombining the spectral components using yet another 2-f system. Using a diffraction grating, the optical beams can be recombined into the nonseparable input state described in Eq. (5.2).

The resulting beam now contains correlations between spectral components and the azimuthal indices. In contrast to the vector modes that are used in other schemes, for example [103], the current method has no fundamental limitation in the dimensionality of the Hilbert space. Apart from practical limitations such as the size of the SLM, this approach can be used to generate states that are nonseparable in an arbitrary number of dimensions.

The input optical field is sent through the channel to produce the output field, as represented in Eq. (5.4). The Kraus operator only acts on the spatial degrees of freedom and not on the frequency or wavelength degrees of freedom. As a result, the OAM modes are scattered into other OAM modes. Based on the construction of the input state, the output state now contains information about the Kraus operator of the channel. Appropriate measurements on the output state can now uncover the Kraus operator. The measurement process, which employs SPUC, is explained next.

5.2.3 Upconversion measurements

As already alluded to in the case of polarization as a degree of freedom, polarization optics can be used to perform the necessary projective measurements. However, in our scheme, we propose to use wavelength as a degree of freedom. Therefore, we use the SPUC process to implement the measurement scheme. The inspiration for this proposal comes from a thorough study of the spontaneous parametric down-conversion (SPDC) process, which is discussed in Chapter 2. In an SPDC process, an input pump beam incident on a nonlinear crystal, usually a β-Barium Borate (BBO), leads to a generation of a pair of photons with frequencies that add up to the pump beam frequency due to energy conservation. Since the SPDC conserves both energy and momentum, it is able to create entanglement in the respective degrees of freedom. Furthermore, it has been shown both theoretically and experimentally that under general conditions SPDC conserves OAM [63].

For an input pump beam that is described by a Gaussian profile, the output beam after the SPDC process can be expressed as

$$|\Psi_{\text{SPDC}}\rangle = \sum_{\ell} \int |\ell, \omega\rangle_s |\bar{\ell}, \omega_p - \omega\rangle_i \Pi(\omega; |\ell|)\, \mathrm{d}\omega, \tag{5.5}$$

where ω_p is the angular frequency of the pump, ℓ represents the azimuthal index, with $\bar{\ell} = -\ell$, the subscripts s and i denote the signal and idler photons, respectively, and $\Pi(\omega; |\ell|)$ is a coefficient function. It can be seen from the kets that the sum of the azimuthal indices gives zero, which is consistent with the input pump beam profile. Likewise, the sum of the frequencies adds up to ω_p which is the pump beam frequency.

Ideally, one would like the coefficient function to be constant over a range of azimuthal indices and frequencies. If the frequencies are selected to be relatively close to each other, which is made possible by using a frequency comb, one may assume that the coefficient function is independent of frequency over that range. However, it would, in general, depend on the magnitudes of the azimuthal indices, especially for the high-dimensional case. Based on this understanding, we'll assume that one can replace $\Pi(\omega; |\ell|) \to \Pi(|\ell|)$.

The upconversion process is given by the dual of the down-converted state $\langle\Psi_{\text{SPUC}}| = (|\Psi_{\text{SPDC}}\rangle)^{\dagger}$, provided that the output that is measured after the upconversion is a photon with a Gaussian profile analogous to that of the pump beam in the down-conversion process. The tomography measurements are then given by

$$M_{\text{mea}} = \langle \Psi_{\text{SPUC}} | \psi_{\text{out}}, \psi_{\text{mea}} \rangle, \tag{5.6}$$

where $|\psi_{\text{mea}}\rangle$ is the measurement state and $|\psi_{\text{out}}\rangle$ is the output state after the channel, given in Eq. (5.4). The probability for a successful upconversion (detection of an upconverted photon) is given by $P_{\text{up}} = |M_{\text{mea}}|^2$. We'll assume the measurement state corresponds to the signal and the output state to the idler, as defined in Eq. (5.5).

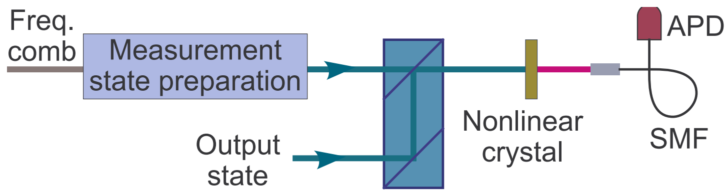

FIGURE 5.2: Diagrammatic representation of the measurement process.

One way to look at this process is to consider the effective state with which the output state is overlapped. Such a state is given by the overlap of the measurement state with the SPUC process

$$\langle \psi_{\text{eff}} | = \langle \Psi_{\text{SPUC}} | \psi_{\text{mea}} \rangle. \tag{5.7}$$

Consider, for example, the case where the measurement state contains superpositions in both the degrees of freedom

$$|\psi_{\text{mea}}\rangle = (|\ell_1\rangle a + |\ell_2\rangle b) \left(|\omega_1\rangle c + |\omega_2\rangle d \right), \tag{5.8}$$

where a, b, c and d are complex coefficients. The effective state then becomes

$$\begin{aligned} \langle \psi_{\text{eff}} | &= [\Pi(|\ell_1|) a \langle \bar{\ell}_1 | + \Pi(|\ell_2|) b \langle \bar{\ell}_2 |] \\ &\quad \times \left(\langle \omega_p - \omega_1 | c + \langle \omega_p - \omega_2 | d \right). \end{aligned} \tag{5.9}$$

One can choose the values of a and b to compensate for the difference in magnitude between $\Pi(|\ell_1|)$ and $\Pi(|\ell_2|)$. The final measurement is then given by

$$M_{\text{mea}} = |\langle \psi_{\text{eff}} | \psi_{\text{out}} \rangle|^2 . \tag{5.10}$$

We see that $\langle \psi_{\text{eff}}|$ is the dual of a specific state that would be selected by inner product from the output state. Since one can design the measurement state $|\psi_{\text{mea}}\rangle$, one has control over $\langle \psi_{\text{eff}}|$.

Using the proposed setup in Fig. 5.2, the necessary measurements can be performed. The output state after the channel is optically combined with a measurement state that is specifically prepared for each measurement. The preparation of the measurement states is discussed in more detail below. The combined beam is then sent through a nonlinear crystal to perform upconversion. The output after the upconversion process is coupled into a single mode optical fiber, which selects out the Gaussian beam profile. The photons that are coupled into the fiber are detected with a single photon detector, such as an avalanche photodiode.

5.2.4 Tomography

A judicious set of measurements can be performed on the output state that is given in Eq. (5.4) to determine the matrix elements of the Kraus operator (Channel matrix) [3]. In the remainder of this discussion, we ignore the complex coefficients α_n under the assumption that one can make these values all equal in the preparation of the input state. The output state is written as follows

$$|\psi_{\text{out}}\rangle = \sum_{mn} |\ell_m\rangle|\omega_n\rangle\Lambda_{mn}, \tag{5.11}$$

where we converted wavelength into angular frequency.

The magnitude of the individual elements of the channel matrix can be determined by using a measurement state with a single frequency and a single OAM mode

$$|\psi_{\text{mea}}\rangle = |\bar{\ell}_u\rangle|\omega_p - \omega_v\rangle, \tag{5.12}$$

where the subscripts u and v represent specific components, leads to

$$\langle\psi_{\text{eff}}| = \langle\ell_u|\langle\omega_v|. \tag{5.13}$$

The projective measurement then gives

$$\begin{aligned} |\langle\ell_u,\omega_v|\psi_{\text{out}}\rangle|^2 &= \left|\sum_{mn}\langle\ell_u,\omega_v|\ell_m,\omega_n\rangle\Lambda_{mn}\right|^2 \\ &= |\Lambda_{uv}|^2 . \end{aligned} \tag{5.14}$$

Since the channel matrix elements are complex, it is still left to determine the phases of the individual elements. However, it is only possible to determine the relative phase since there is an overall phase that the measurements cannot uncover. To obtain the relative phases of the elements, one needs to produce superpositions of the frequencies and/or OAM modes. If, for instance, the measurement state contains a superposition of two frequencies

$$|\psi_{\text{mea}}\rangle = |\bar{\ell}_u\rangle\left(|\omega_p - \omega_v\rangle + |\omega_p - \omega_w\rangle\right)\frac{1}{\sqrt{2}}, \tag{5.15}$$

where the subscripts u, v and w represent specific components, we get

$$\langle\psi_{\text{eff}}| = \langle\ell_u|\left(\langle\omega_v| + \langle\omega_w|\right)\frac{1}{\sqrt{2}}. \tag{5.16}$$

In this case, the projective measurement produces an interference term

$$\begin{aligned} |\langle\psi_{\text{eff}}|\psi_{\text{out}}\rangle|^2 &= \frac{1}{2}|\langle\ell_u,\omega_v|\psi_{\text{out}}\rangle + \langle\ell_u,\omega_w|\psi_{\text{out}}\rangle|^2 \\ &= \frac{1}{2}|\Lambda_{uv} + \Lambda_{uw}|^2 \\ &= \frac{1}{2}\left(|\Lambda_{uv}|^2 + |\Lambda_{uw}|^2 + \Lambda_{uv}^*\Lambda_{uw} + \Lambda_{uv}\Lambda_{uw}^*\right), \end{aligned} \tag{5.17}$$

which can be used to obtain the relative phase of the elements. The interference term in the above equation, however, is only one part of the process that is required to obtain the phase of the elements. It only gives the $\cos\theta_{uwv}$ contribution, where θ_{uwv} is the phase between the elements Λ_{uv} and Λ_{uw}. The $\sin\theta_{uwv}$ component which completes the process is obtained by using a measurement state that contains the same elements with a phase shift of $\pi/2$

$$|\psi_{\text{mea}}\rangle = |\bar{\ell}_u\rangle \left(|\omega_p - \omega_v\rangle + \mathrm{i}|\omega_p - \omega_w\rangle\right) \frac{1}{\sqrt{2}}, \tag{5.18}$$

which therefore leads to the measurement result

$$|\langle\psi_{\text{eff}}|\psi_{\text{out}}\rangle|^2 \quad = \quad \frac{1}{2}\left(|\Lambda_{uv}|^2 + |\Lambda_{uw}|^2 + \mathrm{i}\Lambda_{uv}^*\Lambda_{uw} - \mathrm{i}\Lambda_{uv}\Lambda_{uw}^*\right). \tag{5.19}$$

These two measurement results can finally be combined to generate the relative phase between the said elements. This completes the measurement of the complex elements of the Kraus operator. This process is repeated until all the required measurements have been performed.

5.2.5 Measurement state preparation

The advent of SLMs has made the generation of OAM modes to be trivial. OAM modes and their superpositions can be readily generated using the SLMs through the computer generated hologram method discussed in Chapter 2.

The superposition of frequencies, as would be required by our scheme for the measurement states, can be performed by using amplitude modulation with a suppressed carrier. The modulation frequencies need to be on the order of the pulse repetition frequency of the frequency comb. Currently, electro-optical modulators and acousto-optical modulators can perform modulation of optical signals into the GHz range. The modulation processes for two different cases are shown in Fig. 5.3. Remember that the spectral components that are used in the preparation of the input state are separated by twice the pulse repetition frequency. Therefore, by modulating with the repetition frequency we are able to generate the sidebands that correspond to the frequency elements shown in Fig. 5.3 (a).

If the two components in the superposition lie next to each other, separated by twice the pulse repetition frequency, one would select a component between these two components and modulate it by the pulse repetition frequency, as shown in Fig. 5.3 (a). This would be made possible by the way we would have chosen spectral component for the preparation of the input state.

On the other hand, if the spectral components of the superposition are further apart (say four times the pulse repetition frequency) we select a spectral component halfway between the two required components and modulate it by two times the pulse repetition frequency, as shown in Fig. 5.3 (b). This process would produce sidebands by adding and subtracting to the selected frequency twice the repetition frequency thus leading to the generation of the frequencies as depicted in Fig. 5.3 (b).

As a generic representation of amplitude modulation, let us consider a carrier signal that is represented by

$$f(t) = \sin(\omega_c t), \tag{5.20}$$

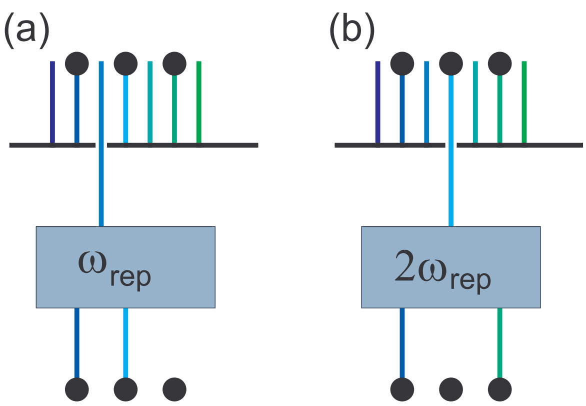

FIGURE 5.3: Diagrammatic representation of modulation process, using (a) pulse repetition frequency and (b) twice pulse repetition frequency. The black dots denote those spectral components that are chosen as part of the input state.

where ω_c is the carrier signal frequency. We note that the use of the word "signal" here is not associated with the signal of the SPDC, it is the jargon used in electrical engineering and communication engineering. Given the carrier signal, as it is also usually done in communication engineering applications, we consider a second signal that will represent the modulating function

$$g(t) = \sin(\omega_m t), \tag{5.21}$$

where ω_c is the modulation signal frequency.

Amplitude modulation is achieved by multiplying the two signals as follows

$$\begin{aligned} h(t) &= f(t)g(t) \\ &= \sin(\omega_c t)\sin(\omega_m t), \end{aligned} \tag{5.22}$$

which after using the identity

$$\sin A \sin B = \frac{1}{2}\left[\cos(A-B) - \cos(A+B)\right] \tag{5.23}$$

becomes

$$\begin{aligned} h(t) &= f(t)g(t) \\ &= \frac{1}{2}\left[\cos(\omega_c - \omega_m) - \cos(\omega_c + \omega_m)\right]. \end{aligned} \tag{5.24}$$

The above result[2] shows that amplitude modulation of some input function leads to the generation of two frequency components that are represented by the sum and difference frequencies that are involved. In our scheme, we consider the modulation frequency as the pulse repetition (or multiples) frequency of the frequency comb laser, and we consider the carrier signal frequency as the frequency component that we modulate with the pulse repetition frequency.

[2]Here, we show the amplitude modulation as a way of illustration. Therefore, we also ignore some constants that may be associated with the functions f and g.

The relative phase between the two components in the superposition is determined by the phase of the modulation signal. Since multiple measurements with different relative phases need to be made simultaneously, it is necessary to maintain coherence among the different modulation signals in the different measurements.

After the temporal modulation, which produces the required superposition in frequency components, the beam is spatially modulated with an SLM to obtain the spatial profile for the measurement state. This is done by producing a superposition of the spatial mode on the SLM. Depending on the required accuracy of the measurement, the fidelity of the spatial mode can be improved with the aid of complex amplitude modulation [150]. Note that the measurement state does not have correlations between the bases elements of the different degrees of freedom, as one has for the input state; the measurement states are separable states in terms of these degrees of freedom.

5.2.6 Complete process

Our scheme consists of different building blocks that can be put together to obtain an overall process that can be summarized as shown in Fig. 5.4. The process commences with the preparation of the input state in a series of steps as can be seen in Fig. 5.1. Having prepared the input state, it is further sent through the channel. The output state is divided by an array of beam splitters. This allows all the different measurements to be made simultaneously. Each measurement is made with a setup as shown in Fig. 5.2 and it incorporates the preparation of a measurement state that may require a temporal modulation, as shown in Fig. 5.3.

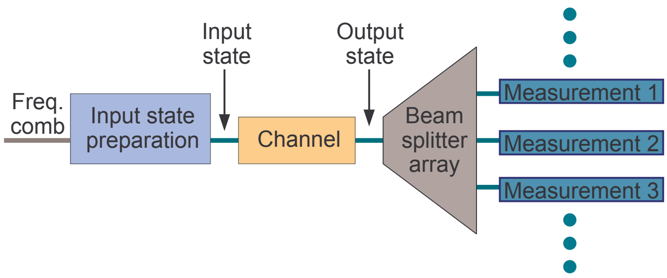

FIGURE 5.4: Diagrammatic representation of the complete channel estimation process.

The information that is obtained from the different measurements is used to reconstruct the Kraus matrix. This is further used to produce a matrix that will compensate for the distortions caused by the channel (Kraus operator).

What remains to be done is to consider the upconversion process in more detail to confirm the process represented in Eqs. (5.6)-(5.9). In addition, we need to consider the nature of the coefficient function $\Pi(|\ell|)$ so that we can understand its effect in Eq. (5.9). For these purposes, we perform a more detailed calculation next.

5.3 Explicit calculation of the upconversion process

Here, we provide a detailed calculation of the upconversion process to show that it does produce the required measurements. This calculation also reveals the nature of the coefficient function $\Pi(|\ell|)$ that appears in Eq. (5.5). The calculation can be expressed as an integral representation of Eq. (5.6):

$$M_{\text{mea}} = \int \Psi_{\text{SPUC}}(\mathbf{a}_1, \mathbf{a}_2)\psi_{\text{out}}(\mathbf{a}_1)\psi_{\text{mea}}(\mathbf{a}_2)\ \mathrm{d}a_1^2\ \mathrm{d}a_2^2, \tag{5.25}$$

where $\mathbf{a}_1$ and $\mathbf{a}_2$ are two-dimensional spatial frequency vectors associated with the output state and the measurement state, respectively.

To perform the calculation in Eq. (5.25) as effectively as possible, we employ some careful considerations and make a few simplifying assumptions. Firstly, we assume that the turbulence in the channel only causes weak scintillation. Under such conditions, the scintillation process can be described by a single phase screen. In turn, this implies that the result is independent of the propagation distance; the propagation has no effect. In the calculation, the wavelengths are determined by those in $\Psi_{\text{SPUC}}(\mathbf{a}_1, \mathbf{a}_2)$.

The SPUC-function $\Psi_{\text{SPUC}}(\mathbf{a}_1, \mathbf{a}_2)$ serves as a kernel function in Eq. (5.25). It is composed of the product of the phase matching function $S(\mathbf{a}_1, \mathbf{a}_2)$ and the mode that couples into the single mode fiber $g(\mathbf{a}_3)$, where $\mathbf{a}_3$ is the spatial frequency of the upconverted photon. The transverse phase matching conditions replace $\mathbf{a}_3$ with a linear combination of the spatial frequencies $\mathbf{a}_1$ and $\mathbf{a}_2$. As a result, the kernel function for the upconversion process has the form

$$\Psi_{\text{SPUC}}(\mathbf{a}_1, \mathbf{a}_2) = g(\mathbf{a}_1, \mathbf{a}_2)S(\mathbf{a}_1, \mathbf{a}_2). \tag{5.26}$$

The phase matching function is a sinc-function, which one can approximate with a Gaussian function in the limit where the crystal is much shorter than the Rayleigh range of the coupled mode (the thin crystal limit). Hence,

$$\begin{aligned} S(\mathbf{a}_1, \mathbf{a}_2) &= \operatorname{sinc}\left[\frac{L}{2}\Delta k_z(\mathbf{a}_1, \mathbf{a}_2)\right] \\ &\approx \exp\left[-\frac{L}{2}\Delta k_z(\mathbf{a}_1, \mathbf{a}_2)\right], \end{aligned} \tag{5.27}$$

where $\Delta k_z(\mathbf{a}_1, \mathbf{a}_2)$ is the mismatch in the longitudinal components of the propagation vectors. To obtain an expression for the mismatch given above, we first consider that any deviation from momentum conservation in SPDC can be expressed in terms of the three-dimensional propagation vectors $\mathbf{k}$ as

$$\Delta\mathbf{k}(\mathbf{a}_1, \mathbf{a}_2) = n_1\mathbf{k}_1 + n_2\mathbf{k}_2 - n_3\mathbf{k}_3, \tag{5.28}$$

where the subscripts $1, 2, 3$ refer to the signal, idler and pump beams, respectively. The refractive indices n_1, n_2 and n_3 depend on the frequencies and states of polarization of their associated optical beams.

For critical phase matching, the dominant part of Eq. (5.28) becomes zero. As a result, if we assume collinear conditions and replace the three propagation vectors by their magnitudes, we obtain a relationship among the refractive indices and wavelengths

$$0 = \frac{n_1}{\lambda_1} + \frac{n_2}{\lambda_2} - \frac{n_3}{\lambda_3}. \tag{5.29}$$

Energy conservation, $\omega_3 = \omega_1 + \omega_2$, provides us with another relationship among the three wavelengths given as

$$\lambda_3 = \frac{\lambda_1 \lambda_2}{\lambda_1 + \lambda_2}. \tag{5.30}$$

Using Eqs. (5.29) and (5.30), one can obtain an expression for n_3 given by

$$n_3 = \frac{n_1 \lambda_2 + n_2 \lambda_1}{\lambda_1 + \lambda_2}. \tag{5.31}$$

The transverse part of the mismatch given in Eq. (5.28) is zero $\Delta \mathbf{k}_\perp = 0$. This is because one can extend the transverse spatial integrations to infinity, provided that the pump beam does not overfill the nonlinear crystal. Here, the subscript $\perp$ represents the transverse part. The transverse components of the pump beam can be replaced by

$$\mathbf{a}_3 = \frac{n_1 \mathbf{a}_1 + n_2 \mathbf{a}_2}{n_3} = \frac{(n_1 \mathbf{a}_1 + n_2 \mathbf{a}_2)(\lambda_1 + \lambda_2)}{n_1 \lambda_2 + n_2 \lambda_1}, \tag{5.32}$$

where we express the transverse parts of the propagation vectors in terms of two-dimensional spatial frequency vectors, related by $2\pi \mathbf{a} = \mathbf{k}_\perp$.

Due to the finite length of the nonlinear crystal, the longitudinal components do not cancel exactly

$$\Delta k_z = n_1 k_{1z} + n_2 k_{2z} - n_3 k_{3z}. \tag{5.33}$$

One can express the longitudinal components of the propagation vectors in terms of the transverse spatial frequency vectors

$$k_{mz} = 2\pi \left(\frac{1}{\lambda_m^2} - |\mathbf{a}_m|^2 \right)^{1/2}, \tag{5.34}$$

where $m = 1, 2, 3$. Substituting these expressions into Eq. (5.33), performing a paraxial expansion and applying Eqs. (5.30) and (5.31), we then obtain (ignoring an overall minus sign)

$$\Delta k_z(\mathbf{a}_1, \mathbf{a}_2) = \frac{\pi n_1 n_2 |\lambda_1 \mathbf{a}_1 - \lambda_2 \mathbf{a}_2|^2}{n_1 \lambda_2 + n_2 \lambda_1}. \tag{5.35}$$

Combining all the above, we obtain an expression for the SPUC kernel-function given by

$$\begin{aligned} \Psi_{\text{SPUC}}(\mathbf{a}_1, \mathbf{a}_2) \quad = \quad & \Omega(\lambda_1, \lambda_2) \exp \left[-\frac{\pi^2 w_c^2}{n_3^2} |n_1 \mathbf{a}_1 + n_2 \mathbf{a}_2|^2 \right. \\ & \left. - \frac{\pi n_1 n_2 L |\lambda_1 \mathbf{a}_1 - \lambda_2 \mathbf{a}_2|^2}{2(\lambda_1 n_2 + \lambda_2 n_1)} \right], \end{aligned} \tag{5.36}$$

where w_c is the size of the Gaussian mode that couples into the fiber, Ω is an overall constant that may depend on the wavelengths. Since we are not interested in the global magnitude of the process, as it will cancel out in normalization, we will henceforth ignore Ω.

Both the output state and the measurement state can be expressed as superpositions of LG modes. The point of this exercise is to show that the three-way overlap, given in Eq. (5.25), serves as an inner product for these LG modes because this allows the extraction of the coefficients in the expansion from which the information of the Kraus operator is obtained. For this purpose, it suffices to select individual LG modes for the output state and the measurement state. In the calculation, we use the generating function for the angular spectra of the LG modes [90] with zero radial index ($p = 0$)

$$\mathcal{G}_{\mathrm{LG}}(\mathbf{a};\mu,T,w) = \mathcal{N}\exp\left[\mathrm{i}\pi(a+\mathrm{i}Tb)w\mu - \pi^2 w^2|\mathbf{a}|^2\right], \tag{5.37}$$

where w is the mode size, T is given by the sign of the azimuthal index, μ is the generating parameter and

$$\mathcal{N} = w\left(\frac{2\pi 2^{|\ell|}}{|\ell|!}\right)^{1/2}, \tag{5.38}$$

is the normalization constant, which depends on the azimuthal index. The angular spectrum for a particular LG mode is produced by taking the number of derivatives, with respect to the generating parameter equal to the magnitude of the azimuthal index and setting the generating parameter to zero, where after we substitute in the appropriate normalization constant.

One can now substitute Eq. (5.36) and

$$\begin{aligned} \psi_{\mathrm{out}}(\mathbf{a}_1) &\rightarrow \mathcal{G}_{\mathrm{LG}}(\mathbf{a}_1;\mu_1,T_1,w_1) \\ \psi_{\mathrm{mea}}(\mathbf{a}_2) &\rightarrow \mathcal{G}_{\mathrm{LG}}(\mathbf{a}_2;\mu_2,T_2,w_2), \end{aligned} \tag{5.39}$$

into Eq. (5.25) to obtain the generating function for the measurements M_{mea}

$$\begin{aligned} \mathcal{G} = & \int \exp\left[-\frac{\pi^2 w_c^2}{n_3^2}|n_1\mathbf{a}_1 + n_2\mathbf{a}_2|^2 - \frac{\pi n_1 n_2 L|\lambda_1\mathbf{a}_1 - \lambda_2\mathbf{a}_2|^2}{2(\lambda_1 n_2 + \lambda_2 n_1)}\right. \\ & + \mathrm{i}\pi(a_1 + \mathrm{i}T_1 b_1)w_1\mu_1 - \pi^2 w_1^2|\mathbf{a}_1|^2 + \mathrm{i}\pi(a_2 + \mathrm{i}T_2 b_2)w_2\mu_2 \\ & \left. -\pi^2 w_2^2|\mathbf{a}_2|^2\right] \mathrm{d}a_1^2\,\mathrm{d}a_2^2. \end{aligned} \tag{5.40}$$

However, in this form it is not really useful. Therefore, we proceed by evaluating all the spatial frequency integrals to obtain

$$\begin{aligned} \mathcal{G} = & \frac{\pi w_1 w_2 \mathcal{N}_1\mathcal{N}_2 n_3^2}{\mathcal{A}_0} \\ & \times \exp\left[\frac{w_c^2\mu_1\mu_2 n_1 n_2 w_1 w_2 \mathcal{A}_1(T_1T_2 - 1)\lambda_2\lambda_1}{4\lambda_1^2\lambda_2 n_2^3 w_1^2 w_c^2 + 4\lambda_1^2\lambda_2 n_2 n_3^2 w_1^2 w_2^2 + \mathcal{A}_2 n_1^3 + \mathcal{A}_3 n_1^2 + \mathcal{A}_4 n1}\right], \end{aligned} \tag{5.41}$$

where

$$\begin{aligned}
\mathcal{A}_0 &= n_1^2 w_2^2 w_c^2 + n_2^2 w_1^2 w_c^2 + n_3^2 w_1^2 w_2^2 \\
\mathcal{A}_1 &= \beta\lambda_1 n_3^2 + \beta\lambda_2 n_3^2 - 2\lambda_1 n_2 - 2\lambda_2 n_1 \\
\mathcal{A}_2 &= \frac{2\beta\lambda_1\lambda_2^3 w_c^4 n_2}{\lambda_3} + 4\lambda_1\lambda_2^2 w_2^2 w_c^2 \\
\mathcal{A}_3 &= \frac{4\beta\lambda_1^2\lambda_2^2 w_c^4 n_2^2}{\lambda_3} + 4\lambda_1^2\lambda_2 w_2^2 w_c^2 n_2 \\
\mathcal{A}_4 &= \frac{2\beta\lambda_1\lambda_2 w_c n_2\left[\lambda_1^2 w_c^2 n_2^2 + n_3^2(\lambda_1^2 w_2^2 + \lambda_2^2 w_1^2)\right]}{\lambda_3} + 4\lambda_1\lambda_2^2 w_1^2 w_c^2 n_2^2 + 4\lambda_1\lambda_2^2 n_3^2 w_1^2 w_2^2,
\end{aligned}$$

and

$$\beta = \frac{L\lambda_1\lambda_2}{\pi w_c^2(\lambda_1+\lambda_2)}. \tag{5.42}$$

In most experimental settings we work within the thin crystal limit, thus we set

$$\beta \to 0, \tag{5.43}$$

and the final result for the generating function of the measurements becomes

$$\mathcal{G} = \frac{\pi w_1 w_2 \mathcal{N}_1\mathcal{N}_2 n_3^2}{\mathcal{A}_0}\exp\left[\frac{\mu_1\mu_2(1-T_1T_2)n_1n_2w_1w_2w_c^2}{2\mathcal{A}_0}\right]. \tag{5.44}$$

One can use Eq. (5.44) to generate the upconversion probability for any values of the azimuthal indices of the output state and the measurement state.

The result obtained in Eq. (5.44) confirms that the upconversion process does indeed act like an inner product operation (apart from the flip in the sign of the azimuthal index) with the necessary orthogonality and that it can, therefore, be used to extract the information of the Kraus operator from the output state. This follows from the fact that unless the azimuthal indices have the same magnitude and opposite signs the result would be null.

The expression in Eq. (5.44) can also be used to determine the nature of the coefficient function $\Pi(|\ell|)$ that was introduced in Eq. (5.5). Our assumption that $\Pi(|\ell|)$ is independent of the frequency is validated by the fact that the frequency components in the frequency comb that we select in our implementation are extremely close to each other.

By expanding Eq. (5.44) to all orders in $\mu_1\mu_2$

$$\mathcal{G} = \sum_{n=0}^{\infty}\frac{(-1)^n}{n!2^n}\frac{w_1w_2\mathcal{N}_1\mathcal{N}_2n_3^2\left[w_2w_1n_1n_2w_c^2(T_1T_2-1)\mu_1\mu_2\right]^n}{\pi\mathcal{A}_0^{n+1}}, \tag{5.45}$$

we obtain the coefficients of the LG modes in the SPDC state (dual of the SPUC process). The coefficients of this expansion are the Π-functions. In an effort to obtain a simplified expression for the Π-functions, we consider a few simplifications. We start with the signs T_1 and T_2. It can be seen that Eq. (5.45) is nonzero provided that $T_1T_2 = -1$, this corresponds to the case that the two LG modes having opposite signs as already alluded to above. Furthermore, as already alluded to as well, the only time that the generating function in Eq. (5.45) is also nonzero is if the number of derivatives taken with respect to the generating parameters is the same. This implies that the magnitude of the azimuthal indices for the LG modes has to be the same. Therefore, in substituting Eq. (5.38) into Eq. (5.45) and incorporating the consequence of substituting $T_1 T_2 = -1$ we obtain the following equation

$$\mathcal{G} = \frac{2w_1^2 w_2^2 n_3^2}{\mathcal{A}_0}\left(\sum_{n=0}^{\infty}\frac{1}{(n!)^2}\left[\frac{2n_1 n_2 w_1 w_2 w_c^2}{\mathcal{A}_0}\right]^n [\mu_1\mu_2]^n\right). \tag{5.46}$$

Given the above expression, we can remove the global magnitude through normalization (dividing by the multiplicative factor). Subsequent to this, the generating function can be written as

$$\mathcal{G}_0 = \sum_{n=0}^{\infty}\frac{1}{(n!)^2}\left[\frac{2n_1 n_2 w_1 w_2 w_c^2}{\mathcal{A}_0}\right]^n [\mu_1\mu_2]^n . \tag{5.47}$$

Based on the form of the generating function above, the Π-functions for the normalized generating function can be written as

$$\Pi(|\ell|) = \left(\frac{2n_1 n_2 w_1 w_2 w_c^2}{\mathcal{A}_0}\right)^{|\ell|} . \tag{5.48}$$

The factorial term $(n!)^2$ is not included above since it cancels off the effect of the derivatives and we have also substituted n with $|\ell|$.

When the measurement state is designed, one can weigh the coefficients of the different LG modes to compensate for the difference in the magnitude of $\Pi(|\ell|)$, caused by the different values of $|\ell|$, that would be produced in the upconversion process, as seen in Eq. (5.9).

If the different wavelengths are very close to each other, then the refractive indices seen by the output state and the measurement state would be approximately the same. Critical phase matching would then imply that $n_1 = n_2 = n_3$. If, furthermore, we assume that the mode sizes of the output state and the measurement state are the same $w_1 = w_2 = w_0$, then the coefficient function can be expressed as

$$\Pi(|\ell|) = 2^{|\ell|}\,(2+\alpha)^{-|\ell|} , \tag{5.49}$$

where

$$\alpha = \frac{w_0^2}{w_c^2}. \tag{5.50}$$

One would prefer that the coefficient function remains as constant as possible as a function of $|\ell|$; in other words, close to 1. From Eq. (5.49) we see that under the operating conditions $w_0 \ll w_c$ such that $\alpha \ll 1$ this result is approximately attainable $\Pi(|\ell|) \approx 1$.

5.4 Discussion and conclusions

The most common way to characterize a quantum channel is through quantum process tomography. The disadvantage of quantum process tomography is that one needs to prepare a set of basis states. In addition, one also needs to prepare an ensemble of identical input states. In other words, one needs to prepare the same state repeatedly to build up statistics from which one can extract the required information. For an increasing number of dimensions, quantum process tomography quickly becomes unpractically complex. Moreover, due to the required repetition of measurements, the complete measurement process runs over an extended period during which the conditions of the channel may change. As a result, it would not be possible to characterize a single realization of turbulence. The best it can do is to give information about the average behavior overall turbulence realizations.

In contrast, the use of classical light as proposed here and in [103] allows one to perform the process with a single pulse of bright light. A higher dimensionality does not lead to longer measurement times, but instead to a more complex measurement system. Therefore, it is not necessary to prepare an ensemble of input states and a large set of input basis states. The single-pulse implementations enable the classical scheme to characterize single realizations of turbulence, which represents a process that maintains purity.

The use of wavelength, rather than polarization as was done in [103], provides the means to implement channel characterization for arbitrary dimensions. There is no fundamental barrier to the number of dimensions. Therefore, the method is scalable. However, the complexity of the measurement system would increase drastically with an increase in the number of dimensions.

It is important to note that this scheme differs from the conventional classical methods that are based on the preparation of a set of orthogonal input modes, which are used to determine the classical crosstalk matrix. Instead, our scheme only requires the preparation of a single nonseparable input state.

When preparing the input state, one needs to ensure that the modes associated with different wavelength are properly separated on the SLM. To form beams that are well-separated, the incident beam needs to illuminate enough lines on the diffraction grating. The required number of illuminated lines is $N = \lambda/\Delta\lambda$. For a pulse repetition frequency of 1 GHZ and a nominal wavelength of $\lambda = 1$ μm, the number of lines that needs to be illuminated is on the order of 300 000. Diffraction gratings with several thousand lines per mm are commercially available. So, the input beam size needs to be on the order of a 100 mm to illuminate enough lines. Although challenging, this should be doable. Often the best setup for this type of system is to operate the diffraction gratings at the Littrow angle [151]. This will also avoid too much astigmatism in the first diffracted order.

For a three-dimensional implementation as we show here, the maximum size of the beam on the SLM would be one-fifth of the total width of the SLM (taking those beams that are blocked in between, into account). The typical number of pixels across the SLM is on the order of a thousand. Hence, one can expect that each beam on the SLM would have about 200 pixels on a side (200×200 in total) with which it can be modulated. This should be more than enough to achieve a reasonably well-defined spatial mode. For higher dimensions, one would obtain progressively smaller numbers of pixels. At some point, one would need to separate the beams onto different SLMs. This will make the system more complex, but it does not introduce a fundamental limit.

The modulation process that is used in the preparation of the measurement state is assumed to be an amplitude modulation with a suppressed carrier. It should be noted that to implement this form of modulation may require a more involved setup than what a single optical modulator would provide. Details of such a setup would depend on the experimental equipment that is used in the implementation.

In a down-conversion process, the signal and idler photons propagate at particular angles depending on their frequencies. One can design the down-conversion process so that the signal and idler both propagate collinearly with the pump at a particular frequency, but for different frequencies, they would have nonzero angles with respect to the pump because different frequencies are produced with different angles of propagation as governed by the phase matching conditions of the crystal. The inverse process (upconversion) would, therefore, require that the different frequencies enter the nonlinear crystal at the required angles to produce a successful upconversion incorporating all the different frequencies. However, if the frequencies are close enough to each other the differences in these angles would be negligible. This would be the case for a frequency comb where the differences among the different frequency components are on the order of a GHz. In that case, the differences in frequency are too small to produce significantly different propagation angles. (See for instance Appendix C in [60].)

The upconversion process is assumed to employ critical phase matching, such as type 1 phase matching. For higher efficiency, it is often advisable to use quasi-phase matching that involves type 0 phase matching. This would result in some changes in the details of the calculation. However, these changes are not expected to give significantly different results.

In the practical implementation of the measurements, it is assumed that the wavelength would always match up with a particular wavelength produced in the upconversion process. However, if the different wavelength components from which the input state and measurements states are composed are extremely close together, then the upconversion process would produce upconverted wavelengths that are also very close together. As a result, a wavelength filter may not be able to separate them to select the particular wavelength intended in the design. It may, therefore, require an additional diffraction grating-based filter after the upconversion process to select the specific wavelength that would enable the correct operation of the measurement process.

Chapter 6

Compressive sensing based quantum entanglement preservation of twisted photons

6.1 Introduction

Characterization and determination of quantum processes is a very crucial task that is necessary for the implementation of quantum communication and information processing systems. This is because it allows for the design of mitigation strategies against noise and other distortions that may negatively affect a quantum system. The standard method of characterizing a quantum channel is called quantum process tomography (SQPT) [3]. However, SQPT, as it is commonly abbreviated, is a resource intensive process that scales dramatically with the size of the quantum system [3, 152]. The number of resources that are required for SQPT is $O(N^4)$, where N is the dimension of the Hilbert space.

Atmospheric turbulence induced distortions lead to the scattering of input OAM modes into other modes [71, 74], and thus an increase in the dimensionality of the photonic quantum systems [89]. This implies that the application of SQPT would not be favorable for characterizing a turbulent atmospheric channel.

It is clear that for successful implementation of quantum communication systems with twisted photons (photons that have spiral wavefronts and carry OAM), there has to be a different method of determining and characterizing the turbulent quantum channel. This is where we employ compressive sensing [153, 154, 155], a data processing method that provides an efficient mechanism for the recovery of unknown signals from only a fraction of the required measurements. A generalization of this method to matrices is called matrix completion. In traditional compressive sensing, the signal has to have certain properties such as sparseness in the appropriate basis, whereas in the matrix generalization case the matrices have to be low rank for the method to be successful. Fortunately, this is the case for a single realization of atmospheric turbulence. The turbulence is treated as a unitary process that preserves the purity of quantum states.

Gross *et al.* [156] have established a method, based on a random selection of Pauli measurements, for efficient reconstruction of an unknown quantum state. They show that using their method they can reconstruct an unknown matrix of rank r with only $O(rNlog^2N)$ measurements, in contrast to the standard method of $O(N^2)$. In another study [157], a high-dimensional entangled state has been reconstructed from a significantly smaller number of measurements using a related approach based on compressive sensing. While this method for reconstruction of signals from an underdetermined system of equations is very popular in signals and image processing applications, it has now attracted interest and become topical in quantum information science related applications as well [156, 157, 158, 159, 160, 161, 162].

The aim of this work is to show, through numerical simulations, that compressive sensing is a viable technique for channel estimation and channel correction in the specific case of twisted light transmission in atmospheric turbulence. Further, we argue that a pairing of the method that has recently been proposed [148] and compressive sensing can lead to a more efficient protocol for the characterization of turbulent channels.

The outline of this contribution is as follows: In Sec. 6.2 we present the model for this work. Section 6.3 is based on the results of this work. Finally, the conclusions are given in Sec. 6.4.

6.2 Model

6.2.1 Channel matrix

The Choi-Jamiolkowski isomorphism [163] establishes a correspondence between a completely positive trace preserving quantum map Λ and a quantum state ρ as follows

$$\rho_\Lambda = (\Lambda_A \otimes \mathbb{1}_B)(|\psi\rangle\langle\psi|), \tag{6.1}$$

where

$$|\psi\rangle = \frac{1}{\sqrt{N}} \sum_{n=1}^{N} |n\rangle_A \otimes |n\rangle_B \tag{6.2}$$

is a maximally entangled state, $\mathbb{1}$ is the identity matrix which is the operator on subsystem B, and N is the dimension of the Hilbert space. This isomorphism means that the identification and characterization of the quantum channel is tantamount to performing a quantum state tomography. In the particular case of interest to us, we prepare our quantum system Eq. (6.2) by entangling the OAM state of an optical field with the wavelength of the optical field and therefore as a typical input state for our consideration we obtain [148]

$$|\psi\rangle = \frac{1}{\sqrt{2M+1}} \sum_{\ell=-M}^{M} |\ell, 0\rangle_A |\lambda_\ell\rangle_B \tag{6.3}$$

where $|\ell, 0\rangle$ represents a Laguerre-Gaussian (LG) mode with azimuthal index ℓ and radial index $p = 0$, λ_ℓ is the wavelength of the corresponding LG mode and M is an integer representing the maximum OAM. In the most general case, we would have an arbitrary radial index such that $|\ell, p\rangle$, however, here we set the radial index to zero for the input state of interest.

Transmission through the atmosphere causes the OAM modes to scatter into other modes. The atmospheric turbulence only affects the spatial degree of freedom and leaves the wavelength unaffected. Therefore, a given input OAM mode becomes, after propagating through the atmosphere,

$$|\ell, p\rangle \rightarrow \sum_n \sum_m \Lambda_{\ell,p}^{m,n} |m, n\rangle, \tag{6.4}$$

where $\Lambda_{\ell,p}^{m,n}$ is the tensor representation of the atmospheric turbulence Kraus operator Λ. This is the tensor that we have to characterize in order to understand the effects of the atmosphere.

The Kraus map Λ, has a rectangular matrix representation. It is an $n_1 \times n_2$ matrix such that $n_1 \geq n_2$. The expression for the Kraus operator in Eq. (6.4) is given as follows

$$\Lambda = \sum_n \sum_m |m, n\rangle\langle \ell, p| \Lambda_{\ell,p}^{m,n}. \tag{6.5}$$

The rectangular nature of the channel matrix can be seen by observing that the columns of the matrix are determined from the input OAM modes $\langle \ell, p|$. That is, the dimensionality of the input Hilbert space is finite and determines the number of columns of the matrix. On the other hand, the rows are determined from the crosstalk induced by the atmospheric turbulence. That is, the dimensionality of the spread in the OAM modes determines the length of the columns of the channel matrix.

6.2.2 Compressive sensing

Using the matrix completion method, it is possible to recover a low-rank matrix given that some of the elements of the matrix are unknown. Here, however, rather than to recover the quantum state density matrix from a sample of its elements $\rho_{i,j}$ we recover the full matrix that represents the quantum states in terms of a sample of the results of measurements made on the quantum system.

In the most general case, as already discussed in Chapter 2, the density matrix of a quantum system can be decomposed in terms of the Bloch representation as follows

$$\rho = \sum_{i=1}^{N^2} \alpha_i \tau_i, \tag{6.6}$$

where α_i are the elements of the so-called Bloch vector, N represents the dimensionality of the state vector and τ_i denotes the generalized Gell-Mann matrices (GGMs), including the identity matrix. The GGMs reduce to the Pauli matrices in the case that $N = 2$. In this formalism, the GGM form a convenient measurement basis for the characterization of the state. To determine the state through a tomography, one would have to perform measurements that reveal N^2 real parameters α_i. The Bloch vectors elements are the expectation values and are given as already discussed in Chapter 2

$$\alpha_i = \frac{\mathrm{tr}\,\{\tau_i \rho\}}{N}. \tag{6.7}$$

In the implementation of the modified matrix completion problem [156], we consider an undersampled set of measurements ($m \ll N^2$) that are chosen at random. That is, we consider a situation where there is only a subset of the total possible measurements α_i. With this, the optimization problem is described as follows:

$$\text{Minimise} \;\| \rho_{\mathrm{r}} \|_{\mathrm{tr}} \;\text{ such that} \begin{cases} \mathrm{tr}\{\rho_{\mathrm{r}}\} = 1, \\ \rho_{\mathrm{r}} = \rho_{\mathrm{r}}^{\dagger}, \\ \frac{\mathrm{tr}\{\rho_{\mathrm{r}}\tau_i\}}{N} = \alpha_i \text{ for } i = 1...m, \end{cases} \tag{6.8}$$

where ρ_{r} is the to-be-recovered density matrix, $\| \cdot \|_{\mathrm{tr}}$ is the trace norm of the matrix which is given by

$$\| \rho_{\mathrm{r}} \|_{\mathrm{tr}} = \mathrm{tr}\left\{ \sqrt{\rho_{\mathrm{r}}\rho_{\mathrm{r}}^{\dagger}} \right\}. \tag{6.9}$$

The compressive sensing algorithm is based on the singular value thresholding algorithm (SVT) [164]. However, we modify the algorithm to take advantage of known properties about the quantum state that we intend to recover [157]. Essentially, in applying the SVT algorithm we perform an eigenvalue decomposition of the density matrix

$$\rho_{\mathrm{r}} = \sum_j \sigma_j |\phi_j\rangle\langle\phi_j|, \tag{6.10}$$

where $|\phi_j\rangle$ are the eigenvectors of ρ_{r} and σ_j are the corresponding eigenvalues. Given the above decomposition, we apply the thresholding operator on the eigenvalues. That is, we select the eigenvalues that are above a certain threshold ϵ_0 that we fix apriori. By ensuring that the eigenvalues of the density matrix are real we ensure that the density matrix is Hermitian. A further requirement is the normalization of the density matrix to a trace of unity. This is achieved by merely dividing the resultant matrix by its trace.

The algorithm uses a guess matrix as a starting point for the optimization process. The most crucial step in setting up the guess matrix is choosing its dimensions. This is because the dimensions of this matrix should be representative of the conditions of the atmospheric turbulence that we are working under. We should have a matrix that is big enough to accommodate most of the non-zero elements of the spread in the OAM modes. Having determined the dimensions of the guess matrix, the algorithm can be applied.

After performing the above operations on the density matrix (thresholding and normalizing to unity), the obtained density matrix represents some real physical system, but it no longer corresponds to the density matrix whose measurements with respect to the GGM τ_i gives the correct measurement results $\{\alpha_i\}_{i=1...m}$. To overcome this hurdle we have to project the density matrix back into the linear space determined by τ_i and the corresponding results α_i by performing a projection procedure. This projection procedure is better understood from a geometrical perspective, which requires us to think in terms of hyperplanes.

As an aid to understand this projection operation, we re-express Eq. (6.7) in vector notation as follows

$$M\bar{\rho} = \bar{\alpha}, \tag{6.11}$$

where $\bar{\rho}$ is the vectorized density matrix, M is a matrix with rows representing the vectorized GGM, and $\bar{\alpha}$ denotes the vector of the measurement results. In this representation, it is rather trivial to notice that each vectorized GGM $\bar{\tau}_i$and its corresponding measurement result α_i can be associated with a hyperplane in N^2 dimensional space. The compressive sensing approach is meant to solve an under-determined linear system of equations. The solution is a common point to all the m hyperplanes. However, having performed the former operations (thresholding and normalization) a point which does not lie in the linear space given in Eq. (6.11) is obtained. That is,

$$M\bar{\rho}_0 \neq \bar{\alpha}. \tag{6.12}$$

As a resolution to this issue, the "recently" obtained density matrix ρ_0 is modified to give the correct measurement results. By recently obtained matrix it is meant the density matrix that has been recomposed within the bounds of Hermiticity and trace normalization. The projection is done stepwise for each value of α_i. The projection starts by defining a vector $\bar{v}_i$ that is normal to the hyperplane, $\bar{\tau}_i\bar{\rho} = \alpha_i$, such that it has magnitude given as

$$|\bar{v}_i| = \alpha_i - \bar{\hat{v}} \cdot \bar{\rho}_{i-1}, \tag{6.13}$$

where $\hat{\bar{v}}$ is the unit vector that is normal to the hyperplane. The new density matrix becomes

$$\bar{\rho}_i = \bar{\rho}_{i-1} + \bar{v}_i. \tag{6.14}$$

This projection process is performed for all m measurements. At the end of this process, we start again and perform the procedure for Hermiticity and trace normalization. That is, we perform the thresholding operation and further recompose the matrix according to the conditions in the optimization problem statement.

The above described processes are performed iteratively and the desired matrix is said to have been recovered if the norm of the difference between two consecutive iterations is within some tolerance *tol*, where *tol* is a parameter in the algorithm.

6.2.3 Channel correction

The following procedure represents the main contribution of this work. It involves the generation of the Kraus operator matrix from the estimated density matrix. The density matrix is estimated as described above using compressive sensing.

The full Kraus operator matrix can be obtained from the density matrix of the output state. This is made possible by the fact that propagation through the atmosphere is a unitary process. If the input state is pure, then the output state is also a pure state. We also assume that the truncation of the output state, to a finite dimension, does not affect the unitary nature of the process. Since we assume that the entire process is unitary, we can consider the Kraus operator as a unitary operator. This implies that its Hermitian adjoint represents the inverse process.

Given the Kraus operator tensor Λ, whose elements are obtained from the state of the system that is reconstructed using the methods of the previous section on compressive sensing, we formulate the correction process as follows

$$
\begin{aligned}
|\Psi\rangle_{\text{in}} &= (\Lambda_A \otimes \mathbb{1}_B)^{\dagger} |\Psi\rangle_{\text{out}} \\
&= \left(\sum_n \sum_m |m,n\rangle \Lambda_{\ell,p}^{m,n} \langle \ell, p| \otimes \mathbb{1}_B \right)^{\dagger} |\Psi\rangle_{\text{out}},
\end{aligned}
\tag{6.15}
$$

where the dagger denotes a Hermitian adjoint. The results of this process are given next, in Sec. 6.3.

6.3 Results

As an example of our proposal to perform quantum channel estimation and correction by using compressive sensing, we consider a qutrit input state (see Fig.6.1 for density matrix) given in terms of the spatial (OAM) and wavelength degrees of freedom

$$
|\Psi\rangle_{\text{in}} = \frac{1}{\sqrt{3}} \left[|\ell, 0\rangle |\lambda_{\ell}\rangle + |0,0\rangle |\lambda_0\rangle + |\bar{\ell}, 0\rangle |\lambda_{\bar{\ell}}\rangle \right]. \tag{6.16}
$$

This state is very simple, and it is obviously very clear that to characterize such a state there is hardly any use for compressive sensing. However, transmission through atmospheric turbulence causes crosstalk and the dimensionality of the quantum states grows very fast in an unpredictable manner. The severity of the crosstalk depends on the strength of turbulence. Even under specific turbulence conditions, the crosstalk is not fixed; it is random. Therefore, the dimensions of the Kraus operator are not fixed and can be very huge for severe turbulence.

The information about the atmospheric turbulence Kraus operator is contained in the output state of the system. The channel matrix is determined by performing a state tomography. For each realization of the atmospheric turbulence, the quantum state remains pure and is thus low rank. Compressive sensing is used to estimate the quantum state and subsequently to determine the Kraus operator matrix. The purity of a state implies that it is well represented by a state vector $|\psi_{\text{out}}\rangle$, as detailed out in Chapter 2. This further implies that the density matrix has rank equal to unity. The input state vector has dimension $N_{\text{in}} = N_A \cdot N_B$. In the particular case of the state described in Eq. (6.16), we have that $N_A = N_B = 3$. This implies that $N_{\text{in}} = 3^2$, and the corresponding density matrix has 3^4 elements. After passing through turbulence, the dimension of photon A grows in an unpredictable fashion. The dimension of the output density matrix becomes $N_{\text{out}} \times N_{\text{out}}$, with N_{out} being the unpredictable output state dimension. For the LG modes used in the numerical simulation with typical wavelength $\lambda = 1$ μm and a waist $w_0 = 0.1$ m, in turbulence conditions given by $C_n^2 = 1 \times 10^{-16}$ m$^{-2/3}$ and after propagating for a distance of $z = 2z_R$, N_{out} is above 300.

In the numerical simulations, we considered one-sided turbulence as an illustrative example. Since we are working with the qutrit case, the simulation required the propagation of three different optical fields through the atmospheric turbulence. The three LG modes that were used had azimuthal indices $\ell = 1$, $\ell_0 = 0$ and $\bar{\ell} = -1$; the same waist ($w_0 = 0.1$ m). Although the wavelengths of the three optical fields are different, in practical experimental setups the differences can be made very small. Therefore, the same wavelength $\lambda = 1$ μm was used for all three modes.

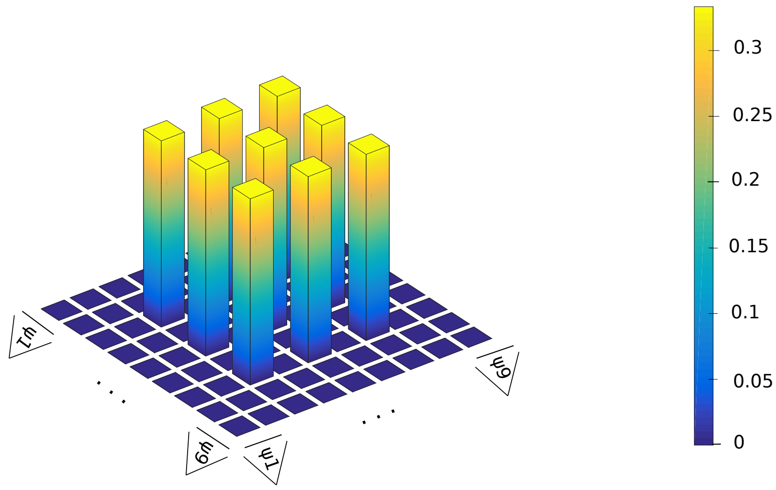

FIGURE 6.1: Schematic representation of the density matrix of the input qutrit state.

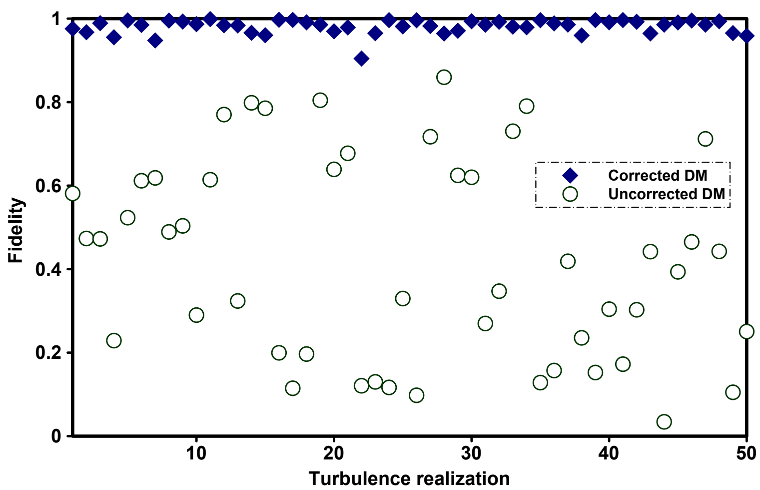

FIGURE 6.2: Fidelity as a function of atmospheric turbulence realisation. The circle markers represent the truncated and uncorrected density matrix and the diamond markers represent the corrected density matrix.

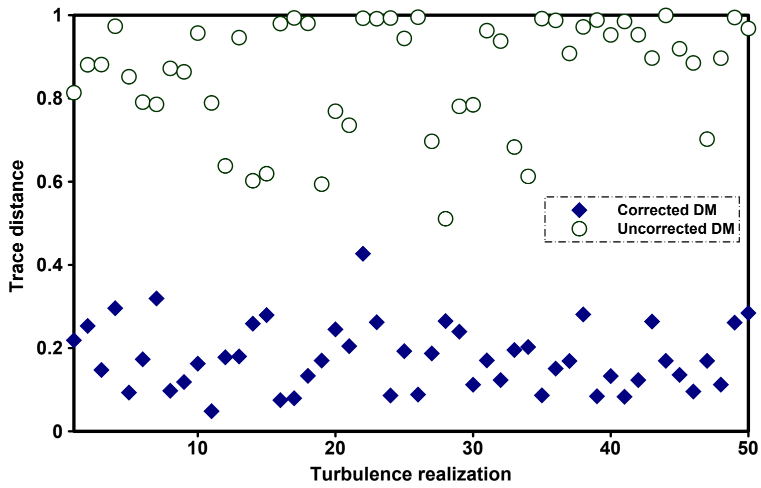

FIGURE 6.3: Trace distance as a function of atmospheric turbulence realizations. The circle markers represent the truncated and uncorrected density matrix and the diamond markers represent the corrected density matrix.

To further characterize the atmospheric turbulence, we considered the normalized turbulence strength which is given as

$$\kappa = \frac{C_n^2 w_0^{11/3} \pi^3}{\lambda^3}. \tag{6.17}$$

Given the above information it follows that we had $\kappa = 0.0667$. Furthermore, we consider a total propagation distance of $z = 2z_R$ m, the Fried parameter that was considered is $r_0 = 0.09$ m, where the Fried parameter is rewritten here for convenience

$$r_0 = 0.185 \left(\frac{\lambda^2}{C_n^2 z} \right)^{3/5}. \tag{6.18}$$

As expected, the LG modes scatter into other modes which were not initially included in the input state. For our illustration, we consider radial indices up to $p = 7$, and for each of the radial indices, we considered azimuthal indices in the range $-7 \leq \ell \leq 7$. This implies that the overall output dimension of the photon in subsystem A becomes $N_A = 105$. Therefore the number of elements of this output density matrix becomes just below 100000. This means that to specify a density matrix obtained in this way would require a measurement of 315^2 real parameters.

Using compressive sensing, the state of the output density matrix can be identified by a significantly smaller number of measurements. For this work, around 3% (which in this case is roughly 3000) of the total number of measurements were used and yet the output density matrix was reconstructed reliably. Using the reconstructed density matrix, the elements of Kraus operator $\hat{\Lambda}$ were extracted. The Kraus operator was used to generate the correction matrix, which was used to correct for the perturbation.

The idea here is that the input state in Eq. (6.16) is used to obtain information about the one-sided channel. This channel information is used to correct a quantum state that is subject to the same channel conditions.

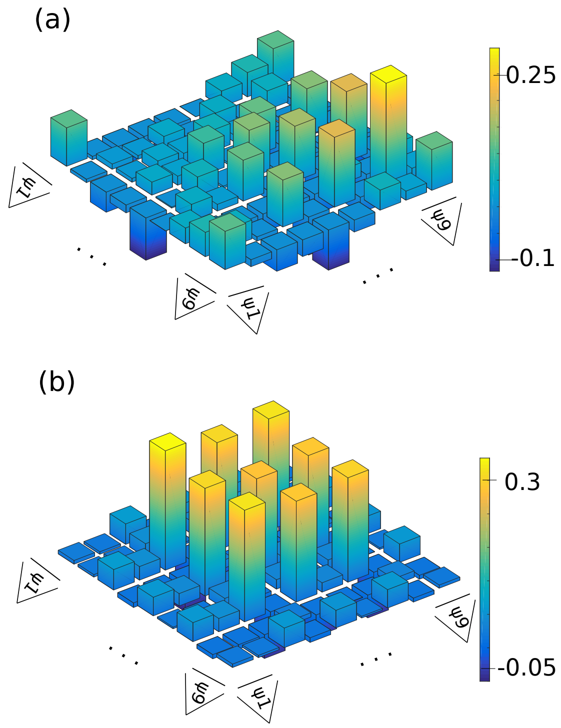

FIGURE 6.4: Arbitrary density matrices for the output quantum state after passing through the atmospheric turbulence. a) The uncorrected, truncated density matrix; b) the corrected density matrix.

The result of the correction using the information obtained from the input state in Eq. (6.16) was then tested for fidelity and trace distance against the maximally entangled qutrit quantum state.

The fidelity is computed with respect to the maximally entangled quantum state as follows

$$F(\rho_c, |\Psi\rangle\langle\Psi|) = \mathrm{tr}\left\{\sqrt{\sqrt{\rho_c}|\Psi\rangle\langle\Psi|\sqrt{\rho_c}}\right\}, \tag{6.19}$$

where

$$|\Psi\rangle = \frac{1}{\sqrt{3}}\left[|\ell,0\rangle|\bar{\ell},0\rangle + |0,0\rangle|0,0\rangle + |\bar{\ell},0\rangle|\ell,0\rangle\right] \tag{6.20}$$

is the input quantum state entangled (maximally) in the OAM degrees of freedom that went through the same one-sided channel as the input state in Eq. (6.16), and ρ_c is the corrected density matrix from the compressive sensing algorithm. The results of this calculations are shown in Fig. 6.2.

The trace distance, which is shown Fig. 6.3, is defined as

$$D(\rho_c, |\Psi\rangle\langle\Psi|) = \frac{1}{2}\mathrm{tr}\left\{|\rho_c - |\Psi\rangle\langle\Psi||\right\}, \tag{6.21}$$

where the magnitude $|A|$ of a matrix is given as $|A| = \sqrt{A^\dagger A}$. Both the plots in Figs. 6.2 & 6.3 are plotted against the different realizations of the atmospheric turbulence. In Fig. 6.2 it can be seen that the corrected density matrix is really close to the ideal maximally entangled input quantum state. This is in contrast to the data points of the truncated and uncorrected density

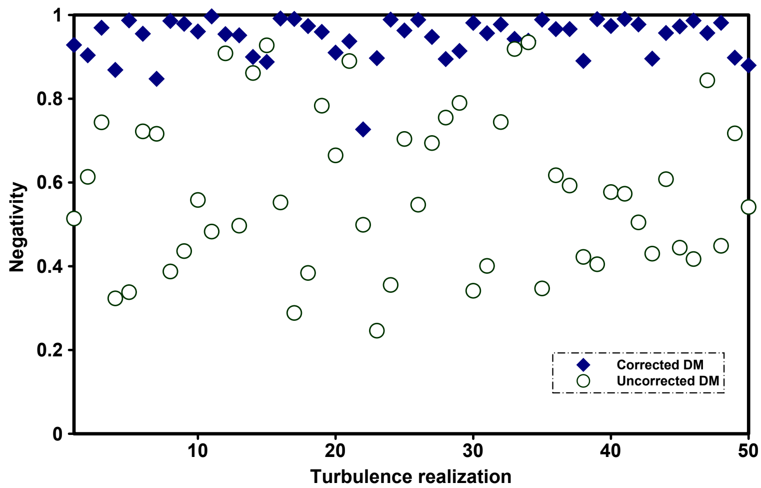

FIGURE 6.5: The negativity of the corrected and uncorrected density matrices as a function of turbulence realization. The circle markers represent the truncated and uncorrected density matrix and the diamond markers represent the corrected density matrix.

matrix. The mean fidelity for the corrected density matrix over the 50 turbulence realizations is 0.981 ± 0.002 and the uncorrected has a fidelity of 0.424 ± 0.034, where the error is given as the standard error. The same conclusion can also be reached from looking at Fig. 6.3 which is the trace distance. The mean trace distance for the corrected density matrix is 0.177 ± 0.011 and the uncorrected has a trace distance of 0.864 ± 0.019. Both these results imply that the correction procedure was successful.

The density matrices of an arbitrary realization, real part, for the uncorrected and corrected density matrices are shown in Fig. 6.4. The axes are denoted by the kets

$$|\psi_n\rangle = |\ell_j, \lambda_k\rangle, \tag{6.22}$$

where n runs from $1-9$, ℓ_j is an OAM mode in the set $\{\bar{\ell}, 0, \ell\}$ with j given as

$$j = mod(n-1, 3) + 1, \tag{6.23}$$

and λ_k is the associated wavelength in the set $\{\lambda_1, \lambda_2, \lambda_3\}$ with

$$k = mod(n-k, 4) + (-1)^{n-k}. \tag{6.24}$$

A visual comparison of the density matrices shows that the corrected density matrix is closer to the input density density matrix. The results show that compressive sensing can be a very useful and powerful method for the implementation of a quantum communication system.

As a further measure for the usefulness of the compressive technique, the negativity (see Chapter 2) of the density matrices was calculated in order to quantify the entanglement. Figure 6.5 shows that the quantum entanglement of the system really improves with the correction procedure that is based on the compressive sensing technique. The mean negativity for the corrected density matrix over the 50 realizations was calculated to be 0.95 ± 0.01. This value can be contrasted with that of the uncorrected density matrix which is 0.58 ± 0.03.

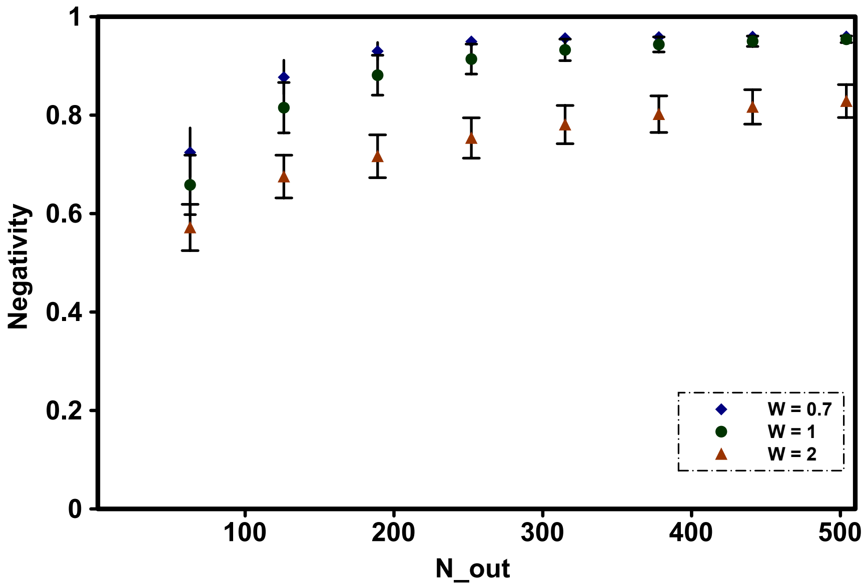

FIGURE 6.6: The negativity of the corrected density matrix as a function of N_{out} for different scintillation strengths W. For clarity we show the error bars with different sysmbols. The error bars for $W = 0.7$ have zero width. The error bars for $W = 1$ have medium width. The error bars for $W = 2$ have the largest width.

In order to inform the practical design for the implementation of compressive sensing for optical and quantum communication systems, the performance of the correction process as a function of the N_{out} was considered. Fig. (6.6) shows three curves at the same normalized turbulence $\kappa = 0.067$ at different scintillation strengths (by changing the propagation distance), where the scintillation strength is represented by the dimensionless number $W = w_0/r_0$. It can be seen that the negativity increases with increase in the Hilbert space dimension N_{out}. This implies that the size of the guess matrix is very important for the success of this method. In spite of this dependence on N_{out}, we also find that there is a value of N_{out} where the correction reaches a plateau. This value is directly related to the turbulence conditions. The rate at which the plateau is approached is a function of the scintillation strength. In Fig. 6.6 it can be seen that while a negativity of around 0.9 is reached for the scintillation strengths $W = 0.7, 1$ at N_{out} around 300, the correction is not yet optimal for the scintillation strength $W = 2$.

This opens up an opportunity to improve the algorithm by applying other methods such as deep learning or other advanced machine learning algorithms. Such algorithms could be used to teach the system to look for trends that could be used to decide upon the appropriate value of N_{out}.

6.4 Conclusions

We have performed a numerical analysis of the performance of a compressive sensing based correction method on OAM states that have been transmitted through turbulence. The compressive sensing algorithm that was used is based on a singular value thresholding technique.

The results show that compressive sensing drastically reduces the required number of measurements for the characterization of the turbulent channel, and could thus be very useful in the design of quantum communication systems that are based on the OAM states of light. Our argument is that compressive sensing can be used in conjunction with the method proposed in [148] for high dimensional systems. this method, which uses classical light, can be used to make the subset of the necessary measurements. A protocol can then be developed which uses these two methods to probe the high dimensional Hilbert space for the channel matrix, which would then be used for the correction of high dimensional quantum system.

As a further study, we intend to investigate the use of deep learning or machine learning at large as methods that inform the system on the appropriate values of N_{out} [165].

Chapter 7

Conclusions

7.1 Achievements and the future

The work in this thesis can be put into two categories: Firstly, we studied the effect of atmospheric turbulence on single-photon optical fields and on quantum entangled OAM systems. Secondly, the mitigation against the atmospheric turbulence on OAM based quantum systems was considered.

The evolution of single-photon optical fields propagating through atmospheric turbulence was studied under arbitrary turbulence conditions. The single photon solution to the infinitesimal propagation equation (IPE) was obtained. The solution was used to calculate the coupling of the optical power from one orbital angular momentum (OAM) mode, the input mode, to different OAM modes due to the scintillation caused by the atmospheric turbulence. The results of the coupling of optical power were also obtained in accordance with the single phase screen (SPS) model. The predictions of the IPE model, which is valid under all scintillation conditions, were compared with the predictions of the SPS model. The SPS model is only valid under weak scintillation. It was found that the SPS curves are governed by a single scale parameter. It is called the weak scintillation scale and is determined by the location at which the curves change slopes. The IPE curves start by following the SPS curves, however, they begin to deviate at some point when the scintillation strength crosses a certain threshold. The scale at which the IPE deviates from the SPS is referred to as the deviation scale.

Having studied the two theoretical models, numerical simulations were performed using a multi-phase screen (MPS) model based on the Kolmogorov theory of turbulence. The results of the numerical simulations were compared with the predictions of both models. It was observed that the numerical simulations follow the IPE predictions more closely than the SPS predictions. However, it was also observed that there is a slight discrepancy in the IPE predictions and numerical simulations. The reason is attributed to the quadratic structure function approximation. In deriving the IPE, an approximation to the Kolmogorov theory structure function is made due to tractability reasons. Therefore, this may lead to some deviation between the IPE results and the numerical results in strong scintillation conditions. If, however, the results that were obtained are anything to go by, the effect of the quadratic approximation is not that severe.

This work was presented in Chapter 3. It served to show that the IPE, which was originally derived for entangled photonic quantum systems, can also be used to describe the evolution of single-photon optical fields propagating through atmospheric turbulence.

In performing this work, it was further found questionable that the deviation of the SPS and the IPE represents the onset of strong scintillation. This is because it was observed that the deviation does not occur at the expected Rytov variance for weak scintillation. This could imply that the deviation indicates the point where the SPS approximation breaks down, for whatever reason. Therefore, the nature of the deviation scale is a matter to be further investigated.

In Chapter 4 a theoretical and experimental study was undertaken to investigate the effect of atmospheric turbulence on the Hong Ou Mandel (HOM) interference effect. In performing the investigation, two types of channels were considered: a single-sided channel and a double-sided channel. Furthermore, only weak scintillation conditions were considered. The single-sided weak scintillation channel results showed that the HOM interference effect is not affected by the atmospheric turbulence. The reason for this behavior is attributed to the fact that in such conditions the atmospheric turbulence does not convert the symmetric quantum state into the anti-symmetric quantum state.

In the double-sided weak scintillation channel case, it was found that the effect of the atmospheric turbulence on the HOM dip is small. Moreover, it was also observed that with an appropriate choice of the crystal length and pump mode size the effect of the atmospheric turbulence on the HOM interference for the two-sided channel can be reduced to a negligible level.

Therefore, in conclusion, it can be said that the HOM interference effect is not really affected by the atmospheric turbulence under weak scintillation conditions. This has positive implications for the implementation of free-space quantum communication and for remote-clock synchronization protocols that are based on the second-order quantum interference effects.

As a further study, it would be interesting to consider how the results of this work could be affected in strong scintillation conditions.

In Chapter 5 an extension of the method proposed by Ndagano *et al.* for characterizing a quantum channel using classical light was proposed. The method that was proposed, in contrast to the original one, is for high dimensional quantum systems. The method uses a non-separable input state that has correlations between the spatial and wavelength degrees of freedom. It further incorporates spontaneous parametric upconversion or sum-frequency generation. The proposed scheme details how to implement it by discussing the three main issues that are involved: details about how to prepare the input non-separable state, the preparation of the measurement states, and the measurement process itself were discussed.

Using a singular-value- thresholding (SVT) based compressive sensing method, in Chapter 6 it was shown numerically that compressive sensing can be used to estimate a quantum channel with a reduced number of measurements. As a way of example, a qutrit input sate was considered. The success of the compressive sensing method was quantified by the trace distance, fidelity, and the negativity. Further, it was argued that the compressive sensing method can be combined with the classical light method described above to develop an efficient protocol for free-space optical and quantum communication systems that are based on the orbital angular momentum of light. It was also suggested that machine learning algorithms could be incorporated as part of the protocol to develop quantum error correction systems that can learn and thus enhance the correction scheme.

As a future study, we intend to implement the channel estimation and channel correction methods in an experiment.

Bibliography

[1] W. Diffie and M. E. Hellman. “Privacy and authentication: An introduction to cryptography”. In: *Proceedings of the IEEE* 67 (1979), pp. 397–427.

[2] R. L. Rivest, A. Shamir, and L. Adleman. “A method for obtaining digital signatures and public-key cryptosystems”. In: *Communications of the ACM* 21 (1978), pp. 120–126.

[3] M. A. Nielsen and I. L. Chuang. *Quantum Computation and Quantum Information*. Cambridge, England: Cambridge University Press, 2000.

[4] P. W. Shor. “Polynomial-time algorithms for prime factorization and discrete logarithms on a quantum computer”. In: *SIAM Review* 41 (1999), pp. 303–332.

[5] J. P. Gordon, H. J. Zeiger, and C. H. Townes. “The maser−new type of microwave amplifier, frequency standard, and spectrometer”. In: *Physical Review* 99 (1955), p. 1264.

[6] A. L. Schawlow and C. H. Townes. “Infrared and optical masers”. In: *Physical Review* 112 (1958), p. 1940.

[7] T. H. Maiman. “Stimulated optical radiation in ruby”. In: (1960).

[8] P. A. M. Dirac. “The quantum theory of the emission and absorption of radiation”. In: *Proceedings of the Royal Society of London. Series A, Containing Papers of a Mathematical and Physical Character* 114 (1927), pp. 243–265.

[9] E. Fermi. “Quantum theory of radiation”. In: *Reviews of Modern Physics* 4 (1932), p. 87.

[10] R. J. Glauber. “The quantum theory of optical coherence”. In: *Physical Review* 130 (1963), p. 2529.

[11] G. Grynberg, A. Aspect, and C. Fabre. *Introduction to quantum optics: from the semi-classical approach to quantized light*. Cambridge university press, 2010.

[12] C. H. Bennett, G. Brassard, and N. D. Mermin. “Quantum cryptography without Bells theorem”. In: *Physical Review Letters* 68 (1992), p. 557.

[13] C. H. Bennett. “Quantum cryptography using any two nonorthogonal states”. In: *Physical Review Letters* 68 (1992), p. 3121.

[14] D. Bruß. “Optimal eavesdropping in quantum cryptography with six states”. In: *Physical Review Letters* 81 (1998), p. 3018.

[15] V. Scarani, A. Acin, G. Ribordy, and N. Gisin. “Quantum cryptography protocols robust against photon number splitting attacks for weak laser pulse implementations”. In: *Physical Review Letters* 92 (2004), p. 057901.

[16] D. Stucki, S. Fasel, N. Gisin, Y. Thoma, and H. Zbinden. "Coherent one-way quantum key distribution". In: *Photon Counting Applications, Quantum Optics, and Quantum Cryptography*. Vol. 6583. International Society for Optics and Photonics. 2007, p. 65830L.

[17] K. Inoue, E. Waks, and Y. Yamamoto. "Differential phase shift quantum key distribution". In: *Physical Review Letters* 89 (2002), p. 037902.

[18] C. H. Bennett and Brassard. G. "Quantum cryptography: public-key distribution and coin tossing". In: *Proceedings of IEEE International Conference on Computers Systems and Signal Processing*. 1984, pp. 175–179.

[19] A. K. Ekert. "Quantum cryptography based on Bell's theorem". In: *Physical Review Letters* 67 (1991), pp. 661–663.

[20] P. A. M. Dirac. *The principles of quantum mechanics*. 27. Oxford university press, 1981.

[21] R. G. Newton. *How physics confronts reality: Einstein was correct, but Bohr won the game*. World Scientific, 2009.

[22] A. Einstein, B. Podolsky, and N. Rosen. "Can quantum-mechanical description of physical reality be considered complete?" In: *Physical Review* 47 (1935), p. 777.

[23] E. Schrödinger. "Quantum Theory and Measurement". In: *Naturwiss* 23 (1935), p. 807.

[24] J. F. Clauser, M. A. Horne, A. Shimony, and R. A. Holt. "Proposed experiment to test local hidden-variable theories". In: *Physical Review Letters* 23 (1969), p. 880.

[25] S. J. Freedman and J. F. Clauser. "Experimental test of local hidden-variable theories". In: *Physical Review Letters* 28 (1972), p. 938.

[26] C. H. Bennett and D. P. DiVincenzo. "Quantum information and computation". In: *Nature* 404 (2000), p. 247.

[27] C. H. Bennett, G. Brassard, C. Crépeau, R. Jozsa, A. Peres, and W. K. Wootters. "Teleporting an unknown quantum state via dual classical and Einstein-Podolsky-Rosen channels". In: *Physical Review Letters* 70 (1993), p. 1895.

[28] D. Bouwmeester, J.-W Pan, K. Mattle, M. Eibl, H. Weinfurter, and A. Zeilinger. "Experimental quantum teleportation". In: *Nature* 390 (1997), pp. 575–579.

[29] C. H. Bennett and S. J. Wiesner. "Communication via one-and two-particle operators on Einstein-Podolsky-Rosen states". In: *Physical Review Letters* 69 (1992), p. 2881.

[30] J. T. Barreiro, Tzu-Chieh Wei, and P. G Kwiat. "Beating the channel capacity limit for linear photonic superdense coding". In: *Nature Physics* 4 (2008), p. 282.

[31] H. Bechmann-Pasquinucci and W. Tittel. "Quantum cryptography using larger alphabets". In: *Physical Review A* 61 (2000), p. 062308.

[32] S. P. Walborn, D. S. Lemelle, M. P. Almeida, and P. H. S. Ribeiro. "Quantum key distribution with higher-order alphabets using spatially encoded qudits". In: *Physical Review Letters* 96 (2006), p. 090501.

[33] J. H. Poynting. "The wave motion of a revolving shaft, and a suggestion as to the angular momentum in a beam of circularly polarised light". In: *Proc. R. Soc. Lond. A* 82 (1909), pp. 560–567.

[34] L. Mandel and E. Wolf. *Optical coherence and quantum optics*. New York: Cambridge University Press, 1995.

[35] R. A. Beth. "Mechanical detection and measurement of the angular momentum of light". In: *Physical Review* 50 (1936), p. 115.

[36] C. G. Darwin. "Notes on the theory of radiation". In: *Proceedings of the Royal Society of London. Series A, Containing Papers of a Mathematical and Physical Character* 136 (1932), pp. 36–52.

[37] C. J. Bouwkamp and H. B. G. Casimir. "On multipole expansions in the theory of electromagnetic radiation". In: *Physica* 20 (1954), pp. 539–554.

[38] Morris Edgar Rose and RB Lindsay. "Multipole fields". In: *Physics Today* 8 (1955), p. 22.

[39] L. Allen, M. W. Beijersbergen, R. J. C. Spreeuw, and J. P. Woerdman. "Orbital angular momentum of light and the transformation of Laguerre-Gaussian laser mode". In: *Physical Review A* 45 (1992), pp. 8185–8189.

[40] Lasers Siegman et al. "University science books". In: *Mill Valley, CA* (1986), pp. 858–890.

[41] M. I. Kolobov. *Quantum imaging*. Springer Science & Business Media, 2007.

[42] B. E. A. Saleh and M. C. Teich. *Fundamentals of photonics*. Vol. 22. Wiley New York, 1991.

[43] M. W. Beijersbergen, L. Allen, H. Van der Veen, and J. P. Woerdman. "Astigmatic laser mode converters and transfer of orbital angular momentum". In: *Optics Communications* 96 (1993), pp. 123–132.

[44] L. Allen, M. J. Padgett, and M. Babiker. "The orbital angular momentum of light". In: *Progress in Optics*. Elsevier, 1999, pp. 291–372.

[45] M. W. Beijersbergen, R. P. C. Coerwinkel, M. Kristensen, and J. P. Woerdman. "Helical-wavefront laser beams produced with a spiral phaseplate". In: *Optics Communications* 112 (1994), pp. 321–327.

[46] G. A. Turnbull, D. A. Robertson, G. M. Smith, L. Allen, and M. J. Padgett. "The generation of free-space Laguerre-Gaussian modes at millimetre-wave frequencies by use of a spiral phaseplate". In: *Optics Communications* 127 (1996), pp. 183–188.

[47] S. S. R. Oemrawsingh, J. A. W. Van Houwelingen, E. R. Eliel, J. P. Woerdman, E. J. K. Verstegen, J. G. Kloosterboer, and G. W. t Hooft. "Production and characterization of spiral phase plates for optical wavelengths". In: *Applied Optics* 43 (2004), pp. 688–694.

[48] K. Sueda, G. Miyaji, N. Miyanaga, and M. Nakatsuka. "Laguerre-Gaussian beam generated with a multilevel spiral phase plate for high intensity laser pulses". In: *Optics Express* 12 (2004), pp. 3548–3553.

[49] L. Marrucci, C. Manzo, and D. Paparo. "Optical spin-to-orbital angular momentum conversion in inhomogeneous anisotropic media". In: *Physical Review Letters* 96.16 (2006), p. 163905.

[50] E. Karimi, B. Piccirillo, E. Nagali, L. Marrucci, and E. Santamato. "Efficient generation and sorting of orbital angular momentum eigenmodes of light by thermally tuned q-plates". In: *Applied Physics Letters* 94 (2009), p. 231124.

[51] V. Y. Bazhenov, M. V. Vasnetsov, and M. S. Soskin. "Laser beams with screw dislocations in their wavefronts". PhD thesis. 1990.

[52] N. R. Heckenberg, R. McDuff, C. P. Smith, and A. G. White. "Generation of optical phase singularities by computer-generated holograms". In: *Optics Letters* 17 (1992), pp. 221–223.

[53] N. R. Heckenberg, R. McDuff, C. P. Smith, H. Rubinsztein-Dunlop, and M. J. Wegener. "Laser beams with phase singularities". In: *Optical and Quantum Electronics* 24 (1992), S951–S962.

[54] D. McGloin and K. Dholakia. "Bessel beams: diffraction in a new light". In: *Contemporary Physics* 46 (2005), pp. 15–28.

[55] J. Durnin, J. J. Miceli Jr, and J. H. Eberly. "Diffraction-free beams". In: *Physical Review Letters* 58 (1987), p. 1499.

[56] M. A. Bandres and J. C. Gutiérrez-Vega. "Ince–Gaussian modes of the paraxial wave equation and stable resonators". In: *JOSA A* 21 (2004), pp. 873–880.

[57] J. C. Gutiérrez-Vega, M. D. Iturbe-Castillo, and S. Chávez-Cerda. "Alternative formulation for invariant optical fields: Mathieu beams". In: *Optics Letters* 25 (2000), pp. 1493–1495.

[58] A. Migdall, S. V. Polyakov, J. Fan, and J. C. Bienfang. *Single-Photon Generation and Detection: Physics and Applications*. Vol. 45. Academic Press, 2013.

[59] R. W. Boyd. *Nonlinear optics*. Elsevier, 2003.

[60] Y. Shih. "Entangled biphoton source — property and preparation". In: *Rep. Prog. Phys.* 66 (2003), p. 1009.

[61] H. Huang and J. H. Eberly. "Correlations and one-quantum pulse shapes in photon pair generation". In: *Journal of Modern Optics* 40 (1993), pp. 915–930.

[62] P. G. Kwiat, A. M. Steinberg, and R. Y. Chiao. "High-visibility interference in a Bell-inequality experiment for energy and time". In: *Physical Review A* 47 (1993), R2472.

[63] A. Mair, A. Vaziri, G. Weihs, and A. Zeilinger. "Entanglement of the orbital angular momentum states of photons". In: *Nature* 412 (2001), p. 313.

[64] H. H. Arnaut and G. A. Barbosa. "Orbital and intrinsic angular momentum of single photons and entangled pairs of photons generated by parametric down-conversion". In: *Physical Review Letters* 85 (2000), pp. 286–289.

[65] S. Franke-Arnold, S. M. Barnett, M. J. Padgett, and L. Allen. "Two-photon entanglement of orbital angular momentum states". In: *Physical Review A* 65 (2002), p. 033823.

[66] A. Vaziri, G. Weihs, and A. Zeilinger. "Experimental two-photon, three-dimensional entanglement for quantum communication". In: *Physical Review Letters* 89 (2002), p. 240401.

[67] S. Gröblacher, T. Jennewein, A. Vaziri, G. Weihs, and A. Zeilinger. "Experimental quantum cryptography with qutrits". In: *New J. of Phys.* 8 (2006), p. 75.

[68] M. Krenn, R. Fickler, M. Fink, J. Handsteiner, M. Malik, T. Scheidl, R. Ursin, and A. Zeilinger. "Communication with spatially modulated light through turbulent air across Vienna". In: *New Journal of Physics* 16 (2014), p. 113028.

[69] G. Vallone, V. DâĂŹAmbrosio, A. Sponselli, S. Slussarenko, L. Marrucci, F. Sciarrino, and P. Villoresi. "Free-space quantum key distribution by rotation-invariant twisted photons". In: *Physical review letters* 113.6 (2014), p. 060503.

[70] M. Mafu, A. Dudley, S. Goyal, D. Giovannini, M. McLaren, M. J. Padgett, T. Konrad, F. Petruccione, N. Lütkenhaus, and A. Forbes. "Higher-dimensional orbital-angular-momentum-based quantum key distribution with mutually unbiased bases". In: *Physical Review A* 88 (2013), p. 032305.

[71] C. Paterson. "Atmospheric Turbulence and Orbital Angular Momentum of Single Photons for Optical Communication". In: *Physical Review Letters* 94 (2005), p. 153901.

[72] B.-J. Pors, C. H. Monken, E. R. Eliel, and J. P. Woerdman. "Transport of orbital-angular-momentum entanglement through a turbulent atmosphere". In: *Optical Express* 19 (2011), p. 6671.

[73] G. Gbur and R. K. Tyson. "Vortex beam propagation through atmospheric turbulence and topological charge conservation". In: *J. Opt. Soc. Am. A* 25 (2008), pp. 225–230.

[74] G. A. Tyler and R. W. Boyd. "Influence of atmospheric turbulence on the propagation of quantum states of light carrying orbital angular momentum". In: *Optics Letters* 34 (2009), pp. 142–144.

[75] A. K. Jha, G. A. Tyler, and R. W. Boyd. "Effects of atmospheric turbulence on the entanglement of spatial two-qubit states". In: *Physical Review A* 81 (2010), p. 053832.

[76] C. Gopaul and R. Andrews. "The effect of atmospheric turbulence on entangled orbital angular momentum states". In: *New Journal Physics* 9 (2007), p. 94.

[77] M. Malik, M. O Sullivan, B. Rodenburg, M. Mirhosseini, J. Leach, M. P. J. Lavery, M. J. Padgett, and R. W. Boyd. "Influence of atmospheric turbulence on optical communications using orbital angular momentum for encoding". In: *Optical Express* 20 (2012), p. 13195.

[78] A. Hamadou Ibrahim, F. S. Roux, M. McLaren, T. Konrad, and A. Forbes. “Orbital-angular-momentum entanglement in turbulence”. In: *Physics Review A* 88 (2013), p. 012312.

[79] Y. Zhang, S. Prabhakar, A. Hamadou Ibrahim, F. S. Roux, A. Forbes, and T. Konrad. “Experimentally observed decay of high-dimensional entanglement through turbulence”. In: *Physical Reviews A* 94 (2016), p. 032310.

[80] S. K. Goyal, A. Hamadou Ibrahim, F. S. Roux, T. Konrad, and A. Forbes. “The effect of turbulence on entanglement-based free-space quantum key distribution with photonic orbital angular momentum”. In: *Journal of Optics* 18 (2016), p. 064002.

[81] N. D. Leonhard, V. N. Shatokhin, and A. Buchleitner. “Universal entanglement decay of photonic-orbital-angular-momentum qubit states in atmospheric turbulence”. In: *Physical Reviews A* 91 (2015), p. 012345.

[82] F. S. Roux, T. Wellens, and V. N. Shatokhin. “Entanglement evolution of twisted photons in strong atmospheric turbulence”. In: *Physical Review A* 92 (2015), p. 012326.

[83] B. Rodenburg, M. P. J. Lavery, M. Malik, M. N. O Sullivan, M. Mirhosseini, D. J. Robertson, M. Padgett, and R. W. Boyd. “Influence of atmospheric turbulence on states of light carrying orbital angular momentum”. In: *Optics Letters* 37 (2012), pp. 3735–3737.

[84] B. J. Smith and M. G. Raymer. “Two-photon wave mechanics”. In: *Physical Review A* 74 (2006), p. 062104.

[85] J. C. Leader. “Atmospheric propagation of partially coherent radiation”. In: *J. Opt. Soc. Am.* 68 (1978), pp. 175–185.

[86] A. Hamadou Ibrahim, F. S. Roux, and T. Konrad. “Parameter dependence in the atmospheric decoherence of modally entangled photon pairs”. In: *Physical Review A* 90 (2014), p. 052115.

[87] J. M. Martin and S. M. Flatté. “Intensity images and statistics from numerical simulation of wave propagation in 3-D random media”. In: *Applied Optics* 27 (1988), pp. 2111–2126.

[88] J. M. Martin and S. M. Flatté. “Simulation of point-source scintillation through three-dimensional random media”. In: *J. Opt. Soc. Am. A* 7 (1990), pp. 838–847.

[89] M. A. Anguita J. A.and Neifeld and B. V. Vasic. “Turbulence-induced channel crosstalk in an orbital angular momentum-multiplexed free-space optical link”. In: *Applied Optics* 47 (2008), pp. 2414–2429.

[90] F. S. Roux. “Infinitesimal-propagation equation for decoherence of an orbital-angular-momentum-entangled biphoton state in atmospheric turbulence”. In: *Physical Review A* 83 (2011), p. 053822.

[91] F. S. Roux. “Erratum: Infinitesimal-propagation equation for decoherence of an orbital-angular-momentum-entangled biphoton state in atmospheric turbulence [Phys. Rev. A 83, 053822 (2011)]”. In: *Physical Review A* 88 (2013), p. 049906.

[92] S. M. Zhao, J. Leach, L. Y. Gong, J. Ding, and B. Y. Zheng. "Aberration corrections for free-space optical communications in atmosphere turbulence using orbital angular momentum states". In: *Optics Express* 20 (2012), pp. 452–461.

[93] Y. Ren, G. Xie, H. Huang, C. Bao, Y. Yan, N. Ahmed, M. P. J. Lavery, B. I. Erkmen, S. Dolinar, and M. Tur. "Adaptive optics compensation of multiple orbital angular momentum beams propagating through emulated atmospheric turbulence". In: *Optics Letters* 39 (2014), pp. 2845–2848.

[94] Y. Ren, G. Xie, H. Huang, N. Ahmed, Y. Yan, L. Li, C. Bao, M. P. J. Lavery, M. Tur, and M. A. Neifeld. "Adaptive-optics-based simultaneous pre-and post-turbulence compensation of multiple orbital-angular-momentum beams in a bidirectional free-space optical link". In: *Optica* 1 (2014), pp. 376–382.

[95] M. Li, M. Cvijetic, Y. Takashima, and Z. Yu. "Evaluation of channel capacities of OAM-based FSO link with real-time wavefront correction by adaptive optics". In: *Optics Express* 22 (2014), pp. 31337–31346.

[96] B. Rodenburg, M. Mirhosseini, M. Malik, O. S. Magaña-Loaiza, M. Yanakas, L. Maher, N. K. Steinhoff, G. A. Tyler, and R. W. Boyd. "Simulating thick atmospheric turbulence in the lab with application to orbital angular momentum communication". In: *New Journal of Physics* 16 (2014), p. 033020.

[97] Y. Ren, G. Xie, H. Huang, L. Li, N. Ahmed, Y. Yan, M. P. J. Lavery, R. Bock, M. Tur, and M. A. Neifeld. "Turbulence compensation of an orbital angular momentum and polarization-multiplexed link using a data-carrying beacon on a separate wavelength". In: *Optics Letters* 40 (2015), pp. 2249–2252.

[98] G. Xie, Y. Ren, H. Huang, M. P. J. Lavery, N. Ahmed, Y. Yan, C. Bao, L. Li, Z. Zhao, and Y. Cao. "Phase correction for a distorted orbital angular momentum beam using a Zernike polynomials-based stochastic-parallel-gradient-descent algorithm". In: *Optics Letters* 40 (2015), pp. 1197–1200.

[99] S. Zhao, L. Wang, L. Zou, L. Gong, W. Cheng, B. Zheng, and H. Chen. "Both channel coding and wavefront correction on the turbulence mitigation of optical communications using orbital angular momentum multiplexing". In: *Optics Communications* 376 (2016), pp. 92–98.

[100] M. Chen, F. S. Roux, and J. C. Olivier. "Detection of phase singularities with a Shack-Hartmann wavefront sensor". In: *JOSA A* 24 (2007), pp. 1994–2002.

[101] J. R. González Alonso and T. A. Brun. "Error correction with orbital angular momentum of multiple photons propagating in a turbulent atmosphere". In: *arXiv preprint arXiv:1611.04039* (2016).

[102] N. Leonhard, G. Sorelli, V. N. Shatokhin, C. Reinlein, and A. Buchleitner. "Protecting the entanglement of twisted photons by adaptive optics". In: *Physical Review A* 97 (2018), p. 012321.

[103] B. Ndagano, B. Perez-Garcia, F. S. Roux, M. McLaren, C. Rosales-Guzman, Y. Zhang, O. Mouane, R. I. Hernandez-Aranda, T. Konrad, and A. Forbes. "Characterizing quantum channels with non-separable states of classical light". In: *Nature Physics* 13 (2017), pp. 397–402.

[104] B. E. A. Saleh and M. C. Teich. *Fundamentals of photonics*. Vol. 22. Wiley New York, 1991.

[105] T. A. Nieminen, J. Higuet, G. G. Knöner, V. L. Y. Loke, S. Parkin, W. Singer, N. R. Heckenberg, and H. Rubinsztein-Dunlop. "Optically driven micromachines: progress and prospects". In: *Photonics: Design, Technology, and Packaging II*. Vol. 6038. International Society for Optics and Photonics. 2006, p. 603813.

[106] H. He, M. E. J. Friese, N. R. Heckenberg, and H. Rubinsztein-Dunlop. "Direct observation of transfer of angular momentum to absorptive particles from a laser beam with a phase singularity". In: *Physical Review Letters* 75 (1995), p. 826.

[107] Michael V Berry. "Optical currents". In: *Journal of Optics A: Pure and Applied Optics* 11 (2009), p. 094001.

[108] S. M. Barnett and L. Allen. "Orbital angular momentum and nonparaxial light beams". In: *Optics Communications* 110 (1994), pp. 670–678.

[109] L. C. Biedenharn and J. D. Louck. *Angular momentum in quantum physics: theory and application*. Cambridge University Press, 1984.

[110] K. F. Riley, M. P. Hobson, and S. J. Bence. *Mathematical methods for physics and engineering*. 1999.

[111] A. E. Siegman. "Lasers University Science Books, Mill Valley, CA, 1986. 2 A. Yariv". In: *Quantum Electronics* ().

[112] S. Feng and H. G. Winful. "Physical origin of the Gouy phase shift". In: *Optics Letters* 26 (2001), pp. 485–487.

[113] T. D. Visser and E. Wolf. "The origin of the Gouy phase anomaly and its generalization to astigmatic wavefields". In: *Optics Communications* 283 (2010), pp. 3371–3375.

[114] A. V. Carpentier, H. Michinel, J. R. Salgueiro, and D. Olivieri. "Making optical vortices with computer-generated holograms". In: *American Journal of Physics* 76 (2008), pp. 916–921.

[115] J. A. Davis, D. M. Cottrell, J. Campos, M. J Yzuel, and I. Moreno. "Encoding amplitude information onto phase-only filters". In: *Applied optics* 38 (1999), pp. 5004–5013.

[116] E. Bolduc, N. Bent, E. Santamato, E. Karimi, and R. W. Boyd. "Exact solution to simultaneous intensity and phase encryption with a single phase-only hologram". In: *Optics letters* 38 (2013), pp. 3546–3549.

[117] G. Molina-Terriza, J. P. Torres, and L. Torner. "Management of the Angular Momentum of Light: Preparation of Photons in Multidimensional Vector States of Angular Momentum". In: *Physical Review Letters* 88 (2001), p. 013601.

[118] W. K. Wootters. “Entanglement of formation of an arbitrary state of two qubits”. In: *Physical Review Letters* 80 (1998), pp. 2245–2248.

[119] C. Gerry and P. Knight. *Introductory quantum optics*. Cambridge university press, 2005.

[120] A. D. Wheelon. *Electromagnetic scintillation: volume 2, weak scattering*. Cambridge University Press, 2003.

[121] L. C. Andrews and R. L. Phillips. *Laser Beam Propagation Through Random Media*. Washington: SPIE, 1998.

[122] A. N. Kolmogorov. “The local structure of turbulence in an incompressible viscous fluid for very large Reynolds numbers”. In: *C. R. (Doki) Acad. Sci. U.S.S.R.* 30 (1941), pp. 301–305.

[123] D. W. Allan. “Statistics of atomic frequency standards”. In: *Proceedings of the IEEE* 54 (1966), pp. 221–230.

[124] J. D. Schmidt. “Numerical simulation of optical wave propagation with examples in MATLAB”. In: SPIE Bellingham, Washington, USA. 2010.

[125] C. Macaskill and T. E. Ewart. “Computer simulation of two-dimensional random wave propagation”. In: *IMA journal of applied mathematics* 33 (1984), pp. 1–15.

[126] S. M. Flatté and F. D. Tappert. “Calculation of the effect of internal waves on oceanic sound transmission”. In: *The Journal of the Acoustical Society of America* 58 (1975), pp. 1151–1159.

[127] R. Buckley. “Diffraction by a random phase-changing screen: A numerical experiment”. In: *Journal of Atmospheric and Terrestrial Physics* 37 (1975), pp. 1431–1446.

[128] C. L. Rino and J. Owen. “Numerical simulations of intensity scintillation using the power law phase screen model”. In: *Radio Science* 19 (1984), pp. 891–908.

[129] C. M. Mabena and F. S. Roux. “Optical orbital angular momentum under strong scintillation”. In: *Physical Review A* 99 (2019), p. 013828.

[130] D. L. Knepp. “Multiple phase-screen calculation of the temporal behavior of stochastic waves”. In: *Proc. IEEE* 71 (1983), pp. 722–737.

[131] R. Dashen. “Path integrals for waves in random media”. In: *Journal of Mathematical Physics* 20 (1979), pp. 894–920.

[132] B. J. Uscinski. “Analytical solution of the fourth-moment equation and interpretation as a set of phase screens”. In: *JOSA A* 2 (1985), pp. 2077–2091.

[133] R. Dashen, W. H. Munk, and K. M. Watson. *Sound transmission through a fluctuating ocean*. Cambridge University Press, 2010.

[134] R. G. Lane, A. Glindemann, and J. C. Dainty. “Simulation of a Kolmogorov phase screen”. In: *Waves in Random Media* 2 (1992), pp. 209–224.

[135] Z. Zhao, T. Yang, Y. Chen, A. Zhang, and J.-W. Pan. “Experimental realization of entanglement concentration and a quantum repeater”. In: *Physical Review Letters* 90 (2003), p. 207901.

[136] C. K. Hong, Z. Y. Ou, and L. Mandel. “Measurement of subpicosecond time intervals between two photons by interference”. In: *Physical Review Letters* 59 (1987), pp. 2044–2046.

[137] T. B. Bahder and W. M. Golding. “Clock Synchronization based on Second-Order Quantum Coherence of Entangled Photons”. In: *AIP Conference Proceedings*. Vol. 734. AIP. 2004, pp. 395–398.

[138] R. Quan, Y. Zhai, M. Wang, F. Hou, S. Wang, X. Xiang, T. Liu, S. Zhang, and R. Dong. “Demonstration of quantum synchronization based on second-order quantum coherence of entangled photons”. In: *Science Reports* 6 (2016), p. 30453.

[139] J.-D. Deschênes, L. C. Sinclair, F. R. Giorgetta, W. C. Swann, E. Baumann, H. Bergeron, M. Cermak, I. Coddington, and N. R. Newbury. “Synchronization of Distant Optical Clocks at the Femtosecond Level”. In: *Physical Review X* 6 (2016), p. 021016.

[140] S. Prabhakar, C. M. Mabena, T. Konrad, and F. S. Roux. “Turbulence and the Hong-Ou-Mandel effect”. In: *Physical Review A* 97 (2018), p. 013835.

[141] M.W Hamilton. “Phase shifts in multilayer dielectric beam splitters”. In: *American Journal of Physics* 68 (2000), pp. 186–191.

[142] C. K. Law and J. H. Eberly. “Analysis and interpretation of high transverse entanglement in optical parametric down conversion”. In: *Physical Review Letters* 92 (2004), p. 127903.

[143] Yingwen Zhang and Filippus S. Roux. “Modal spectrum in spontaneous parametric down-conversion with noncollinear phase matching”. In: *Physical Review A* 89 (2014), p. 063802.

[144] D. L. Fried. “Optical resolution through a randomly inhomogeneous medium for very long and very short exposures”. In: *J. Opt. Soc. Am.* 56 (1966), pp. 1372–1379.

[145] F. M. Miatto, H. Di Lorenzo Pires, S. M. Barnett, and M. P. van Exter. “Spatial Schmidt modes generated in parametric down-conversion”. In: *Eur. Phys. J. D* 66 (2012), p. 263.

[146] F. M. Miatto, T. Brougham, and A. M. Yao. “Cartesian and polar Schmidt bases for down-converted photons”. In: *Eur. Phys. J. D* 66 (2012), p. 183.

[147] F. S. Roux. “The Lindblad equation for the decay of entanglement due to atmospheric scintillation”. In: *J. Phys. A: Math. Theor.* 47 (2014), p. 195302.

[148] C. M. Mabena and F. S. Roux. “High-dimensional quantum channel estimation using classical light”. In: *Physical Review A* 96 (2017), p. 053860.

[149] J. Ye, H. Schnatz, and L. W. Hollberg. “Optical frequency combs: from frequency metrology to optical phase control”. In: *IEEE J. Sel. Top. Quantum Electron.* 9 (2003), pp. 1041–1058.

[150] V. Arrizon. “Optimum on-axis computer-generated hologram encoded into low-resolution phase-modulation devices”. In: *Optics Letters* 28 (2003), pp. 2521–2523.

[151] C. Palmer and E. G. Loewen. *Diffraction grating handbook*. New York: Newport Corporation, 2005.

[152] M. Mohseni, A. T. Rezakhani, and D. A. Lidar. "Quantum-process tomography: Resource analysis of different strategies". In: *Physical Review A* 77 (2008), p. 032322.

[153] E. J. Candès. "Compressive sampling". In: *Proceedings of the international congress of mathematicians*. Vol. 3. Madrid, Spain. 2006, pp. 1433–1452.

[154] E. J. Candès and M. B. Wakin. "An introduction to compressive sampling". In: *IEEE signal processing magazine* 25 (2008), pp. 21–30.

[155] D. L. Donoho. "Compressed sensing". In: *IEEE Transactions on information theory* 52 (2006), pp. 1289–1306.

[156] D. Gross, Y.-K. Liu, S. T. Flammia, S. Becker, and J. Eisert. "Quantum state tomography via compressed sensing". In: *Physical Review Letters* 105.15 (2010), p. 150401.

[157] F. Tonolini, S. Chan, M. Agnew, A. Lindsay, and J. Leach. "Reconstructing high-dimensional two-photon entangled states via compressive sensing". In: *Scientific Reports* 4 (2014), p. 6542.

[158] G. A. Howland, P. B. Dixon, and J. C. Howell. "Photon-counting compressive sensing laser radar for 3D imaging". In: *Applied Optics* 50 (2011), pp. 5917–5920.

[159] G. A. Howland and J. C. Howell. "Efficient high-dimensional entanglement imaging with a compressive-sensing double-pixel camera". In: *Physical Review X* 3 (2013), p. 011013.

[160] G. A. Howland, D. J. Lum, M. R. Ware, and J. C. Howell. "Photon counting compressive depth mapping". In: *Optics Express* 21 (2013), pp. 23822–23837.

[161] R. L Kosut, A. Shabani, and D. A. Lidar. "Robust quantum error correction via convex optimization". In: *Physical Review Letters* 100 (2008), p. 020502.

[162] A. Shabani, R. L. Kosut, M Mohseni, H. Rabitz, M. A. Broome, M. P. Almeida, A. Fedrizzi, and A. G. White. "Efficient measurement of quantum dynamics via compressive sensing". In: *Physical Review Letters* 106 (2011), p. 100401.

[163] M. Jiang, S. Luo, and S. Fu. "Channel-state duality". In: *Physical Review A* 87.2 (2013), p. 022310.

[164] J.-F. Cai, E. J. Candès, and Z. Shen. "A singular value thresholding algorithm for matrix completion". In: *SIAM Journal on Optimization* 20 (2010), pp. 1956–1982.

[165] Y. Ismail, I. Sinayskiy, and F. Petruccione. "Integrating machine learning techniques in quantum communication to characterize the quantum channel". In: *JOSA B* 36 (2019), B116–B121.